STUDY OF SOLAR-INTERPLANETARY-GEOMAGNETIC DISTURBANCES USING DATA FROM THE GLOBAL MUON DETECTOR NETWORK AND THE LASCO CORONAGRAPH

Carlos Roberto Braga

Master Thesis at Post Graduation Course in Spacial Geophysics / Solar Terrestrial Environmental Science, advised by Drs. Alisson Dal Lago, and Nelson Jorge Schuch, approved in February 28, 2011.

URL of the original document:
<http://urlib.net/8JMKD3MGP7W/395P8PH>

INPE

São José dos Campos

2011

STUDY OF SOLAR-INTERPLANETARY-GEOMAGNETIC DISTURBANCES USING DATA FROM THE GLOBAL MUON DETECTOR NETWORK AND THE LASCO CORONAGRAPH

Carlos Roberto Braga

Master Thesis at Post Graduation Course in Spacial Geophysics / Solar Terrestrial Environmental Science, advised by Drs. Alisson Dal Lago, and Nelson Jorge Schuch, approved in February 28, 2011.

URL of the original document:
<http://urlib.net/8JMKD3MGP7W/395P8PH>

INPE

São José dos Campos

2011

Aprovado (a)   pela Banca Examinadora
em cumprimento ao requisito exigido para
obtenção do Título de Mestre   em

Geofísica Espacial/Ciências do Ambiente
Solar-Terrestre

Dr.   Odim Mendes Júnior

Presidente / INPE / SJCampos - SP

Dr.   Alisson Dal Lago

Orientador(a) / INPE / São José dos Campos - SP

Dr.   Nelson Jorge Schuch

Orientador(a) / CRS / Santa Maria - RS

Dr.   Walter Demetrio Gonzalez Alarcon

Membro da Banca / INPE / SJCampos - SP

Dr.   Delano Gobbi

Membro da Banca / INPE / SJCampos - SP

Dr.   Guillermo Adrian Stenborg

Convidado(a) / Int. Inc. / Washington, D.C. - USA

Aluno (a):   Carlos Roberto Braga

São José dos Campos, 28 de fevereiro de 2011

"Seid umschlungen, Millionen!

Diesen Kuß der ganzen Welt!

Brüder, über'm Sternenzelt

Muss ein lieber Vater wohnen.

Seid umschlungen,

Diesen Kuß der ganzen Welt!

Freude, schöner Götterfunken

Tochter aus Elysium,

Freude, schöner Götterfunken

Götterfunken!"

Symphony No. 9 (Ludwig van Beethoven)

To Leonardo Murilo Adam.

ACKNOWLEDGEMENTS

ABSTRACT

The objective of this work is to study solar-interplanetary-geomagnetic disturbances like coronal mass ejections (CMEs) using observations from the white light coronagraph and high-energy cosmic ray (muons). Images from the Large Angle and Spectroscopic Coronagraph (LASCO-C3) were segmented by texture in a supervised way and the identified contour was used to estimate the radial and expansion speed of a set of 57 limb CMEs for the period between 1997 and 2001. Texture analysis was chosen in a way to parameterize the estimation of CMEs' contours, which are not always consensus. In a general view, the identified contour is in agreement with the CME definition and the estimate position angle, radial speed and expansion speed are in agreement with previous catalogs manually done. In the other hand, using high-energy cosmic ray (muons) observations, signatures preceding the arrival of plasma structures were studied using data from the Global Muon Detector Network (GMDN). Pitch angle distributions were done for periods associated with the 16 small and moderate geomagnetic storms observed in 2008. Fourteen of them show some possible precursors, both precursory increases and precursory decreases. No clear reason was found yet for not seeing precursors in the remaining two events.

ESTUDO DE DISTURBIOS SOLAR-INTERPLANETÁRIO-GEOMAGNÉTICOS USANDO DADOS DA REDE MUNDIAL DE DETECTORES DE MUONS E DO CORONÓGRAFO LASCO

RESUMO

O objetivo do trabalho da Dissertação é estudar distúrbios solar-interplanetário-geomagnéticos, como ejeções de massa coronais solares (Coronal Mass Ejections - CMEs) usando observações de coronógrafos de luz branca e de raios cósmicos de alta energia (muons). A partir de imagens do coronógrafo LASCO-C3 (*Large Angle and Spectroscopic Coronagraph)*, ejeções coronais de massa (CMEs) foram segmentadas de forma supervisionada por textura. O contorno identificado foi utilizado para estimar velocidades radiais e de expansão de um conjunto de 57 CMEs associadas a eventos solares próximos ao limbo. Optou-se por segmentação por textura, buscando-se parametrizar estimativas de velocidades de CME que não são consenso. De forma geral o contorno identificado pela técnica mostrou-se coerente com a definição de CME e a posição angular, velocidade radial e de expansão estimadas são similares aos resultados anteriores obtidos por catálogos produzidos manualmente. Por outro lado, usando dados de raios cósmicos de alta energia (muons), assinaturas precedentes a chegada da massa de plasma solar foram estudadas usando dados da Rede Mundial de Detectores de Muons (GMDN). Foi elaborada e estudada a distribuição da intensidade de raios cósmicos como função do ângulo de *pitch* para períodos associados às 16 tempestades geomagnéticas fracas ou moderadas observadas em 2008. Em 14 dos eventos foram observados possíveis precursores, tanto acréscimos como decréscimos sistemáticos. Não há razão identificada para a ausência de precursores nos dois eventos restantes.

LIST OF FIGURES

xxii

xxiii

LIST OF TABLES

CONTENTS

1 INTRODUCTION

In this Thesis two different techniques for observing solar and interplanetary structures associated to geomagnetic disturbances, like coronal mass ejections (CMEs) and their interplanetary counterparts (ICMEs), are studied: one by a white light coronagraph in the Lagrangian point L1 and the other by a network of high-energy cosmic ray (muon) ground detectors.

Coronal mass ejections (CMEs) can be seen by coronagraphs in the boundaries of the Sun (up to 30 solar radii). One key question is when the interplanetary coronal mass ejection (ICMEs) will arrive at the Earth. The first step to address is estimating the CME velocity in the coronagraph field of view. Velocities estimations were extensively done by several authors and are available in a variety of catalogs. It is noticeable, although, the lack of agreement among them. One concern about this is that they are not unique and they depend on the observer judgment. Different observers can obtain different results. One of the goals of this Thesis is an attempt to parameterize this judgment using a supervised (semi-automated) CME identification method.

At energies up to ~ 100 GeV, cosmic ray experience significant variations in response to passing solar wind disturbances such as interplanetary coronal mass ejections (ICMEs). With suitable analysis, ground-based muon detectors can yield unique information on conditions in the near-Earth interplanetary medium. Ground based muon detectors can provide information on both particle count rate and on its arrival direction. Thanks to the high speed of the particles (almost the speed of the light) compared to the speed of interplanetary disturbances (tens of hundreds kilometers per second) signatures of the disturbance can be observed in advance to their arrival at the Earth. This is illustrated in Figure 1.1. It is one goal of this work to study the influence of interplanetary structures in ground cosmic ray observations.

1
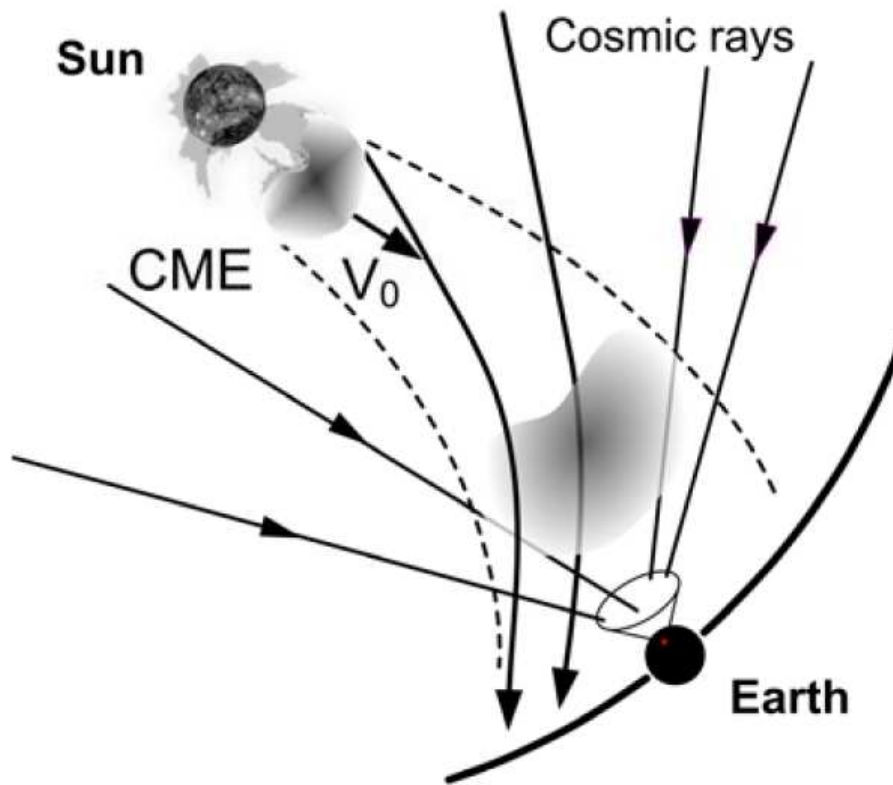
Figure 1.1.   Modulation of cosmic ray in the interplanetary medium regarded to an interplanetary disturbance like an interplanetary coronal mass ejection. The cosmic ray trajectory lines are illustrated by the continuous thin lines. The magnetic field lines are illustrated by the dashed lines and the Earth's orbit is represented by the thick continuous line.
Source: Yashin et al. (2006).

Briefly, the objectives of this Thesis are:

- to study signatures in cosmic ray prior to the storm sudden commencement using observations of ground based high energy muon detectors;

- to study coronal mass ejections using coronagraph observations in order to estimate the kinematical parameters like radial speed, central position angle etc.

This Thesis is structured as follows:

- Chapter 2, reviews the Sun, the interplanetary medium and coronal mass ejections;

- Chapter 3, reviews cosmic ray and muons;

- Chapter 4, describes the muon detectors and the methodologies for analyzing the cosmic ray data;

- Chapter 5, describes the coronagraph used in this Thesis and the methodology, based on texture analysis, for identifying coronal mass ejections;

- Chapter 6, shows the results on cosmic rays;

- Chapter 7, shows the results on coronal mass ejections;

- Chapter 8, summarizes the Thesis conclusions.

2 SUN AND INTERPLANETARY MEDIUM REVIEW

In Chapter 2 it is presented a short overview of the Sun, the interplanetary medium, coronal mass ejections (CMEs) and their relation with geomagnetic storms.

2.1 The Sun and the solar activity

The Sun is a start about 4.5 billion years old, mass around 300 thousand times that of the Earth and radius 109 times that of the Earth. The mean distance between the Sun and the Earth is 1.4959787 x 10^{11} m, defined as one astronomical unit (AU). The Sun is plasma composed of 90% of hydrogen and 10% of helium (KIVELSON; RUSSELL, 1995).

Energy is produced in the Sun by nuclear fusion of hydrogen into helium in its core, where the temperature is about 15 million Kelvin (K). The core is surrounded by the radiative zone and the convection zone. The convection zone has a differential rotation: period of 26 days close to the equator and 37 days near the poles (KIVELSON; RUSSELL, 1995).

The solar atmosphere consists of three layers, in order of distance from the core: photosphere, chromosphere and corona (Figure 2.1). From the photosphere most of the Sunlight is emitted. In the photosphere dark spots, known as Sunspot, can be seen. This are regions colder than the neighboring regions due to orders of magnitude more intense magnetic field. Surrounding the Sunspots there are brighten areas known as active regions. From the center to the photosphere, the temperature of the Sun diminishes, reaching values of order of 5785 K on the surface. The minimum temperature in the Sun's photosphere is about 4200 K and increases gradually up to millions of Kelvin in the corona (KIVELSON; RUSSELL, 1995).
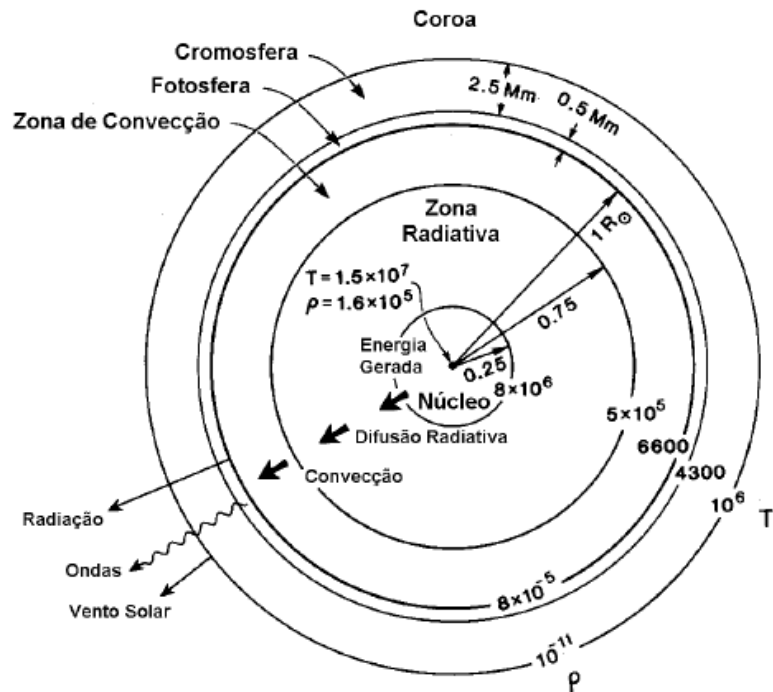
Figura 2.1.   Structure of the interior and the atmosphere of the Sun.
Source: Kivelson & Russell (1995).

The Solar activity varies with a period of about 11 years. Solar flares are an example of solar activity that occurs mainly during solar active years. High energy electrons interact with the solar atmosphere and produce intense bremsstrahlung X-rays. These particles propagate out into space and can reach the Earth's atmosphere increasing the ionization of the upper-atmosphere and they can arrive to the surface (Aschwander, 2004).

Another example of solar activity is the ejection of coronal mass ejections which are typically observed by coronagraphs. These instruments block the Sun photosphere and can observe the solar corona, which has one order of magnitude lower intensity in white light. Coronal mass ejections consist of

closed coronal magnetic field lines confining plasma from the Sun's atmosphere below the corona which are seen as bright loops. In the interplanetary medium, the results of the coronal mass ejections can be observed as large fluctuations in the magnetic field and solar wind composition. More details about coronal mass ejections are described from Section 2.6 on. In the Earth, geomagnetic storms as well as auroras can be the consequences of coronal mass ejections (ASCHWANDER, 2004).

2.2 The solar wind

The existence of the solar wind was predicted from observations of cometary tails. Astronomers noted that cometary tails always point away from the Sun. For a long time, the explanation for this cometary tails was that they were produced by solar electromagnetic radiation. Later it was predicted that the electromagnetic energy was not the appropriate explanation and that the Sun emitted also particulate energy (PARKS, 2004).

E. N. Parker in 1958 formulated a hydrodynamic model with streaming of particles at the base of the corona (criticizing a hydrostatic model from Chapman in 1957). Parker's model assumes that the pressure gradient at the solar atmospheric constituents continuously accelerates the outward streaming of particles and the streaming velocity increases outward. This model successfully predicted the solar wind speed arriving at the Earth with a speed of several hundreds of kilometers per second, which was confirmed in 1960 by the Soviet spacecraft Lunik 2 and Lunik 3 (PARKS, 2004).

The kinetic theory is considered as more appropriate for describing the physics of the solar wind than the hydrodynamic model. The fluid theories are not applicable to collisionless plasmas, such as the solar wind originating in the corona, where the density is very low. However, it is difficult to model the electric field and up to now many authors were not successful in predicting an appropriate solar wind average speed. This field is still considered as young

and much progress is needed to fully account for the solar wind features (PARKS, 2004).

In the corona, at a temperature of millions of Kelvin, 50% of the electrons have thermal velocities that exceed the gravitational escape velocity of the Sun while less than 1% of protons do. A large electric field is created by the escaping electrons which produce an excess of positive charges on the Sun. Thus, this electric field accelerates the protons outward. In this way, the corona is expanded and the Sun maintains charge neutrality. The solar wind main composition is basically protons and ~5% of $_4$He++ (~5%). Electrons are present in equal number (PARKS, 2004).

Typical speed of the solar wind in the vicinity of the Earth is about 300-800 km/s, which is a supersonic flow since the sound speed is about ~ 60km/s. The solar wind is strongly affected by changes in solar activity and the solar wind is generally said to have two types: the fast and the slow solar wind. The fast originates from the coronal holes where the magnetic field is open and has velocities between 400 km/s and 800 km/s. The solar wind has huge differences between the solar maximum and minimum. During solar minimum, it has a velocity from 250 km/s to 400 km/s, and originates from regions close to the heliospheric current sheet at the heliomagnetic equator. During solar maximum it originates above the coronal Helmet streamer in active regions where the magnetic field lines are closed (PARKS, 2004).

The slow and fast winds can collide at a certain distance from the Sun and an interaction region can be formed. This interaction region, if lasting for more than one solar rotation, is known as corotating interaction regions (CHIAN; KAMILDE, 2007).

A weak magnetic field of a few nano Teslas near the Earth is embedded in the solar wind plasma. Due to the high conductivity of the solar wind, the solar wind

8

magnetic field is frozen into the solar wind plasma and is convectively transported outward into the interplanetary medium (CHIAN; KAMILDE, 2007).

2.3 Interplanetary magnetic field

The heliospheric 3D magnetic field is defined by the flow of the solar wind. The field in the regions between the planets near the ecliptic plane is more specifically called the interplanetary magnetic field. The basic geometry of the interplanetary magnetic field has the form of an Archimedes spiral, as inferred by Parker (1963b) from the four assumptions:

- the solar wind moves radially away from the Sun at a constant speed;

- the Sun rotates with a constant period (synodic period of 27.27 days);

- the solar wind is azimuthally symmetric with respect to the solar rotation axis;

- the interplanetary magnetic field is frozen-in the solar wind and anchored at the Sun (PARKS, 2004).

 The resulting Archimedes spirals leave the Sun near-vertically to the surface and cross the Earth orbit at an angle of about 45 degrees. The magnetic field direction at Earth orbit has a two-sector pattern during the solar minimum, with oppositely directed magnetic field vector in each sector. From this ecliptic cut, a warped heliospheric current sheet can be inferred that has the shape of a "ballerina skirt" (Figure 2.2). There is a 7.5 degrees tilt between the ecliptic plane and the solar axis and another tilt up to 25 degrees between the principal dipole magnetic field and the ecliptic plane at minimum solar activity (PARKS, 2004).
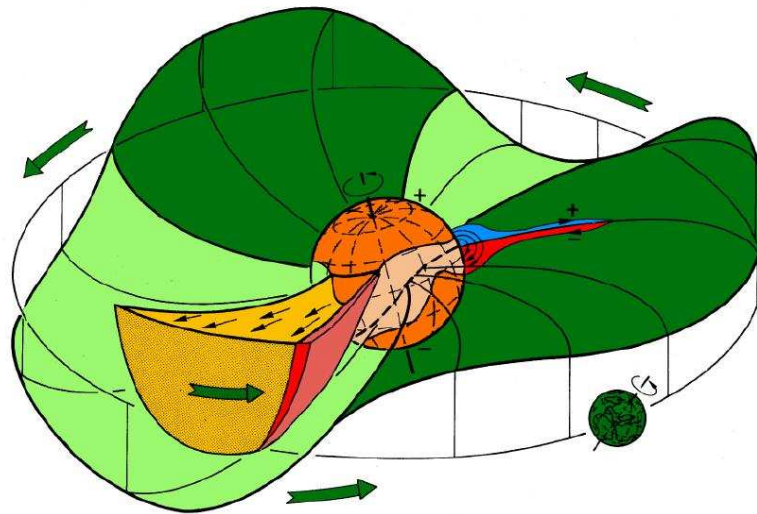
Figure 2.2.   The interplanetary magnetic field has a spiral-like radial field and the boundary layer between the two opposite magnetic polarities in the northern and southern hemispheres is warped like a "ballerina skirt". Source: Schwenn (2006).

The magnetic field is near-radial close to the Sun and falls of with inverse of the square of the distance from the Sun (near), and while it becomes more azimuthal at a few AU, it falls off with the inverse of the distance, according to the model of Parker (PARKS, 2004).

2.4 Transient Interplanetary shocks

Shocks are believed to be present in whole universe between stars and galaxies where flows of plasmas and field energy are present. Wherever the flows are, there will also be shock waves. Shocks can be present both in medium with frequent collisions (like the Earth's troposphere, when an airplane reach the speed of the sound) and in collissionless medium, like the plasma of the solar wind. They are space regions where the plasma and field go through dramatic changes in density, temperature, field strength and flow speed.

Space plasma in the heliosphere support both steady-state shocks, for example, bow shock produced by the solar wind interaction with planets, and

transient shocks, produced for example in front of interplanetary coronal mass ejections.

An interplanetary shock was first suggested in 1953 by T. Gold to explain the sudden commencement of geomagnetic storms. A coronal mass ejection or magnetic cloud can create a shock. An example of shock arrival the Earth and causing a geomagnetic storm is shown in Figure 2.3. According to a statistical study by Echer et al. (2006), 60% of the shocks in the interplanetary medium observed from 1973 to 2000 are associated to intense or moderate geomagnetic storms. When a shock compresses the magnetosphere of the Earth, protons and electrons from the solar wind partially penetrate the geomagnetic field, producing the Chapman-Ferraro current and, as a consequence, increasing the horizontal component of the magnetic field.
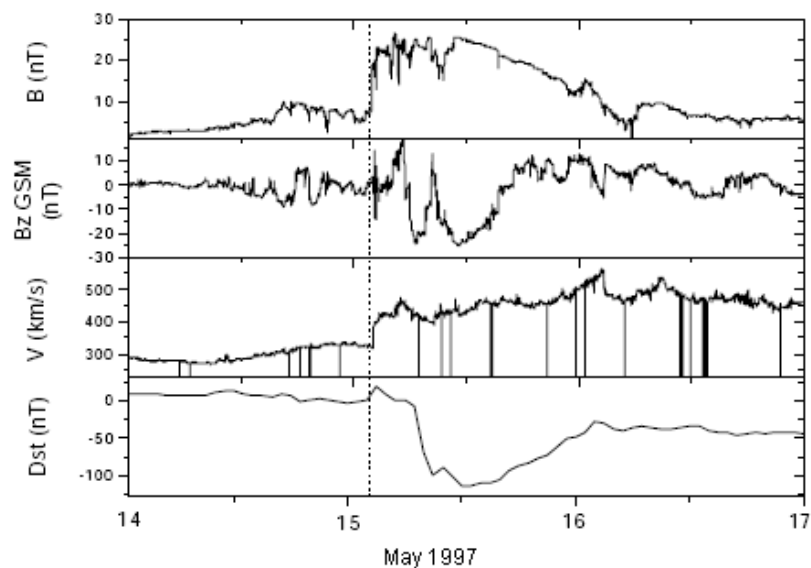
Figure 2.3.   Intensity of magnetic field, the south component, the solar wind speed by the WIND satellite in the Lagrangian point L1 and the Dst index, from May 14th to 16th 1997. The dashed line indicates the arrival of the shock. Source: Dal Lago et al. (2004).

2.5 Magnetic field of the solar corona

The solar magnetic field controls the dynamics and topology of all coronal phenomena. Heated plasma flows along magnetic field lines and energetic particles can only propagate along magnetic field lines. Coronal loops are nothing other than conduits filled with heated plasma, shaped by the geometry of the coronal magnetic field, where cross-field diffusion is strongly inhibited. Magnetic field lines take on the same role for coronal phenomena as, for example, do highways for street traffic (ASCHWANDER, 2004).

There are two different magnetic zones in the solar corona that have fundamentally different properties: open-field and closed-field regions. Open-field regions (white zones above the limb in Figure 2.4), connect the solar surface with the interplanetary field and are the source of the fast solar wind. A consequence of the open-field configuration is efficient plasma transport out into the heliosphere, whenever chromospheric plasma is heated at the footpoints. Closed-field regions (grey zones in Figure 2.4), in contrast, contain mostly closed field lines in the corona up to heights of about one solar radius, which open up at higher altitudes and connect eventually to the heliosphere, but produce a slow solar wind. It is the closed-field regions that contain all the bright and overdense coronal loops, produced by filling with chromospheric plasma that stays trapped in these closed field lines. For loops reaching altitudes higher than about one solar radius, plasma confinement starts to become leaky, because the thermal plasma pressure exceeds the weak magnetic field pressure which decreases with height. In other words, plasma beta parameter becomes bigger than one (ASCHWANDER, 2004).
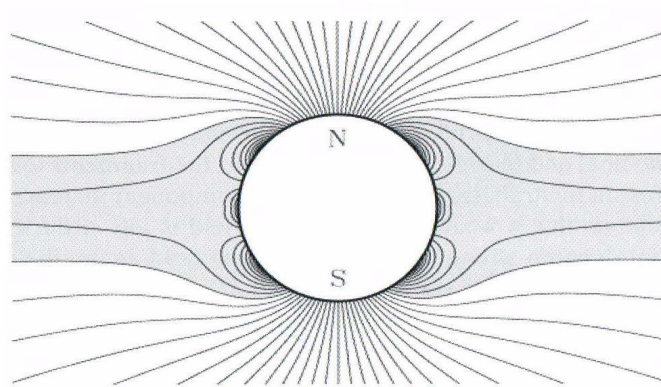
Figure 2.4.   Depiction of lines of magnetic force in the semi-empirical multipole-current sheet coronal model of Banaszkiewicz et al. (1998). The high-speed solar winds fills the unshaded volume above the solar surface. (Cranmer, 2001).
Source: Aschwander (2004).

The magnetic field on the solar surface is very inhomogeneous. The strongest magnetic field regions are in Sunspots, reaching field strengths of 0.2 - 0.3 T. Sunspot groups are dipolar, oriented in a east-west direction (with the leading spot slightly closer to the equator) and with opposite leading polarity in both hemispheres, reversing every 11-years-cycle. Active regions and their plages comprise a larger area around Sunspots, with average photospheric field of ~0.01 - 0.03 T. The background magnetic field in the quiet Sun and in coronal holes has a net field of 1×10^{-5} - 5×10^{-5} T (ASCHWANDER, 2004).

Our knowledge of the solar magnetic field is mainly based on measurements of Zeeman splitting in spectral lines, while the coronal magnetic field is reconstructed by extrapolation from magnetograms at the lower boundary, using a potential or force-free field model. The extrapolation through the chromosphere and transition region is, however, uncertain due to unknown currents and non-force free conditions. The fact that coronal loops exhibit generally much less expansion with height than potential-field models underscores the inadequacy of potential-field extrapolation. Direct measurements of the magnetic field in coronal heights are still in their infancy.

An empirical formula derived by Dulk & McLean (1978) renders the average decrease of the magnetic field with height between 1.02 and 10 solar radii,

$$B(R) = 5x10^{-5} (R/R\_Sun)^{-1.5} \text{ T} (1.02 < R/R\_Sun < 10) \qquad (2.1)$$

Depending on the solar cycle, variations of the magnetic field strength by 1-2 orders of magnitude can be present (ASCHWANDER, 2004).

2.6 Coronal Mass Ejections

The first observation of a coronal mass ejection was done in December 14th 1971 by the spacecraft Orbiting Solar Observatory (OSO-7) and the term coronal mass ejection was used for the first time by Gosling et al. (1975). The definition of CME is "an observable change in coronal structures that (1) occurs on a timescale between a few minutes and several hours and (2) involves the appearance of a new discrete, bright white-light feature in the coronagraph field of view" (HOWARD et al., 1997).

The detection of CMEs in white light requires a coronagraph. Such an instrument positions an occulting disk across the solar disk, so that very faint Thomson-scattered light from the outer corona is measured. CMEs can be observed both by spacecraft and ground based coronagraphs. The most famous spacecraft with white light coronagraphs, in order of appearance, are: Skylab (1973-1974), Solwind (1978-1985), Solar Maximum Mission (1980 and 1984-1989), Solar and Helisphere Observatory, hereafter SOHO (1996-now) and Solar Terrestrial Relations Observatory, hereafter STEREO (2006-now). One example of ground based coronagraph is the Mirror Coronagraph for Argentina (MICA). An example of a CMEs view by SOHO is shown in Figure 2.5.
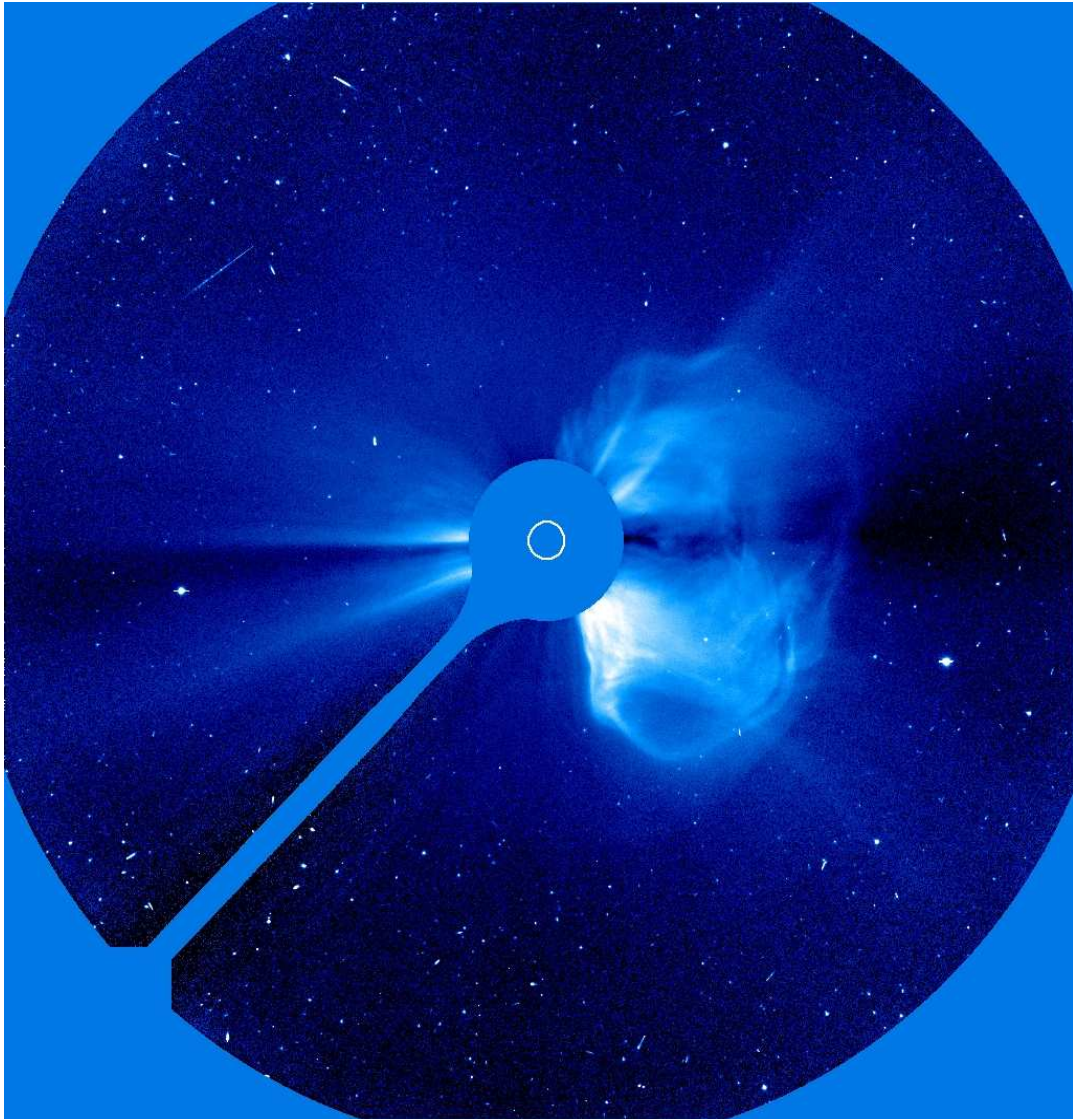
Figure 2.5.   An example of a coronal mass ejection (CME) view by SOHO LASCO-
               C2. The transient brighter features is the CME.
               Source: http://sohowww.nascom.nasa.gov/ (2010).

The phenomenon of a CME occurs with an average frequency of about one
event per day, with the frequency depending strongly on the phase of the 11-
year solar cycle. The mass carried lies in the range of 10^{14} to 10^{16} g. The
transverse size of a CME can cover from a fraction up to more than a solar
radius, and the ejection speed is in the range from hundreds to thousands of
km/s. A CME can have a shape of a flux-rope, a semi-shell, or a bubble, which

is the subject of much debate, because of ambiguities from the line-of-sight projection effects and the optical thickness of the CME. It is a general consensus that a CME is associated with a release of magnetic energy in the solar corona, but its relation to the flare phenomenon is controversial. Even big flares have no associated CME in about 40% of the cases (ANDREWS, 2003). A long-standing debate focused on the question of whether a CME is a by-product of the flare or vice versa. This question has been settled in the view that both CMEs and flares are quite distinct and independent plasma processes, although related to each other, because are by-products of a common magnetic instability controlled on a larger global scale (ASCHWANDEN, 2004).

CMEs are a major form of solar activity. They involve the expulsion of large amounts of plasma and magnetic flux at high speeds from the solar corona into the solar wind. Their manifestations in the solar wind, the Interplanetary Coronal Mass Ejection (hereafter ICME), are responsible for many major disturbances to the Earth's space environment (CARGILL; HARRA, 2007).

As detailed later, a vast range of measured parameters from CMEs have been obtained since first coronagraph in space was launched: speed, occurrence rate, latitudinal distribution, ICME speed, magnetic field strength etc. But major questions associated with CMEs persist. Some of them are:

- what is the pre-eruption configuration of the coronal field?

- what causes the CME to begin and how the CME is accelerated?

- what is the relationship between CME and solar flares?

- how does the CME interact with the solar wind to give the observed ICME and how does this depend on the CME properties at the Sun?

2.7 CME Morphology

Observations of CMEs are often sufficiently ambiguous. Geometric concepts of CMEs range from semi-spherical shells to helical fluxropes and the observations are often sufficiently ambiguous, so that, these two opposite concepts cannot easily be discriminated in the data. CME propagating in the plane of the sky have a relatively simple projected shape. Other CMEs, however, propagating in a direction toward the observer have much more complicated shapes, the so-called halo CMEs (Figure 2.6). This name was given regarded to the ring shape which covers all the sides of the occulter (HOWARD et al., 1982). The 3D configuration is still under intense investigation due to the difficulties of the optically thin coronal plasma and the highly dynamic nature of CMEs. Coronagraphs measure mainly photospheric photons scattered by free electrons in the coronal plasma (Thomson scattering). They yield the integrated density along the line-of-sight, providing only a white-light image against the plane of the sky, which is not trivial to deconvolve. Geometric inversions are only possible by using strong a priori constraints (e. g., spherical symmetry), while forward-modeling requires very flexible dynamics geometric models (ASCHWANDEN, 2004).
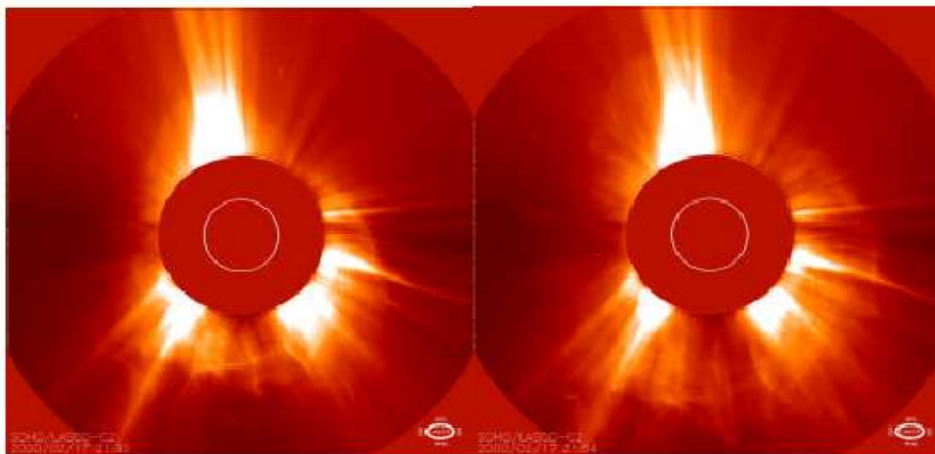
Figure 2.6.   A halo CME observed 17 February 2000 LASCO C2 onboard SOHO.
               Source: http://sohowww.nascom.nasa.gov/ (2010).

A high percentage of CMEs show a pronounced three-part structure. These events appear as having a bright leading edge, a dark void and a bright core (ILLING; HUNDHAUSEN, 1985; HOWARD et al., 1985), as displayed in Figure 2.7. The bright curvilinear leading edge indicates the association with magnetically closed regions, and must not be confused with the shock (which, if present, should be formed ahead of the leading edge). It has been suggested that the void owes its existence to the presence of a magnetic flux rope, which can be observed as circular features at the void's boundary. The bright core is usually comprised of cool prominence material, and in a number of cases seems to be suspended under the dark cavity. A structure such as a flux rope is a plausible entity capable of holding up prominences (CREMADES, 2005).
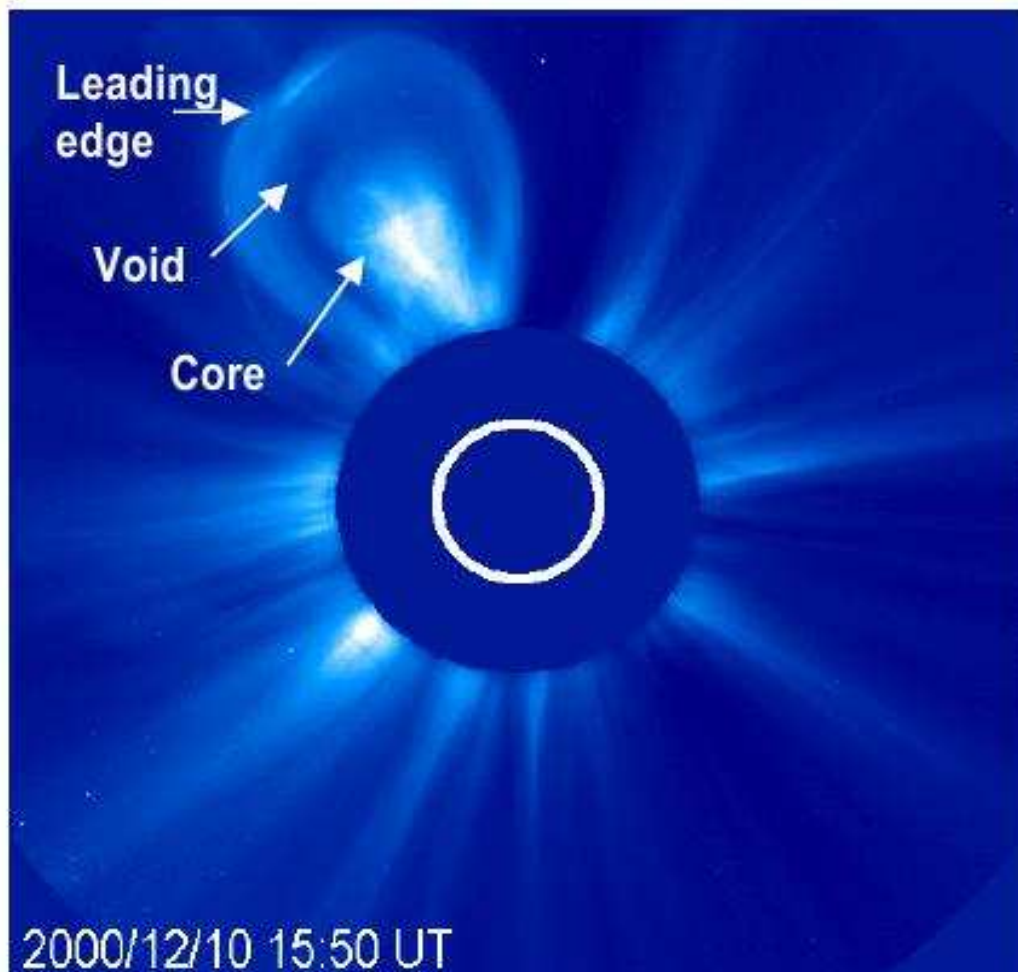
Figure 2.7.   A three-part structured CME showing the characteristic bright leading edge, dark void, and bright core. This event was observed by the LASCO/C2 coronagraph on December 10, 2000.
Source: Cremades et al. (2005).

2.8 Velocity and acceleration of CMEs

Based on the observed characteristics of CME velocity and acceleration profiles observed with SOHO/LASCO over the distance range 2 to 30 solar radii it was proposed that there are two distinct classes of CMEs (SHEELEY et al. 1999): gradual CMEs and impulsive CMEs. Gradual CMEs are apparently formed when prominences and their cavities rise up from below coronal streamers, typically attaining slow speeds from about 400 km/s to about 600 km/s with clear gradual acceleration between 3 and 40 m/s^2, at distances lower than 30

solar radii. Impulsive CMEs are often associated with flares, with speeds in excess of about 750 to 1000 km/s, observed to have a constant velocity or decelerating at distances bigger than 2 solar radii when first seen by coronagraphs. An example of each class of CME is given in Figure 2.8 and Figure 2.9: a gradual CME shows an initially positive acceleration while and impulsive CME shows initial negative acceleration.
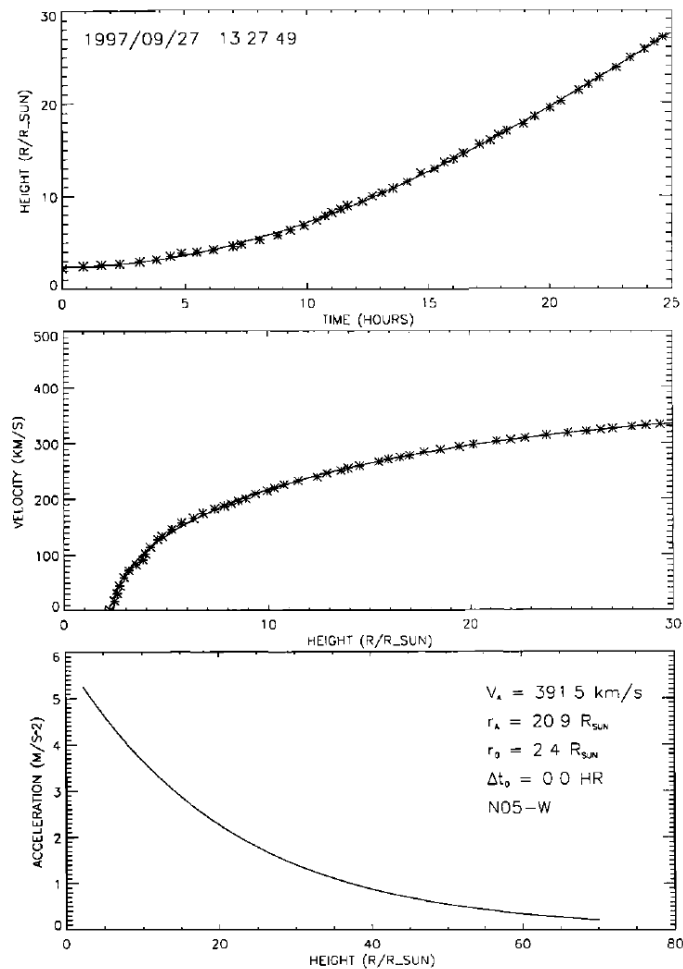
Figure 2.8.   Height-time profile h(t) plot (top), velocity v(t), and acceleration profiles a(r) (bottom), as a function of distance (normalized by the solar radii), are shown for a gradual CME with initially negative acceleration. Source: Sheeley et al. (1999).
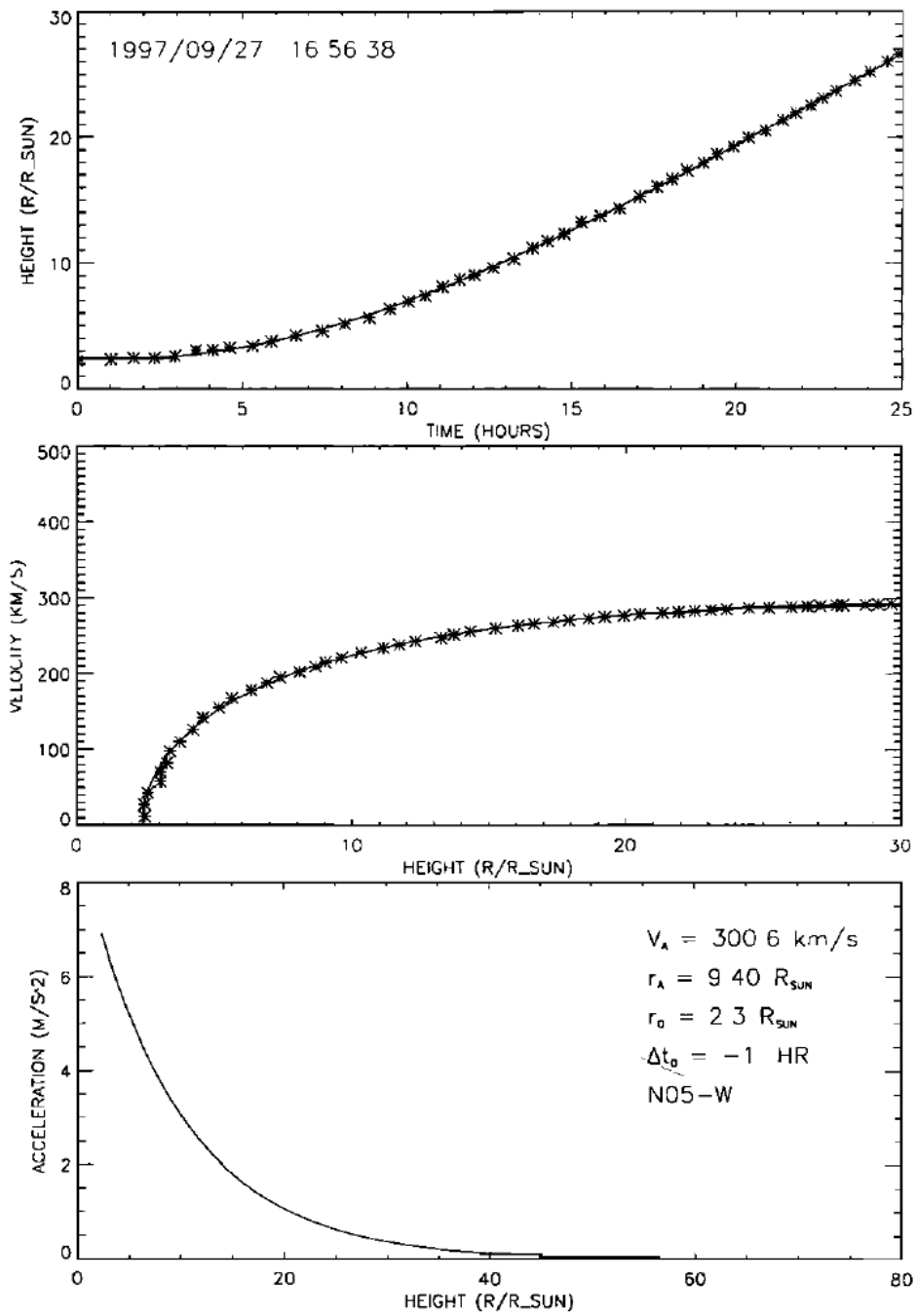
Figure 2.9.   Height-time profile h(t) plot (top), velocity v(t), and acceleration profiles a(r) (bottom), as a function of distance (normalized by the solar radii), are shown for an impulsive CME with initially positive acceleration (right) Source: Sheeley et al. (1999).

2.9 What causes CMEs: observational evidences

It is essential to mention the relation of CMEs and flares and discussing the solar origin of CMEs. In 1859 Carrignton noted that a large solar flare (the first ever observed) was associated with a major geomagnetic storm, presumably due to a CME interacting with the terrestrial magnetosphere. From this point on it was believed strongly that flare were the main cause of geomagnetic activity.

Harrison (1986) and Gosling (1993) argued that CMEs (instead of flares) were the most important influence on geomagnetic activity. The debate over Gosling's contention has continued, but a present-day consensus is that CMEs, flares, filaments (or prominences) eruptions, and other forms of energy release are closely related.

There are strong links between long duration flares and CMEs. If a long duration flare has occurred, one can be reasonably confident that its location is also the source region of the CME (e. g. Kahler, 1992). Short duration and low intensity flares (C level or less) can also be associated with CMEs and generally occur within 10 minutes of each other (CARGILL; HARRA, 2007).

CMEs can also be associated by filaments. Filaments are structures that can suspend cool ($<10^4$ K) plasma above the surface of the Sun by magnetic forces. If filaments are seen close to the limb they are called prominences. They tend to have a complex and twisted magnetic field, and so can store considerable magnetic energy. This twisted complexity can be inferred by the direction of plasma flows when a filament erupts. Evidences for twist are sometimes seen in images. Figure 2.10 (GARY; MOORE, 2004) shows helical structure (implying twist) in an eruption. A helical structure such as this is what forms the central core of the three-part CME structure discussed earlier.
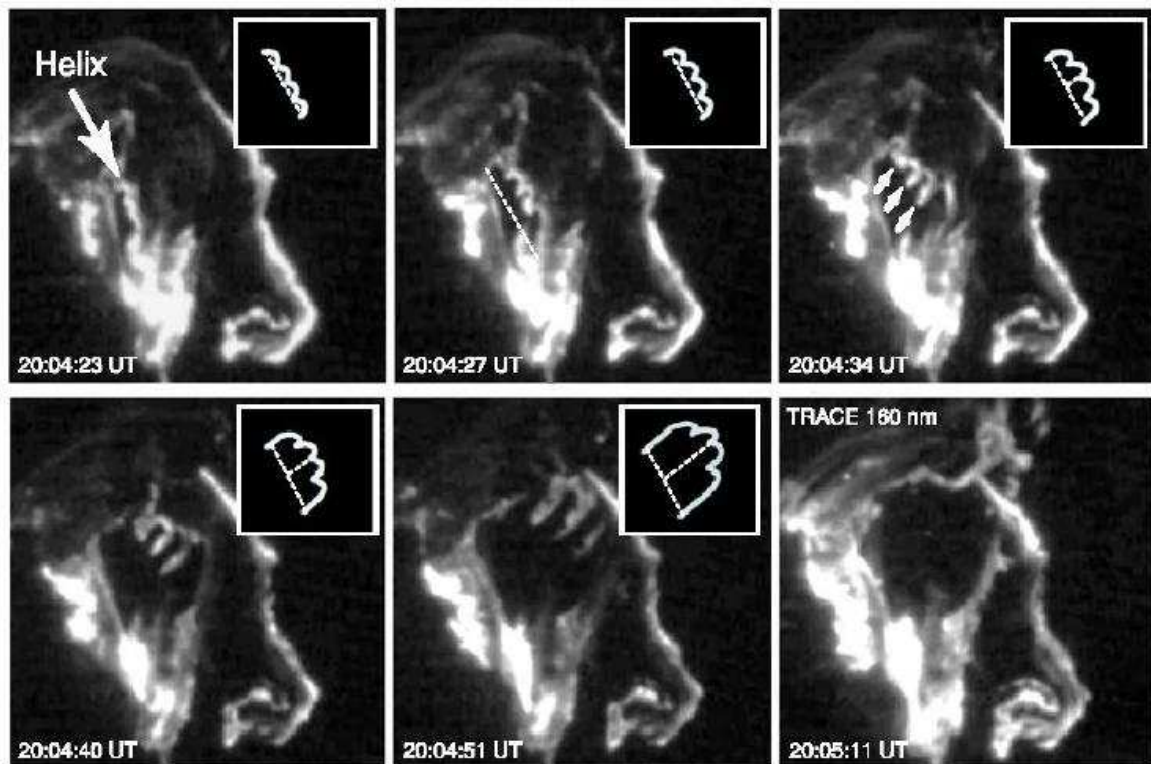
Figure 2.10.   The helical structure of an eruption seen in a flare on the 15th July 2002. The observations were made in the 160nm band the Transition Region and Coronal Explorer (TRACE).
Source: Gary and Moore (2004).

CMEs are thought to be a means of removal of magnetic helicity from the Sun into interplanetary space, so playing an important part in both the evolution of active regions as well as the reversal of the polarity of the magnetic field over a solar cycle (e. g. RUST; KUMAR, 1996).

The scale of filaments encompasses a wide range between structures extending a considerable fraction of solar radius, to miniature ones. They can occur both in active regions and quiet Sun. Filaments in active regions generally are faster than in the quiet Sun. Jing et al. (2004) showed that the majority of the filaments are destabilized by a magnetic flux emerging from the photosphere.

2.10 Geomagnetic storms

In the mid-1800's, episodes of extraordinary fluctuations in the Earth's magnetic field were denoted as storms. Over the major part of the Earth, the main feature of the magnetic storm is an unmistakable decrease of the horizontal intensity of geomagnetic field and its subsequent recovery. This decrease is due to an enhancement of the trapped magnetospheric particle population. Drifts due to the magnetic field gradient and curvature as well as gyration orbit lead to the ions moving from the midnight toward dusk and electrons from midnight toward dawn, giving an overall ring of current (GONZALEZ et al., 1994).

Some geomagnetic storms begin with a sudden impulse which signals the arrival of an interplanetary shock. This generally coincide with the onset of a period of increased ram pressure (the initial phase) that is followed by sustained southward interplanetary fields (the main phase) and then a return to normal conditions (the recovery phase). These sudden impulses preceding geomagnetic storms are called storm sudden commencements (SSC). Sometimes SSC are used as proxies for geomagnetic storms but this is not accurate since shocks that originate the SSC are neither sufficient nor necessary for geomagnetic storm occurrence or development (GONZALEZ et al., 1994).

The primary causes of geomagnetic storms at Earth are strong dawn-to-dusk electric fields associated with the passage of southward directed interplanetary magnetic fields, past the Earth for sufficiently long intervals of time. The solar wind energy transfer mechanism is magnetic reconnection between the IMF and the Earth's magnetic field (GONZALEZ et al., 1994).

The overall features involved in the solar-interplanetary-geomagnetic coupling during solar maximum is illustrated in Figure 2.11, indicating the main magnetospheric dissipation mechanisms, storms and substorms, as well as the

basic role of the "magnetospheric dynamo" in magnetospheric energization (GONZALEZ et al., 1994).

The basic energy transfer process in the Earth's magnetosphere is the conversion of directed mechanism energy from the flow of the solar wind in to magnetic energy stored in the magnetotail, followed by its reconversion into primarily thermal mechanical energy in the plasma sheet, auroral particles, ring current, and Joule heating of the ionosphere (GONZALEZ et al., 1994).

Since early studies, magnetic field reconnection between the southwardly directed IMF and the geomagnetic field is the most widely accepted mechanism for magnetospheric energization and therefore for magnetic storms (e. g., DUNGEY, 1961).
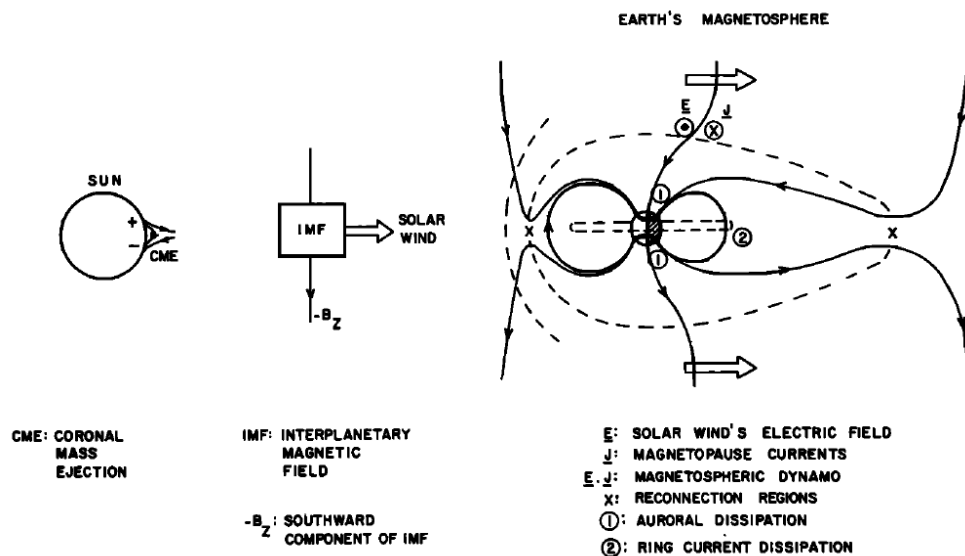
Figure 2.11.   Schematic of the solar-interplanetary-geomagnetic coupling during solar maximum years, during which a coronal mass ejection is the most important solar source for interplanetary and magnetospheric disturbances.
Source: Gonzalez et al. (1994).

It is now well-documented that large, nonrecurrent geomagnetic storms are primary caused by interplanetary disturbances driven by fast CMEs (GOSLING et al., 1990). Even some recurrent storms are enhanced by solar wind disturbances produced only by CMEs. Solar flares are not considered as fundamentally responsible for either CMEs or large geomagnetic storms. Many CMEs do not produce large disturbances either in the solar wind or in the Earth's magnetosphere. Present evidence indicates that only about 1 out of 6 CME-driven disturbances striking the Earth's magnetosphere is effective in driving a large geomagnetic storm (CROOKER; CLIVER, 1994).

3 COSMIC RAY REVIEW

In Chapter 3 it is shortly described the main aspects of cosmic ray: what they are, how they propagate in the near Earth interplanetary medium, how they interact with the Earth's atmosphere and how they are modulated by transient phenomena in the interplanetary medium.

Cosmic ray particles are produced and accelerated outside the atmosphere of the Earth and provide information about the physical processes in the near Earth interplanetary medium, among information about physical processes in various regions of the outer space.

3.1 A historical review: discovery of the main characteristics

Cosmic ray observation has started in 1912 by Victor F. Hess in several balloon flights with radiation detectors than reached an altitude of up to 5350m. While at 1500-2000 m the radiation measured was of similar value than that on the ground but, above 2500m a clear rise in the radiation level with the increasing altitude was observed. It was concluded that a radiation entered the atmosphere from above and it was supposed that this radiation was originated from gamma ray produced outside the atmosphere (HESS, 1912). This result is shown in Figure 3.1 plot. The vertical axis shows the units of ionization which are proportional to the radiation.
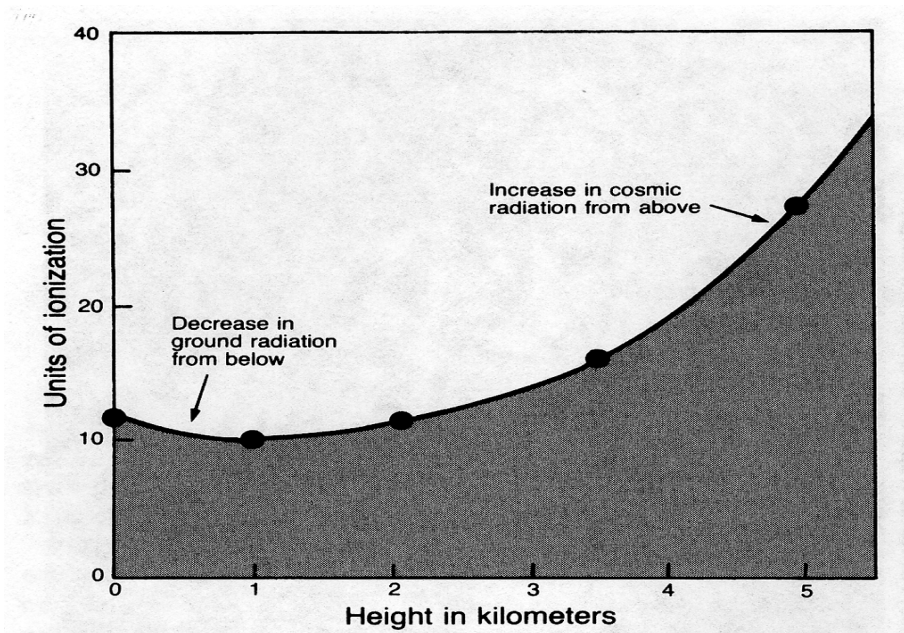
Figure 3.1. The cosmic ray observation versus height in the experiment of Hess.
Source: Hess (1932).

Bothe & Kolhöster (1929) used two Geiger Müller detectors placed close together. Large number of coincidences between detectors and also deflections that could not be explained by gamma rays were observed. This could only be explained by corpuscular rays. Clay & Berlage (1932) made a voyage with the same ionization chamber from high latitude to low latitude location. They observed falling off of the intensity with the decrease of the geomagnetic latitude and concluded that the cosmic ray incident on the Earth is a charged corpuscular radiation.

Measurements of cosmic ray near the equator, at sea level, and in Peru, at 4200 m over the sea level, showed that the cosmic ray flux was higher from the west than from the east (Johnson, 1933). This anisotropy is known as east-west effect and lead to conclusion that cosmic ray are positive charged particles. Finally by Schein et al. (1941) it was shown that primary particles of cosmic rays are mostly protons.

28

A cosmic ray is a high-speed particle – either an atomic nucleus or an electron – that travels throughout the Milky Way Galaxy, including the solar system. Some of these particles originate from the Sun, but most come from sources outside the solar system and are known as galactic cosmic rays (GCRs). Cosmic ray particles that arrive at the top of the atmosphere are called primaries; their collisions with atmospheric nuclei give rise to secondaries.

3.2 Galactic Cosmic Ray in the interplanetary medium

GCRs are high energy particles originated from extrasolar sources within our Galaxy. Although the source of GCRs has not been fully elucidated, supernova explosions are thought to be one source of GCRs. Almost 90% of cosmic ray particles are heavier nuclei. Almost 90% of cosmic ray particles are protons, about 9% are helium nuclei, about 1% are electrons and the remaining are heavier nuclei. GCRs travel from their origin to the heliosphere and enter the Earth's atmosphere through the interplanetary space. In their way to the Earth, they are modulated by the magnetic field both in the interplanetary medium and in the Earth's magnetosphere.

For a particle with charge q of mass m with velocity v and rest mass m_o in a region with magnetic field B, the Lorentz Force is:

$$\frac{d(mv)}{dt} = q(v \times B) \tag{3.1}$$

where m is the relativistic mass of the particle given by

$$m = \frac{m_o}{\sqrt{1 - v^2/c^2}} \tag{3.2}$$

where c is the speed of the light, the Larmor radius is given as

29

$$R_L = \frac{mv}{qB} = \frac{P}{cB} \qquad (3.3)$$

where P is the particle rigidity given by:

$$P = \frac{pc}{q} \quad . \qquad (3.4)$$

The particle rigidity is commonly used for instead of the particle's momentum mv because, any cosmic ray particle with the same rigidity (even with different charge or mass) will have the same Larmor radius and thus, behave in a similar way in a given magnetic field configuration. Supposing a particle with $P = 50GV$ and $B = 5nT$, a typical value for the interplanetary medium, R_L is calculated to be about 0.2 AU.

3.3 Cosmic ray observation at the Earth's surface and air showers

The cosmic ray hardly ever hit the ground but will collide (interact) with a nucleus of the air, usually several ten kilometers high. In such collisions, many new particles are created and the colliding nuclei evaporate to a large extent.

Most of the new particles are pi-mesons (pions). Neutral pions very quickly decay, usually into gamma-rays. Charged pions also decay but after a longer time. Therefore, some of the pions may collide with yet another nucleous of the air before decaying, which would be into a muon and a neutrino. The fragments of the incoming nucleous also interact again, producing new particles (BERNLÖHR, 2010).

The gamma-rays from the neutral pions may also create new particles, an electron and a positron, by the pair-creation process. Electrons and positrons in turn may produce more gamma-rays by the bremsstrahlung mechanism (BERNLÖHR, 2010).

GCRs can be observed at the Earth's surface basically by its secondary components, such as, muon and neutrons, which are generated by an interaction between the primary GCR and Earth's atmospheric nuclei. A schematic diagram indicating the generation of secondary components is shown in Figure 3.2.
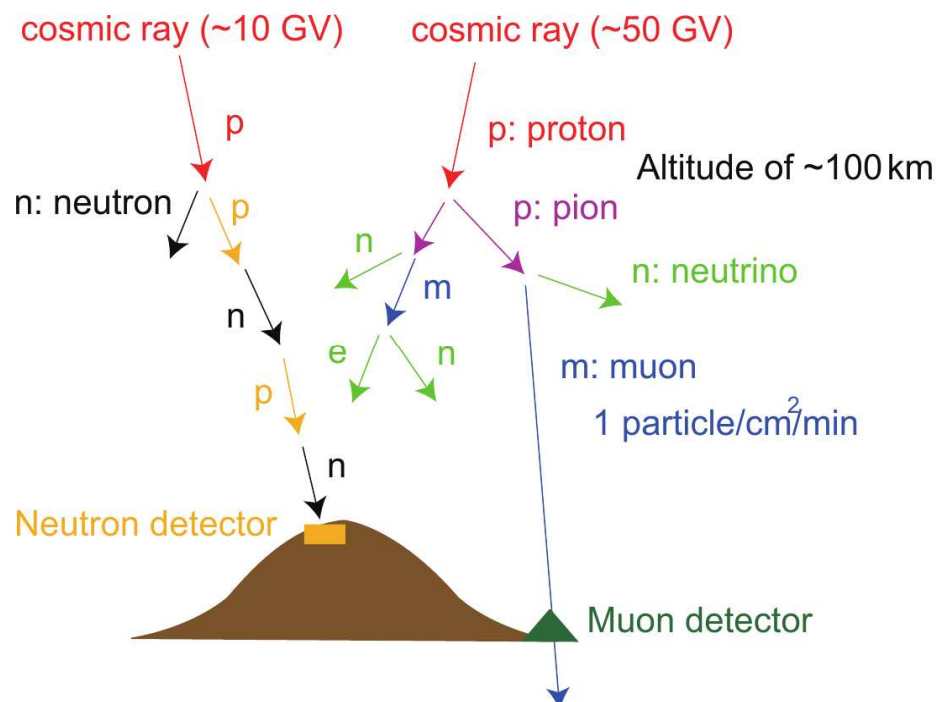
Figure 3.2.   Development of air showers generated by galactic cosmic rays reaching the Earth's atmosphere showing the types of particles that lead to the production of muons and neutrons.
Source: Okazaki (2008).

Neutrons are generated by the interaction of primary GCRs with energy of ~10 GeV. Each secondary neutron carries with a part of the energy and then collides with the other atmospheric nuclei. The collision produced other new secondary neutrons. One can measure their secondary neutrons that reach the surface with neutron monitors. Because of multiple collisions, the incident

direction of primary GCRS cannot be inferred from the observation of a single station (OKAZAKI, 2008).

Muons are generated by the interaction of primary GCRs with energy of ~ 50 GeV. The first interaction produces pions by the hadronic interaction with the atmospheric nuclei. These pions then generate other secondary particles again by colliding with the atmospheric nuclei or decay into a muon and a neutrino in 29 ns. Some muons can reach the detector at the ground level, preserving the incident direction of GCRs, because the life-time of muons of ~ 2.2×10^{-6} s is elongated by several hundred times due to relativistic time dilatation. So, ground-based muon detectors can be used to infer the direction of arrival of a particle. (OKAZAKI, 2008)

The number of particles starts to increase rapidly as this shower or cascade moves downwards in the atmosphere. On their way and in each interaction the particles loose energy, however, and eventually will not be able to create new particles. After some point, the shower maximum, more particles are stopped than created and the number of shower particles declines. Only a small fraction of the particles usually comes down to the ground. How many actually come down depends on the energy and type of the incident cosmic ray and the ground altitude. Actual numbers are subject to large fluctuations (BERNLÖHR, 2010).

When a primary cosmic ray produces many secondary particles, it is called an air shower. When many thousand (sometimes millions or even billions) of particles arrive at ground level, this is called and extensive air shower (EAS). Most of these particles will arrive within some hundred meters along the axis of motion of the original particle, now the shower axis. But some particles can be found even kilometers away. Along the axis, most particles can be found in a kind of disk only a few meters thick and moving almost at the speed of the light. This disk is slightly bent, with particles far from the axis coming later. The

spread of thickness of the disk also increases with distance from the axis (BERNLÖHR, 2010).

3.4 Muon observations

The earliest studies of secondary cosmic ray muons started with ionization chambers in the 1940s. Plastic scintillators and Geiger-Muller counters replaced these systems. Muon detection systems are directional employing two or more trays of counters to deduce the arrival direction of ionizing muons. Thus, the muon detectors systems are sometimes called muon telescopes. The latest generation of muon telescopes consists of multidirectional instruments employing more complex coincidence electronics to record muon arrivals from narrower apertures than previously achievable.

Muon observation can be done by detectors both in surface and underground detectors. Surface detectors have significant responses from approximately 10 GeV to several hundred GeV whilst underground muon observations extend up to slightly above 100 GeV. With increasing energy, galactic effects are more prevalent and solar modulation disappears (DULDIG, 1999).

Muon telescopes are simple ionizing radiation detectors arranged in two or more trays. There detectors produce output pulses of the order of 1 ms whenever a charged particle passes through them. The direction of arrival of the muon is derived from the relative positions of the counters that recorded the muons passage. Because the muons are relativistic they cross the telescope in a much shorter time than the latent detection time. A simple coincidence in response between the telescope trays in all that is required to determine the arrival direction (DULDIG, 1999). More details about the muon detectors used in the present Thesis are described in Chapter 4.

3.5 Forbush Decreases

Decreases in the cosmic ray count rate which last typically for about a week were first observed by Forbush (1937). Simpson (1954) showed that the origin of these decreases was in the interplanetary medium. Short term decreases can basically be of two types: recurrent and not-recurrent. The non-recurrent short term decreases are related to mass ejections from the Sun and generally have a sudden onset, reaching a maximum decrease within about a day and have a gradual recovery. The recurrent are related to corotating high speed solar wind streams and have a gradual onset and are more symmetric in time-profile (CANE, 2000). Historically, both types of decreases are called Forbush Decreases but some researchers use the name more selectively to apply to only non-recurrent events. In this Thesis work, both types of decreases will be called as Forbush Decreases. An Example is shown in Figure 3.3.
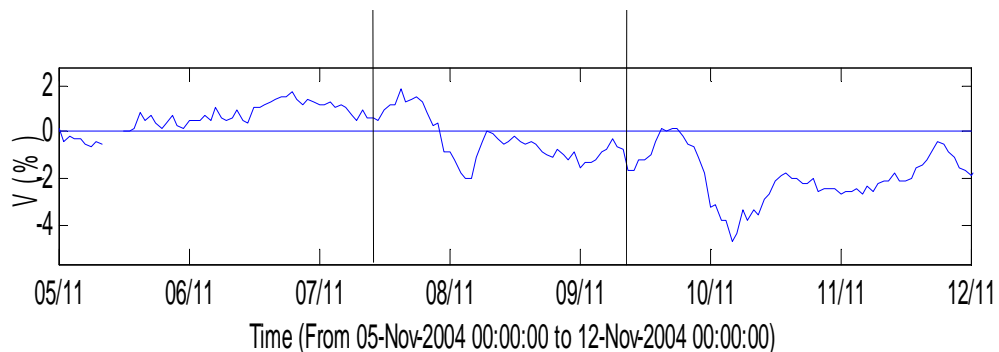
Figure 3.3.   Two Forbush Decreases observed by the muon detector of the Southern Space Observatory – SSO/CRS/CCR/INPE – MCT, in Sao Martinho da Serra, Brazil in November 2004.

Many Forbush Decreases show a precursory increase. Such an increase can result from reflection of particles from the shock or acceleration at the shock.

3.6 Variations of cosmic ray in the solar cycle

Cosmic ray intensity depicts an 11-year variation in anti-phase with solar activity (Figure 3.4). There is a time lag between the changes of solar activity and the corresponding changes in cosmic ray intensity. This time lag is due to the large size of the heliosphere and the finite propagation time of the solar wind (and the IMF disturbances moving with it) as well as the finite diffusion time of the galactic cosmic ray particles (MURSULA; USOSKIN, 2003).

One can also see a 22-year variation of cosmic ray intensity, e. g., in the different shape of cosmic ray maxima during positive and negative polarity minima (MURSULA; USOSKIN, 2003).
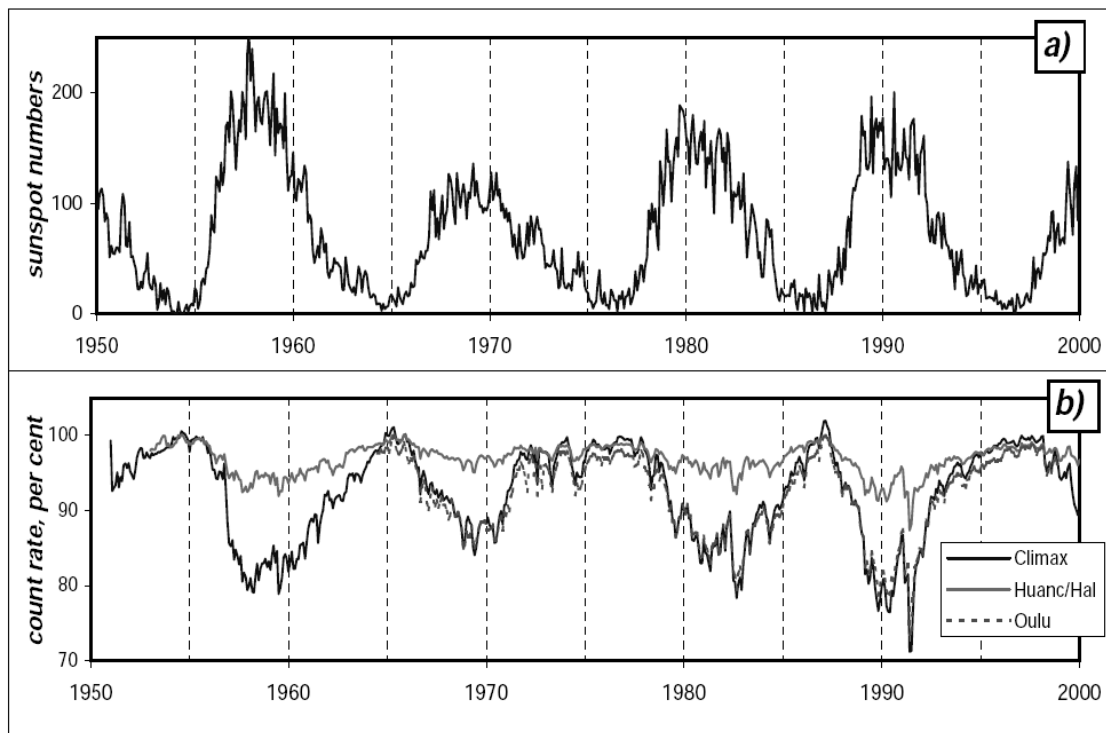
Figure 3.4.   Solar modulation of cosmic ray at neutron monitor energies. (a) Monthly sunspot numbers as index of solar activity. (b) Monthly count rates of different neutron monitors.
Source: Mursula & Usoskin (2003).

4 COSMIC RAY DETECTORS AND DATA ANALYSIS

In Chapter 4 it is described: a) the network of cosmic ray detectors used for observing cosmic ray – muons and b) the methodologies adopted in this Thesis work.

4.1 The Global Muon Detector Network

The Global Muon Detector Network (GMDN) is formed by four Multidirectional Muon Detectors (MMD) installed in Nagoya (Japan), Hobart (Australia), São Martinho da Serra (Brazil, at the Southern Space Observatory – SSO/CRS/CCR/INPE - MCT) and Kuwait city (Kuwait). Data acquisition by the network began in December 1992, as a two-hemisphere observations using a Nagoya-Hobart pair of detectors. In March 2001, a small prototype detector was installed in Sao Martinho da Serra with 4 m^2 to fill a gap in directional coverage of the network over the Atlantic and Europe. In December 2005, the detector in São Martinho da Serra was upgraded by expanding its detection area to 28 m^2. Finally, in March 2006 a detector was installed in Kuwait University, completing the current configuration of the GMDN.

The GMDN is a joint project of the Shinshu University and Nagoya University (Japan), University of Delaware (USA), Nagoya University, National Institute for Space Research and Federal University of Santa Maria (Brazil), Australian Antarctic Division and University of Tasmania (Australia) and University of Kuwait (Kuwait).

The detectors at Nagoya, Hobart and São Martinho da Serra have detection areas of 36 m^2, 9 m^2 and 28 m^2, respectively. Each of these detectors is multidirectional, allowing simultaneous record of the intensities in various directions of viewing. These detectors have an identical design, except for their detection area, consisting of two horizontal layers of plastic scintillators, vertically separated by 1.73 m, with an intermediate 5 cm layer of lead to absorb

the soft component radiation in the air (see Figure 4.1). Each layer comprises an array of 1 m^2 unit detectors, each with a 0.1 m thick plastic scintillator viewed by a photomultiplier tube of 12.7 cm diameter. By counting pulses of the twofold coincidences between a pair of detectors on the upper and lower layers, one can record the rate of muons from the corresponding incident direction. The multidirectional muon detector comprises various combinations between the upper and lower detectors.
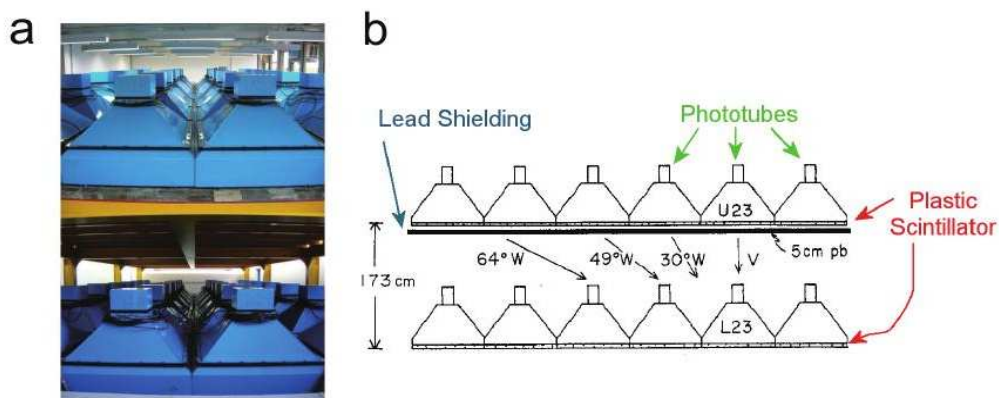
Figure 4.1.   a. Picture of the detector at the São Martinho da Serra station after an expansion in January, 2006. Each blue structure in blue is a detector. The lead shielding is in gray, in the middle of the two layers. b. Schematic of the two-fold detector. By counting pulses of the two-fold coincidences between a pair of detectors on the upper and lower layers, the rate of muons from the corresponding incident direction can be recorded.
Source: Okazaki (2008).

One of four MMDs is located at Kuwait University (Kuwait), with a detection area of 9 m^2. The Kuwait University MMD is a hodoscope (Figure 4.2). Unlike the other three MMDs, it consists of four horizontal layers of 30 Proportional Counter Tubes (PCTs). Each PCT is a 5 m long cylinder, with a 10 cm diameter, having a 50 micron thick tungsten anode along the cylinder axis. A 5 cm layer of lead is installed above the detector to absorb the soft component. The PCT axes are aligned east-west geographically aligned (X) in the top and third layers and north-south (Y) in the second and bottom layers. The top and

second layers form and upper pair, while the third and bottom layers form a lower pair. The two pairs are separated vertically by 80 cm. Muon recording is triggered by the fourfold coincidence of pulses from all layers and the incident direction is identified from X-Y locations of the upper and lower PCT pairs. This is approximately equivalent to recording muons with the two 30x30 square arrays of 10 cm x 10 cm detectors separated vertically by 80 cm. The muon count is recorded is each for 23 x 23 = 529 directional channels which cover 360 degrees of azimuth and from 0 to 60 degrees to zenith. To analyze Kuwait University data together with the data from the other three MMDs of different geometry, one rearranges the 529 directional channels in the detector into 13 channels, which are equivalent to those in the MMD at Hobart having the same detection area (9m^2), (OKAZAKI et al., 2008).

Figure 4.2.   Hodoscope multidirectional muon detector installed at the University of Kuwait. Each tube is a proportional counter. The top and second layers form and upper pair, while the third and bottom layers form a lower pair. Source: Private communication from the Cosmic Ray Laboratory from Shinshu University (2010).

The main characteristics of the GMDN are summarized in Table 4.1. The median rigidity P_m of primary cosmic rays observed, calculated by using the response function of the atmospheric muons to the primary particles (Murakami et al., 1979), ranges from 55 to 114 GV. The statistical error of hourly count rates ranges from 0.06% to 0.49%. Each symbol in Figure 4.3 (from Okazaki et

al., 2010) shows the asymptotic viewing direction, after correction for geomagnetic bending, at rigidity P_m of each directional channel, as determined using a particle trajectory code. The track through each symbol represents the spread of viewing directions for particles with rigidity in the central 80% of each directional channel's energy response. More details about the trajectory code will be explained.

Table 4.1. Main characteristics of the GMDN.

Directional channel	Average count rate	Error	P_m	Asymptotic viewing direction		Correlation	Regression
	10^4[cph]	[%]	[GV]	Latitude [°]N	Longitude [°]E		
Nagoya (35.1°N; 137.0°E)							
V	276	0.06	59.43	28.02	168.35	-0.95	-5.9
N	125	0.09	64.59	46.99	192.73	-0.95	-6.2
S	123	0.1	62.59	2.92	157.50	-0.96	-6.1
E	120	0.09	66.67	10.78	194.02	-0.95	-6.2
W	126	0.09	61.76	40.15	135.00	-0.96	-6.2
NE	58	0.14	72.03	25.85	209.41	-0.96	-6.3
NW	62	0.13	66.63	64.34	155.36	-0.96	-6.3
SE	58	0.14	69.30	-6.64	182.43	-0.96	-6.5
SW	60	0.13	65.60	12.84	131.09	-0.96	-6.4
N2	61	0.13	83.02	56.12	217.00	-0.97	-6.7
S2	60	0.13	80.47	-14.13	152.19	-0.97	-6.5
E2	58	0.14	88.32	2.03	206.75	-0.97	-6.5
W2	62	0.13	79.32	40.44	104.98	-0.97	-6.6
N3	18	0.27	105.00	59.49	236.07	-0.96	-6.5
S3	18	0.27	103.69	-24.42	149.57	-0.96	-6.3
E3	17	0.28	113.68	-1.73	213.42	-0.95	-6.4
W3	18	0.27	102.97	35.57	87.46	-0.96	-6.4
Hobart (42.9°S; 147.4°E)							
V	83	0.12	54.58	-40.02	170.48	-0.83	-4.8
N	29	0.20	59.00	-17.50	152.52	-0.82	-4.5
S	30	0.20	59.00	-53.91	205.96	-0.84	-5.0
E	30	0.20	59.00	-18.57	193.53	-0.81	-4.4
W	29	0.20	59.00	-55.58	132.35	-0.84	-4.8
NE	12	0.33	63.66	-3.86	176.04	-0.77	-4.0
NW	11	0.33	63.66	-29.07	125.77	-0.80	-4.0
SE	12	0.33	63.66	-30.16	214.75	-0.78	-4.2
SW	12	0.33	63.66	-77.18	171.56	-0.82	-4.7
N2	7.0	0.42	76.26	0.18	145.58	-0.73	-3.8
S2	7.3	0.42	76.26	-57.56	236.73	-0.80	-4.7
E2	7.2	0.42	76.26	-6.42	205.76	-0.72	-3.6

(continues)

Table 4.1. Conclusion

Directional channel	Average count rate	Error	P_m	Asymptotic viewing direction		Correlation	Regression
	10^4[cph]	[%]	[GV]	Latitude [°]N	Longitude [°]E		
W2	7.1	0.42	76.26	-53.21	95.60	-0.81	-5.0
São Martinho da Serra (29.4°S; 306.2°E)							
V	231	0.07	55.57	-22.62	330.42	-0.70	-4.1
N	88	0.11	59.81	5.29	325.29	-0.67	-3.9
S	91	0.11	59.09	-48.29	347.17	-0.74	-4.2
E	102	0.10	61.70	-10.73	358.51	-0.73	-4.1
W	102	0.10	58.3	-29.13	298.00	-0.69	-4.0
NE	42	0.15	66.55	10.34	350.29	-0.70	-3.8
NW	42	0.15	62.68	-0.90	299.03	-0.64	-3.6
SE	43	0.15	65.18	-30.59	11.22	-0.70	-3.9
SW	43	0.15	62.34	-56.84	304.03	-0.72	-4.1
N2	29	0.17	78.97	23.01	322.47	-0.68	-3.7
S2	30	0.17	77.29	-63.13	8.76	-0.68	-4.0
E2	37	0.15	80.55	-3.57	12.85	-0.67	-3.7
W2	37	0.15	74.97	-27.66	273.04	-0.68	-3.8
N3	3.4	0.46	98.97	33.26	321.53	-0.49	-4.3
S3	3.5	0.46	96.87	-68.56	32.6	-0.62	-5.8
E3	7.5	0.30	105.01	-0.056	19.97	-0.67	-4.8
W3	7.7	0.30	98.77	-23.70	257.92	-0.59	-4.4
Kuwait (29.4°N; 48.0°E)							
V	86	0.19	62.33	24.24	77.20	-0.92	-6.4
N	22	0.19	67.75	61.41	76.31	-0.93	-6.6
S	22	0.19	69.42	-11.89	90.09	-0.93	-6.9
E	22	0.20	73.45	18.08	121.09	-0.93	-6.2
W	22	0.19	65.95	12.58	36.36	-0.93	-6.8
NE	6.4	0.35	78.21	44.37	127.90	-0.92	-6.4
NW	6.5	0.34	72.86	45.12	18.76	-0.93	-6.6
SE	6.5	0.35	82.32	-5.99	119.67	-0.92	-6.3
SW	6.8	0.34	73.38	-17.43	56.14	-0.93	-7.3
N2	2.8	0.47	97.93	81.94	58.93	-0.90	-6.4
S2	2.8	0.47	102.18	-26.10	95.85	-0.89	-6.1
E2	2.6	0.49	109.77	15.90	135.89	-0.89	-6.4
W2	2.8	0.47	96.97	0.79	15.75	-0.90	-6.8

Source: adapted from Okazaki et al. (2008).
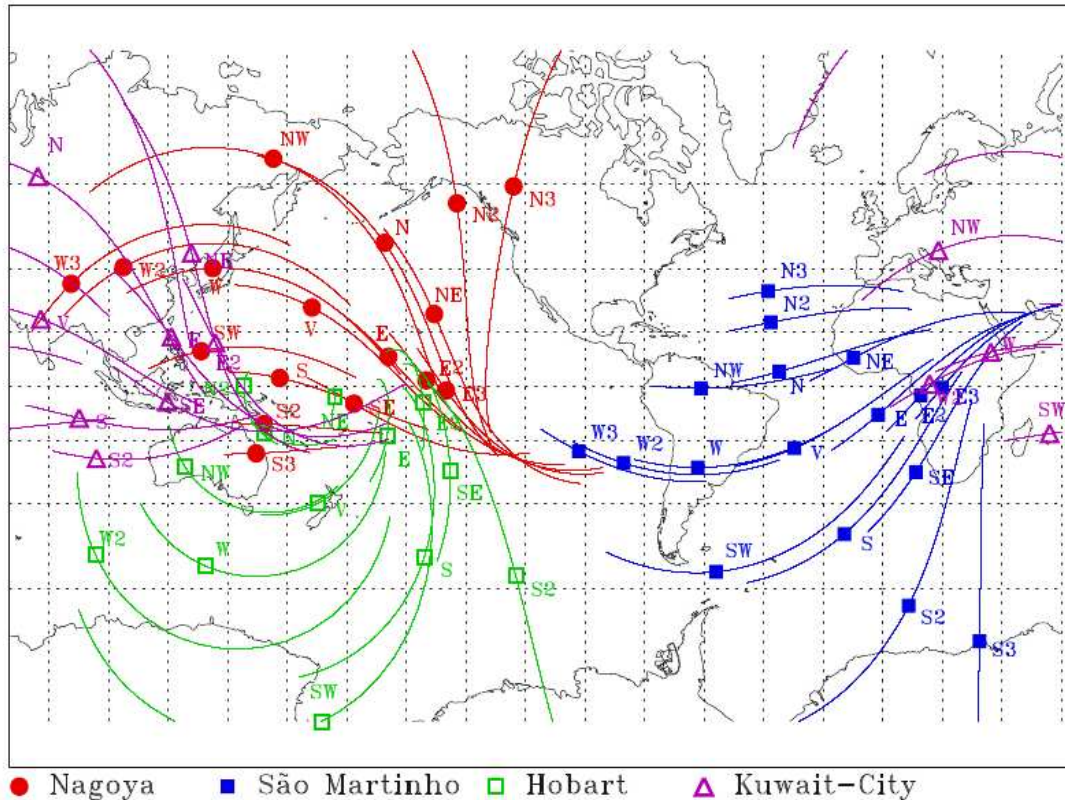
Figure 4.3.   Asymptotic viewing directions of the GMDN. Each symbol (filled circles for Nagoya, filled squares for Sao Martinho da Serra, open squares for Hobart, open triangles for Kuwait University) shows the asymptotic viewing direction (after correction for geomagnetic bending) of each directional channel. The track through each symbol represents the spread of viewing directions corresponding to the central 80% of each channel's energy response.
Source: Okazaki et al. (2008)

4.2 Atmospheric pressure effect correction

A linear regression is done to correct the atmospheric pressure effect in the observed muon count rate, following Duperier (1944, 1949):

$$\Delta I_P = \bar{I} \cdot \beta_P \cdot \Delta P \qquad (4.1)$$

$$I_{PRESSURECORRECTED} = I_{NOTCORRECTED} - \Delta I_P \qquad (4.2)$$

where $\bar{I}$ is the average of the count rate in a given directional channel calculated in a long period after removing data affected by any other sources. For simplicity, generally one year of data is used. It is very difficult to remove all the variations associated with other causes but major transient variations which are known a priori to be not atmospheric. For example, it is common to observe decreases in the count rate associated to geomagnetic storms. For these reasons periods where geomagnetic storms are observed should be removed from the dataset before calculating any regression coefficient to prevent possible bias. ΔP is the difference between a reference value for the pressure and the hourly average pressure at the site where the detector is located. Generally the reference value for the pressure is the average of the pressure calculated in the same period than the average count rate is calculated. Once β_P beta is calculated, it is assumed as constant for a given directional channel of a given station.

All the regression coefficients calculated for the all directional channels for the four stations of the GMDN are shown in Table 4.2. All the coefficients are negative, indicating an anti-correlation between the pressure and the observed muon count rate. The bigger the pressure, the lower the mean free path of the particles and the bigger the collision chance and, for this reason, bigger the decay chance.

Table 4.2. Linear regression pressure coefficients calculated for all the directional channels of the 4 MMDs of the GMDN.

Directional channel	São Martinho da Serra (%/hPa)	Nagoya (%/hPa)	Hobart (%/hPa)	Kuwait (%/hPa)
V	-0.12	-0.12	-0.17	-0.13
N	-0.12	-0.12	-0.17	-0.13
S	-0.12	-0.12	-0.17	-0.14
E	-0.11	-0.12	-0.17	-0.12
W	-0.12	-0.12	-0.17	-0.14
NE	-0.11	-0.12	-0.17	-0.12
NW	-0.12	-0.12	-0.17	-0.13
SE	-0.11	-0.12	-0.17	-0.12
SW	-0.12	-0.12	-0.17	-0.15
N2	-0.12	-0.12	-0.18	-0.12
S2	-0.12	-0.12	-0.18	-0.12
E2	-0.11	-0.12	-0.18	-0.12
W2	-0.12	-0.12	-0.18	-0.14
N3	-0.12	-0.15	x	x
S3	-0.13	-0.15	x	x
E3	-0.12	-0.15	x	x
W3	-0.13	-0.15	x	x
Wide total	**-0.110**	**-0.120**	**-0.160**	**-0.130**
Average	**950.000 hPa**	**1000.000**	**1000.000**	**1010.000**

Source: Okazaki et al. (2008).

4.3 Atmospheric temperature effect correction

The negative atmospheric temperature effect on the muon intensity measured with the surface-level detectors predominantly arises from the increase of muon decays due to the atmospheric expansion. According to first explanation given, the path of muons from the higher atmospheric level (where they are generated)

to the ground becomes longer, and more muons decay, leading to decreasing of muon intensity (BLACKETT, 1938).

A significant negative correlation, therefore, is expected between the altitude of the equi-pressure surface and the muon intensity, i.e., the muon intensity decreases with increasing the altitude due to the expansion.

There is a more complex temperature correction methodology (see Sagisaka (1986)) but the temperature variation for each atmospheric depth is required. As it is seldom to have for all muon detectors it is decided to use the simplest methodology (BLACKETT, 1938) in a similar way done by Okazaki et al. (2008), for 2006 the GMDN data set. The formula used is the similar than the correction of pressure if pressure is replaced by temperature:

$$\Delta I_T = \bar{I} \cdot \beta_T \cdot \Delta T \qquad (4.3)$$

$$I_{TEMPERATURE\,CORRECTED} = I_{NOT\,CORRECTED} - \Delta I_T \qquad (4.4)$$

Measurements of the altitude of 100hPa equi-pressure surface (henceforth called the "the altitude of 100hPa") are made continuously by radio-sonde by the British Natural Environment Research Council (NERC), once every 12 hours (close to midday and midnight), in several sites in the world, generally close to airports. To use these data, Eq. 4.3 and 4.4 can be rewritten, respectively as:

$$\Delta I_T = \bar{I} \cdot \beta_T \cdot \Delta H \qquad (4.5)$$

$$I_{TEMPERATURE\,CORRECTED} = I_{NOT\,CORRECTED} - \Delta I_T \qquad (4.6)$$

where ΔH is the deviation of the altitude of 100 hPa to its annual average.

For the Nagoya muon detector, it is used pressure data of three stations and made a mean of them: Shionomisaki, Tateno and Wajina. For the remaining muon detectors it is used data from only one high-altitude measurement site for

each detector. Details of the high-altitude pressure measurement sites for each muon stations are shown in Table 4.3.

Table 4.3. High-altitude pressure measurements sites associated to the GMDN for each MMD station.

High-altitude pressure measurements sites			Muon station	Approximate distance (km)
Name	Geographic latitude (degrees)	Geographic longitude (degrees)		
Shionomisaki	33.5 N	140.1 E	Nagoya	200
Tateno	36.0 N	140.1 E	Nagoya	400
Wajina	37.4 N	136.9 E	Nagoya	300
Porto Alegre	30.0 S	308.8 E	Sao Martinho da Serra	260
Kuwait	29.2 N	48.0 E	Kuwait	10
Hobart	42.8 N	147.5 E	Hobart	30

The altitude of 100hPa equi-pressure surface (henceforth called the "the altitude of 100hPa") is shown in the bottom panel of Figure 4.4. The observed deviation at Nagoya (red curve in upper panel) shows a seasonal variation with a maximum in the winter period in the northern hemisphere and a minimum in the summer. The deviation is calculated subtracting and dividing the result by the yearly mean of the count rate. The anti-correlation between the observed muon deviation and the altitude of 100 hPa is evident and the temperature corrected deviation (black curve) seems to have the seasonal variation eliminated.

For the vertical directional channel of Nagoya, the correlation coefficient is -0.95 and the regression coefficient is -5.9%/km. Previous results using muon data from 2006 and temperature data only from Shionomizaki are -0.95 for the correlation coefficient and -6.83%/km for the regression coefficient (Okazaki et al., 2008). For all the 60 directional channels in the GMDN, it is calculated the

correlation and regression coefficients, using pressure corrected data, in the same way than done by the vertical directional channel of Nagoya. All the coefficients calculated in the Thesis work are listed in the last two columns of Table 4.4.
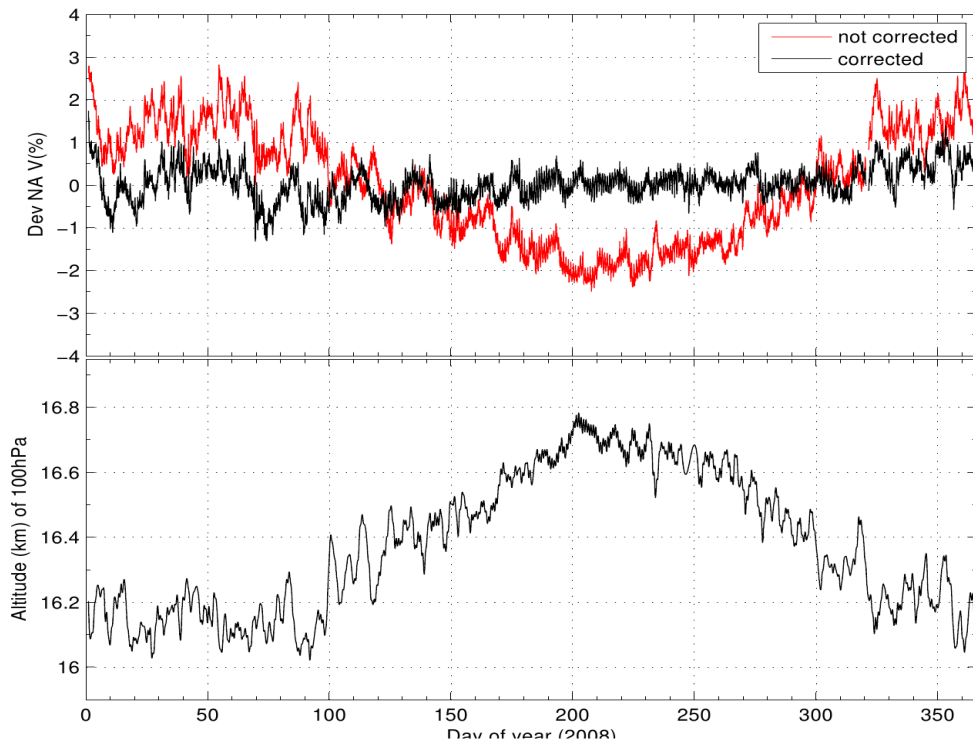
Figure 4.4.   Temperature correction for the vertical directional channel of Nagoya. Upper panel: the deviation (%) of the vertical direction of Nagoya corrected by temperature (black curve) and not corrected (red curve) by temperature. Lower panel: the altitude of the 100hPa altitude (km) of the 100hPa equi-pressure surface.

Table 4.4. Correlation (α) and regression (β_T) coefficients calculated for all the directional channels of the GMDN. The MMD's at Hobart and Kuwait do not have the N3, S3, E3 and W3 channels.

Channel	Nagoya		Hobart		Kuwait		São Martinho da Serra	
	α	β_T (%/km)	α	β_T (%/km)	α	β_T (%/km)	α	β_T (%/km)
V	-0.95	-5.9	-0.83	-4.8	-0.92	-6.4	-0.70	-4.1
N	-0.95	-6.2	-0.82	-4.5	-0.93	-6.6	-0.67	-3.9
S	-0.96	-6.1	-0.84	-5.0	-0.93	-6.9	-0.74	-4.2
E	-0.95	-6.2	-0.81	-4.4	-0.93	-6.2	-0.73	-4.1
W	-0.96	-6.2	-0.84	-4.8	-0.93	-6.8	-0.69	-4.0
NE	-0.96	-6.3	-0.77	-4.0	-0.92	-6.4	-0.70	-3.8
NW	-0.96	-6.3	-0.80	-4.0	-0.93	-6.6	-0.64	-3.6
SE	-0.96	-6.5	-0.78	-4.2	-0.92	-6.3	-0.70	-3.9
SW	-0.96	-6.4	-0.82	-4.7	-0.93	-7.3	-0.72	-4.1
N2	-0.97	-6.7	-0.73	-3.8	-0.90	-6.4	-0.68	-3.7
S2	-0.97	-6.5	-0.80	-4.7	-0.89	-6.1	-0.68	-4.0
E2	-0.97	-6.5	-0.72	-3.6	-0.89	-6.4	-0.67	-3.7
W2	-0.97	-6.6	-0.81	-5.0	-0.90	-6.8	-0.68	-3.8
N3	-0.96	-6.5					-0.49	-4.3
S3	-0.96	-6.3					-0.62	-5.8
E3	-0.95	-6.4					-0.67	-4.8
W3	-0.96	-6.4					-0.59	-4.4

In a similar way, a temperature correction of the vertical directional channel of Kuwait seems to eliminate the seasonal variation (Figure 4.5). Both Nagoya and Kuwait MMDs are stations located in the north hemisphere where the summer is in the middle of the year, in the same period than the altitude of 100 hPa is maximal. The maximum difference between the temperature corrected and not corrected deviations is about 2% for the Nagoya and the Kuwait MMDs data sets.
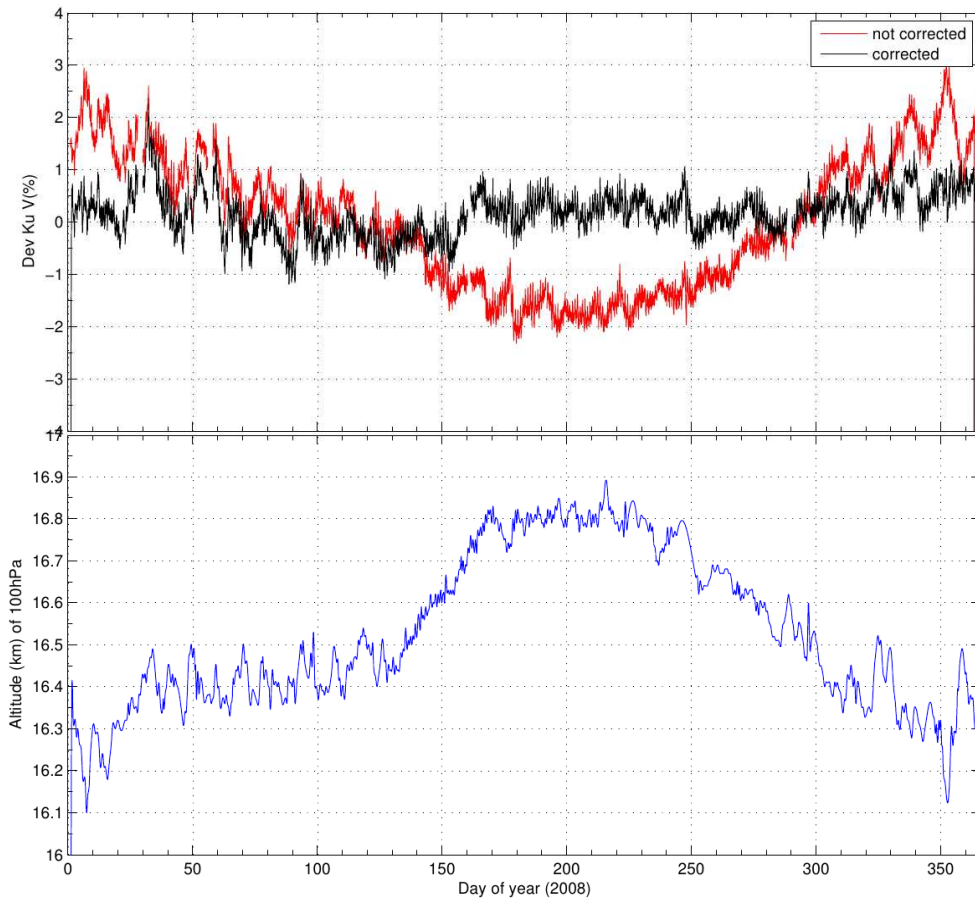
Figure 4.5.   Temperature correction for the vertical directional channel of Kuwait. Upper panel: the deviation (%) of the vertical direction of Kuwait corrected (black curve) and not corrected (red curve) by temperature. Lower panel: the altitude of the 100hPa altitude (km) of the 100hPa equi-pressure surface.

The muon detectors of São Martinho da Serra and Hobart are located in the south hemisphere and have the altitude of 100 hPa yearly variation in opposite phase: the altitude of 100 hPa has the lowest values in the middle of the year during the winter in the south hemisphere (Figure 4.6 and 4.7). The maximum difference between the temperature corrected and not corrected deviations is about 2% for Hobart and 1% for São Martinho da Serra. An explanation for the lower differences for data of Sao Martinho da Serra can be the amplitude of the annual variation of the altitude of 100 hPa: while for MMDs at Nagoya, Kuwait

49

and Hobart it is more than 600 meters, for Sao Martinho da Serra it is less than 400 meters.
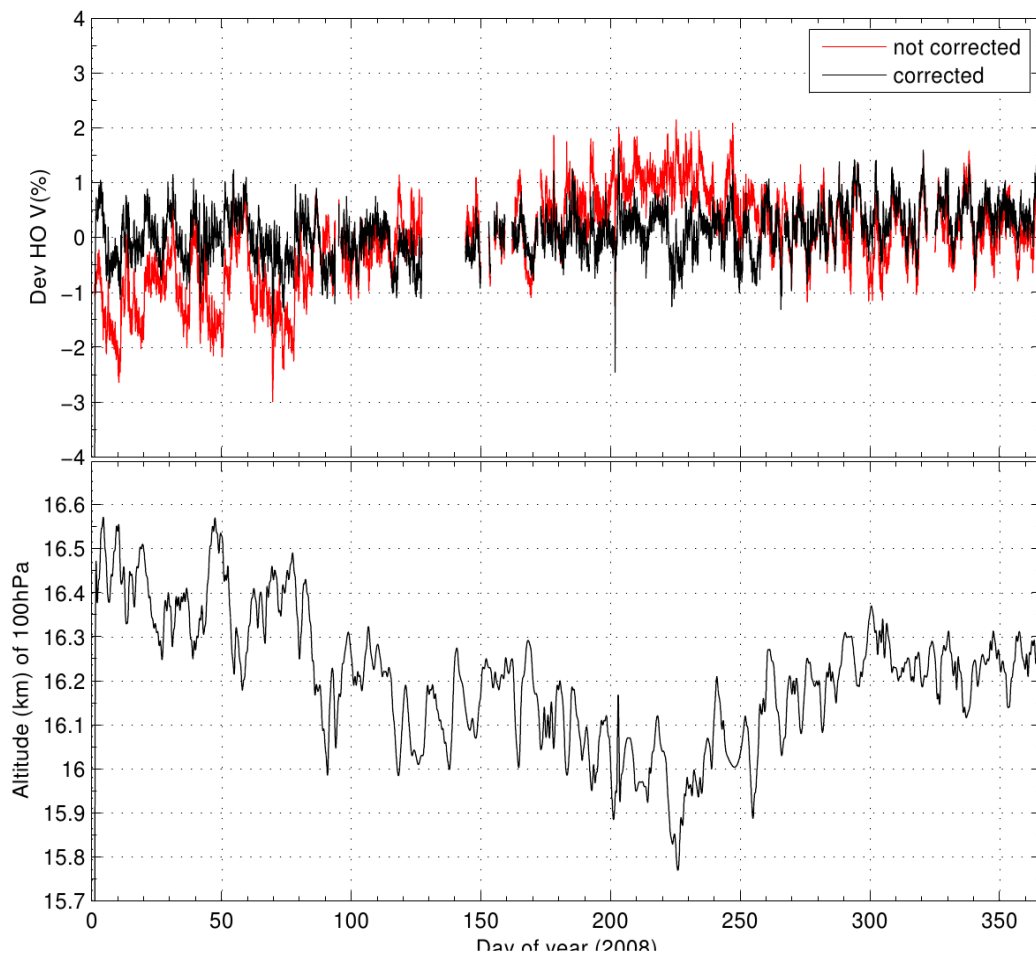
Figure 4.6.   Temperature correction for the vertical directional channel of Sao Martinho da Serra. Upper panel: the deviation (%) of the vertical direction of Sao Martinho da Serra corrected (black curve) and not corrected (red curve) by temperature. Lower panel: the altitude of the 100hPa altitude (km) of the 100hPa equi-pressure surface.
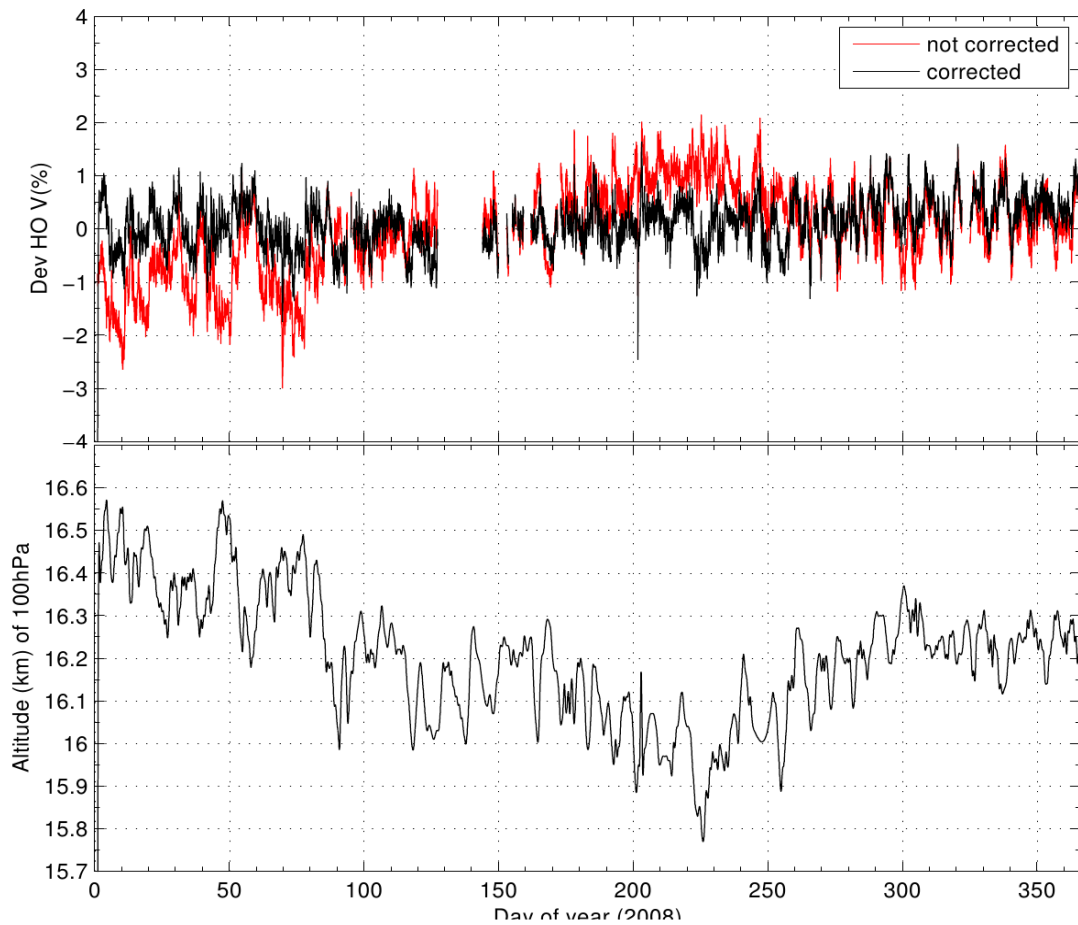
Figure 4.7.   Temperature correction for the vertical directional channel of Hobart. Upper panel: the deviation (%) of the vertical direction of Hobart corrected (black curve) and not corrected (red curve) by temperature. Lower panel: the altitude of the 100hPa altitude (km) of the 100hPa equi-pressure surface.

In summary, the twice-a-day 100 hPa altitude measurements seem to correct properly temperature effect in a yearly perspective. Temperature effect correction in a hourly perspective are still an open question.

4.4 The determination of the interplanetary magnetic field direction

In the Thesis work one is interested in determining the angle between the particle arrival and the interplanetary magnetic field (IMF) direction.

51

In a simplest way, the IMF direction can be determined by assuming a Parker Spiral and assuming a value for the radial solar wind speed. If a 400 km/s is assumed, the IMF direction is calculated to be at 45 degrees from the Earth-Sun line to the dawn.

The direction of the IMF can also be determined using *in situ* magnetic field data measurement made at Lagrangian Point L1 by the ACE spacecraft. As one is working with hourly muon data, hourly averages of the IMF are used. As ~ 50 GeV galactic cosmic ray have almost the speed of the light, they do not follow small scales variation in the IMF but only large scales variation. Fushishita et al (2010) reported that the anisotropy of galactic cosmic ray observed with the GMDN will be rather stable, changing only gradually even when the ACE IMF shows a large fluctuation.

Both methodologies were used in the present Thesis work. Results will be discussed in Chapter 6.

4.5 The particle arrival direction

A secondary cosmic ray preserve the arrival direction of the primary cosmic ray and, in this way, by observing the direction of arrival of a given muon by the directional channels of the detector, the approximate direction of incidence of the primary cosmic ray can be derived.

Geomagnetic bending was corrected using the International Geomagnetic Reference Field (IGRF) model of 1995 for the internal field. The trajectory code was developed by Lin et al (1995) and was previously used for the GMDN in several articles (e. g. Munakata et al., 2000; Kuwabara et al., 2004, Okazaki et al., 2008; Da Silva, 2009). Some assumptions made in the code are:

a) if the charge sign and velocity of a particle is simultaneously reversed, the propagation equations remain unchanged. Thus one can determine trajectories of incident particles by calculating the

trajectories of oppositely charged particles with the same rigidity shooting from the Earth. So, in this case, instead of simulating a proton reach the Earth's atmosphere, an antiproton shooting from the Earth's surface is simulated. This is the typical method which was introduced by Cracken et al. (1962), who used Runge-Kutta method of integration;

b) the motion of a particle within a sufficiently small region is accurately approximated by the helical motion of the same particle in a uniform magnetic field. To obtain satisfactory accuracy, very small integration steps must be chosen. In our trajectory tracing code, the integration step size is varied adaptively along the trajectory;

c) effects of electric field are neglected. For instance, if the total potential drop across the magnetosphere is 200 kV, then the average electric field is ~1mV/m at 10 Earth's radii. If the magnetic field at the same location is ~20 nT, then the ratio of electric to magnetic forces acting on a relativistic particle is ~2 x 10^{-4};

d) magnetic field used span the range from 4 to 70 Earth's radii;

e) variations in the trajectories regarded to geomagnetic activity are not taken in account since they are expected to be negligible for 50 GV particles.

In the previously mentioned works a combination of 16 zenith angles (from 4 to 64 degrees, step of 4 degrees), 24 azimuth angles (from 0 to 345 degrees, step of 15 degrees) and 77 rigidities (an arbitrarily chosen geometric progression with ratio of 1.154755 ranging from 1.7783 to 100000 GV) were simulated. The output of the model is the longitude and latitude of the particle in the top of the atmosphere for a given rigidity, azimuth angle and zenith angle. The code also

can determine if a given trajectory is possible or not. In some cases the particle is deflected in a way that it cannot cross the atmosphere.

With the results of the particle trajectory code and information of the directional channels (location of the station, azimuth and zenith angle), a global map of the asymptotic viewing directions corrected for geomagnetic bending is produced (Figure 4.3). The track through each symbol represents the spread of viewing of viewing directions of particles with rigidity median P_m (see Table 4.1) between $P_{0.1}$ and $P_{0.9}$ which correspond to the central 80% of each directional channel's energy response.

4.6 Diurnal variations

A distribution of the diurnal variation for the four vertical channels (after pressure and temperature corrections) is shown in Figure 4.8. The local time was calculated from the universal time using the longitude of the asymptotic direction of viewing of each vertical channel. For each one of the 24 hourly periods in a day, the yearly mean is plotted. It is clear that the maximum is present in the early afternoon sector and the minimum in the post-midnight. The amplitude of the variation is about ~0.2%. In the figure 100% means the yearly average. Generally this curve is fitted by a cosine function. This observed daily variation can be explained by the diffusion-convection model which is detailed above.

The resulting effect from the convection-diffusion model is shown in Figure 4.9. In the Figure 4.9, the black circle represents the Earth and the yellow circle the Sun. An idealized magnetic line of force is represented by the continuous black line. The directions corresponding to the local time (LT) sector are shown around the Earth. The black arrows indicate the direction of the anisotropy (the vector points toward a direction from which the maximum is expected) due to the convention, diffusion and the combination of both effects (thicker arrow).
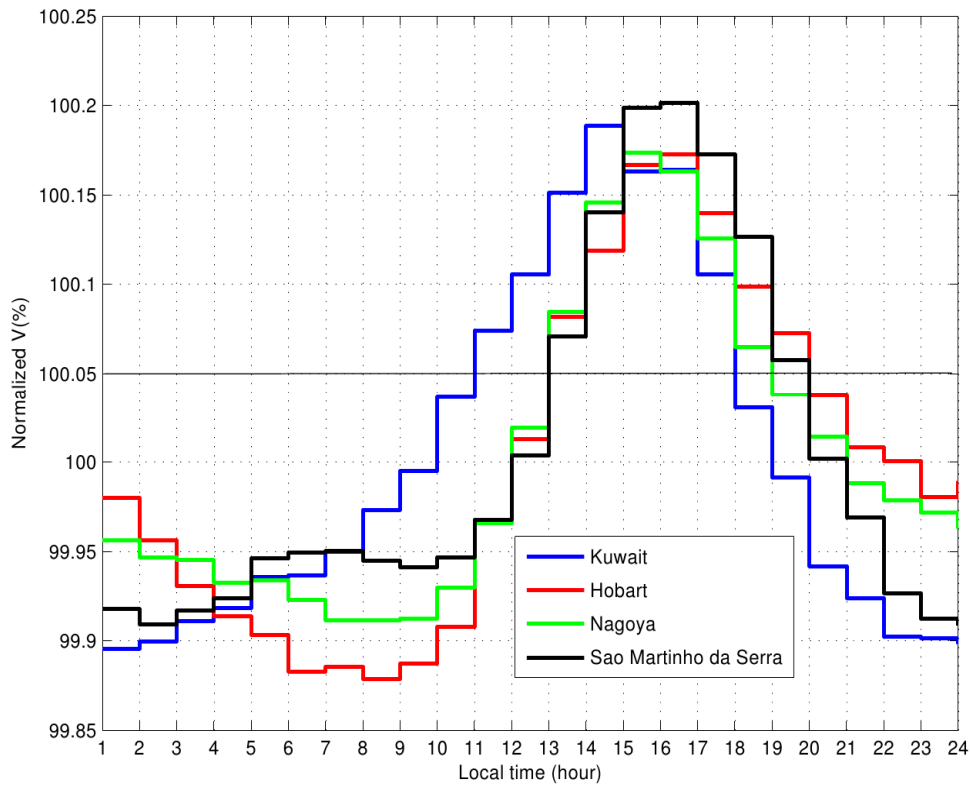
Figure 4.8.   Normalized vertical count rate (after correction of pressure and temperature) for the four MMD stations of the GMND in local time.

Cosmic ray diffusion generally is expressed in a three dimension tensor. It is estimated from the measurements of the fluctuation of this magnetic field that the diffusion coefficient perpendicular to the magnetic field is about ten times less than the parallel to the magnetic field which is about 3×10^{22} cm^2/s for cosmic ray of rigidity of 10 GV. As a results, cosmic ray diffuse mainly along the direction of the magnetic lines of force, which lies in the direction from 9 to 21 hours on the average, as referred to the Earth.
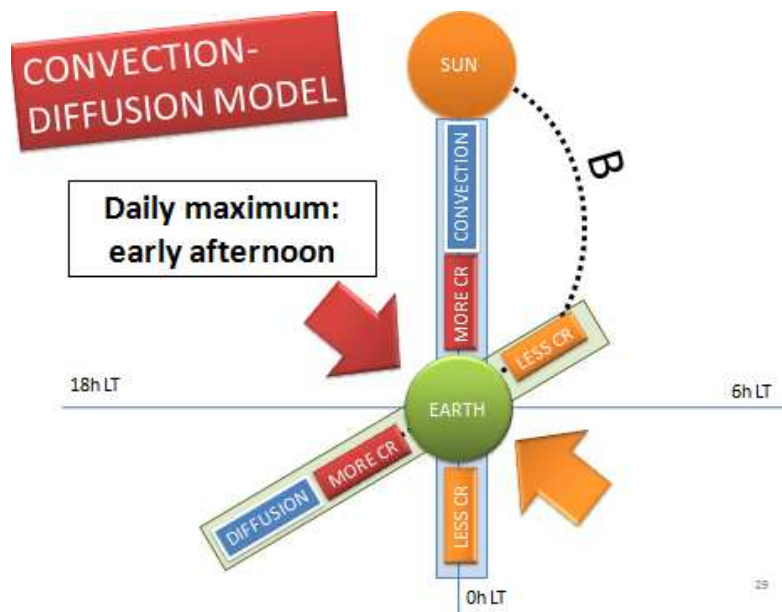
Figure 4.9.   The diurnal anisotropy as a combination of the convection and diffusion of cosmic rays.

The flow of cosmic ray is not caused from such diffusion only in the steady state, but the magnetic fluctuation due to the solar wind flowing outward from the 12 o'clock direction seems responsible for this flow. For the movement of this fluctuation tends to push cosmic ray particles to the 0 hour direction on the average. This tendency may also be interpreted as follows: when cosmic ray particles diffuse in the mean direction of the magnetic field lines of force by being scattered by the magnetic fluctuation, it may be supposed that they are moving with the coordinate frame of the magnetic field moving with the solar wind. Since this frame moves with speed V relative to the Earth, observers on the Earth observe the Compton-Getting effect (WADA; MURAKAMI, 1988).

With the explanation above, it became possible to explain the mean pattern in the diurnal variation of cosmic ray intensity. For more detailed explanation of the daily variation, the polarity reversal of the magnetic field should be taken in account (Wada & Murakami, 1988). Other sources may change the idealized picture like drifts, local latitudinal gradients, varying level of diffusion, changing

solar wind conditions and even the Earth's orbital motion can give a minor contribution (MURSULA; USOSKIN, 2003).

4.7 Trailing moving average

To avoid the spurious diurnal variations in the pressure and temperature corrected muon data $I_{i,j}(t)$, a normalization of 24 hours trailing moving average (TMA) of a given directional channel i and a given station j $r_{i,j}(t)$ to that of the vertical channel of a reference station $r_{1,1}(t)$ according to the expression:

$$J_{i,j}(t) = I_{i,j}(t) \cdot \frac{r_{1,1}(t)}{r_{i,j}(t)}$$ (4.5)

where $J_{i,j}(t)$ is the normalized data. This normalization efficiently removes the spurious diurnal variation and works well for deriving the temporal variation over a period shorter than 24 hours. This normalization is based on previous works from Kuwabara et al. (2004) and Okazaki et al. (2008).

4.8 Determination of the pitch angle distribution

Once the direction of the IMF (or using a Parker spiral assuming a constant speed of 400 km/s for the solar wind) and the arrival direction of a particle are calculated, the pitch angle can be computed simply as the difference between both. A zero degree pitch angle means the direction of the interplanetary magnetic field toward the Sun, while a 180 degree pitch angle means the anti-Sunward direction.

Using hourly pressure and temperature corrected data the pitch angle for each of the GMDN 60 directional channels in each hour is calculated.

4.9 First order anisotropy

As only two measurements in a day were available for the correction of the temperature effect in muon data, hourly muon data can still be affected by this

effect. In this way, the first order anisotropy was calculated following Munakata et al. (2000).

The angular separation between two directional channels in a detector is about 120 degrees at most, and the horizontal separation of paths along two directions is only 350 km even at the top (~100 km above the sea level) of the atmosphere. The horizontal separation is much smaller at low altitudes. The temperature variation in the atmosphere and the temperature effect, therefore, can be regarded to be almost constant wihin such a small region in the atmosphere covered by a single station. This is true particularly hourly mean values of muon count rates analyzed in this work. For this reason, the following best fit calculation for the pitch angle distribution $J_{i,j}^{cal}(t)$ to the observed normalized count rage in the station (subscript i) and directional channel (subscript j) at a time t ($J_{i,j}^{obs}(t)$)

$$J_{i,j}^{cal}(t) = J_i^0(t) + J_i^1(t)\cos(\chi_{i,j}(t)), \qquad (4.6)$$

where $\chi_{i,j}(t)$ is the pitch angle calculated. One of the best fit parameters, $J_i^0(t)$, in Eq. 4.6 represents effects, including the temperature effect, which are common for all directional channels but different from one station to the other, while $J_i^1(t)$ is the best fit parameter representing the first-order anisotropy. Simply $J_i^0(t)$ is subtracted from $J_{i,j}^{obs}(t)$ to extract only the anisotropic component of $J_{i,j}^{obs}(t)$, which is free from the temperature effect and which is the object of primary interest here.

5 OBSERVATION OF CMES AND METHODOLOGY FOR TRACKING

In Chapter 5 both the instruments and methodology for tracking CMEs are described.

Coronal mass ejections (CMEs) are studied and discussed in this Thesis work based on data from Large Angle Spectrometric Coronagraph (LASCO) on-board the spacecraft Solar and Heliospheric Observatory (SOHO). Some aspects related to data processing are also explained in this chapter.

Previous catalogs of CMEs parameters, both manually and automatically made, are described and compared in this Thesis. Finally, the current methodology is introduced: the motivation, definition of texture, tracking of events and the selected events.

New algorithms were created as part of this Thesis to address the kinematical properties of CMEs like radial speed, position angle and radial speed.

5.1 The LASCO coronagraph

The Solar and Heliospheric Observatory (SOHO) is a NASA and ESA joint mission. The SOHO satellite (DOMINGO et al., 1995) was launched on December 2nd 1995 and cruised for 4 months to reach a halo orbit about the L1 Lagrangian point, which is located along the Sun-Earth line at about 1.6×10^6 km from the Earth toward the Sun. In a fixed Sun-Earth reference frame, the projection of the halo orbit onto the plane of the sky is an ellipse, with the semi-major and the semi-minor axes of about 650,000 km and 200,000 km, respectively. At this orbit the satellite is able to observe the Sun continuously, without interruptions usually associated with near-Earth orbits satellites (HOWARD et al., 1997).

The Large Angle Spectrometric Coronagraph (LASCO) is a white light coronagraph experiment consisting of three optical systems: an internally

occulted coronagraph (C1) and two traditional externally occulted coronagraphs (C2 and C3), see Figure 5.1 and 5.2. Together, the three coronagraphs can observe the solar corona from 1.1 to 30 solar radius. More technical details about the coronagraphs are presented in Table 5.1.
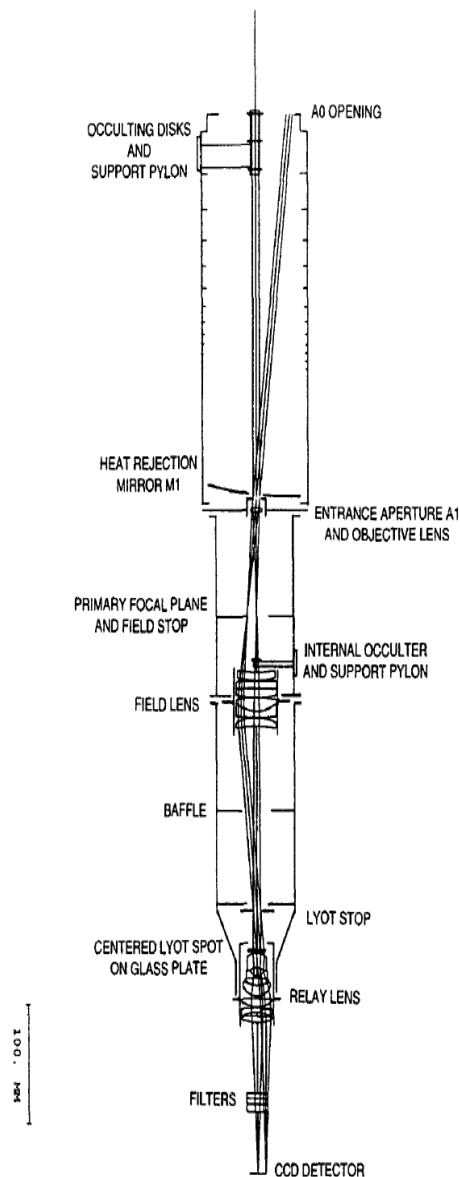
Figure 5.1.   The optical system and instrument tube of the SOHO LASCO-C3 wide field coronagraph. A 30 solar radii and an axial (occulted) ray bundle are shown.
Brueckner et al. (1995).

60
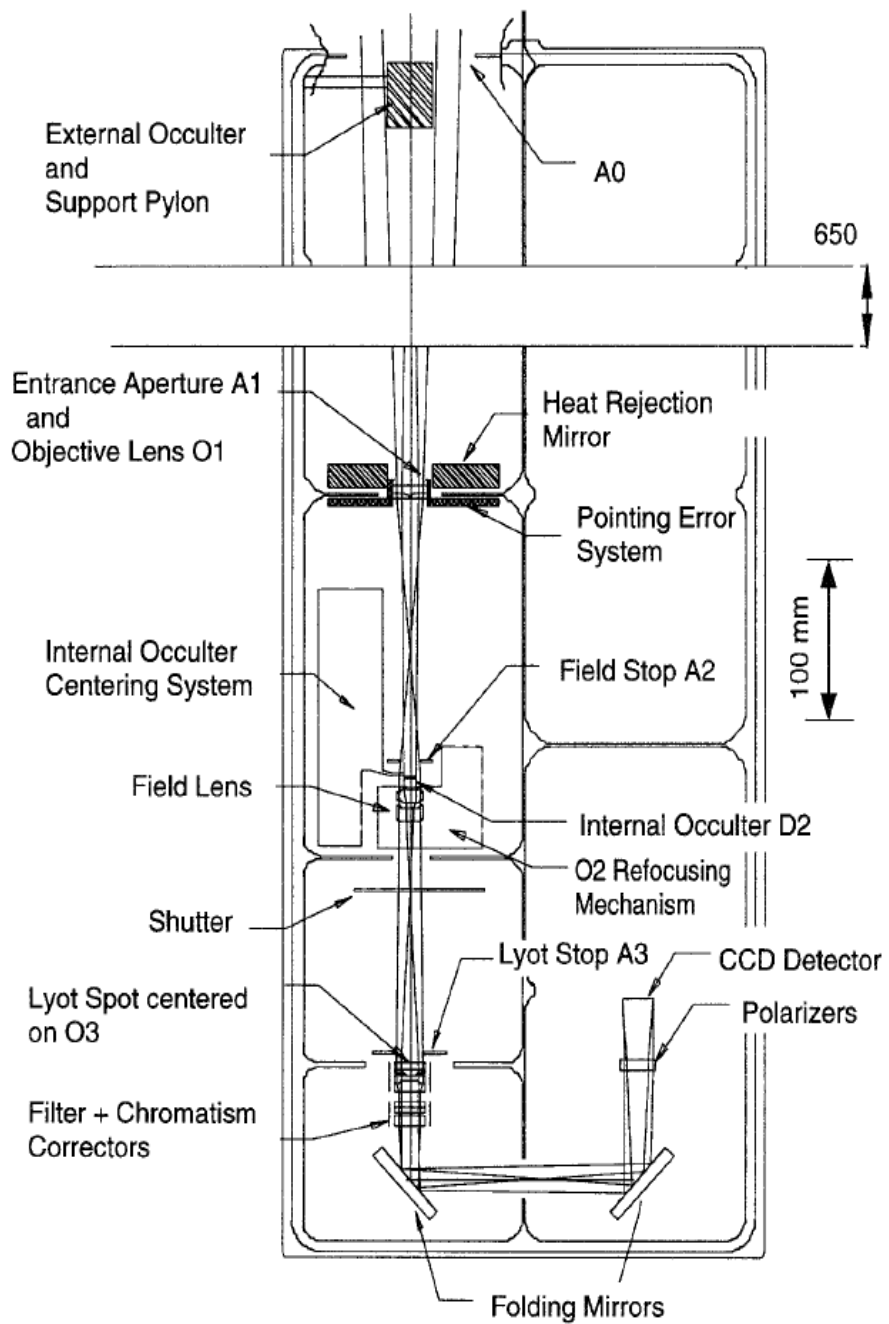
Figure 5.2.   The optical layout of the SOHO LASCO C2 coronagraph.
               Source: Brueckner et al. (1995).

61

Table 5.1. Characteristics of SOHO LASCO C1, C2 and C3 Coronagraphs.

Telescope parameter	C1	C2	C3
Field of view	1.1-3.0	1.7-6.0	3.7-32.0
Occulter type	Internal	External	External
Spectral Bandpass	Fabri-Perot Interferometer (0.07mm)	Broadband	Broadband
Color filter	Fe XIV 530.3 nm Fe X 637.4 nm Ca XV 564.9 nm Na I 589.0 nm H-alfa 656.2 nm	Orange Blue Red H-alfa	Clear Orange Blue Red Infrared H-alfa
Polarization Analyzers	0, 60, -60 linear polarizers	0, 60, -60 linear polarizers	0, 60, -60 linear polarizers
Stray Light	1×10^{-8} B/Bo	5×10^{-11} B/Bo	1×10^{-12} B/Bo
CCD Size	1024x1024	1024x1024	1024x1024
Pixel Size	5.6 arc sec	11.2 arc sec	56.0 arc sec

Source: Howard et al. (1997).

All of the LASCO cameras are identical and use a 1024x1024 CCD with 21 micrometer square pixels. The electron full well capacity of the CCD is approximately 200,000 electrons which are digitalized to 14 bits (16384). The quantization step has been set such that one quantization step is equivalent to about 12 electrons. Since the quantum efficiency is 0.4, the quantization step is equivalent to 30 photons at the detector and the full well capacity is 500,000 photons. Since the total noise of the system in the order of 30 photons per pixel, the dynamic range of the camera is about 16000 (HOWARD et al., 1997).

The LASCO is capable of taking a full image about every 6 minutes, which include preparing the telescope, exposing the CCD, reading out the camera, processing the image and transferring to the telemetry buffer. Downlink of the image take up to 22 minutes for a lossless image. The observation can only be done if the buffer of the image is emptied sufficiently. Thus, a sustained cadence is limited by the telemetry downlink rate (HOWARD et al.,1997).

From June 24, 1998 to November 5, 1998 the contact with SOHO was completely lost and several recovery activities had to be done. During this period, LASCO-C1 was damaged and could not be used anymore since that time. LASCO-C2 and LASCO-C3 are in operation until now.

5.2 The K and F corona

The LASCO C2 and C3 observe basically two spectral components: the k*ontinuierlich* (K) and Fraunhofer (F) corona. Also it is present a stray light component which is very low and constant. The F corona needs to be removed from the images since it is not due to Sun's corona.

The K corona arises from the Thomson scattering of photospheric light by free electrons in the corona. The electric field of the incident light accelerates the particle, causing it to, in turn, emit radiation at the same frequency as the incident wave, and thus, the wave is scattered. The K corona is continuum and partially polarized. Because the emission is optically thin, the observer sees a contribution from electrons all along the line of sight.

The F corona is due to scattering of photospheric light from dust. Beyond 5 solar radii, the polarized contribution of the K corona cannot be ignored (HAYES el al., 2000).

As an illustration, Figure 5.3 shows the relative K and F corona contributions based on the models of Saito et al. (1977) and Koutchmy & Lamy (1985), respectively. Note that the F corona dominates the observed signal beyond ~ 4

solar radii and makes it difficult to recover the much fainter (but very important) K corona signal.
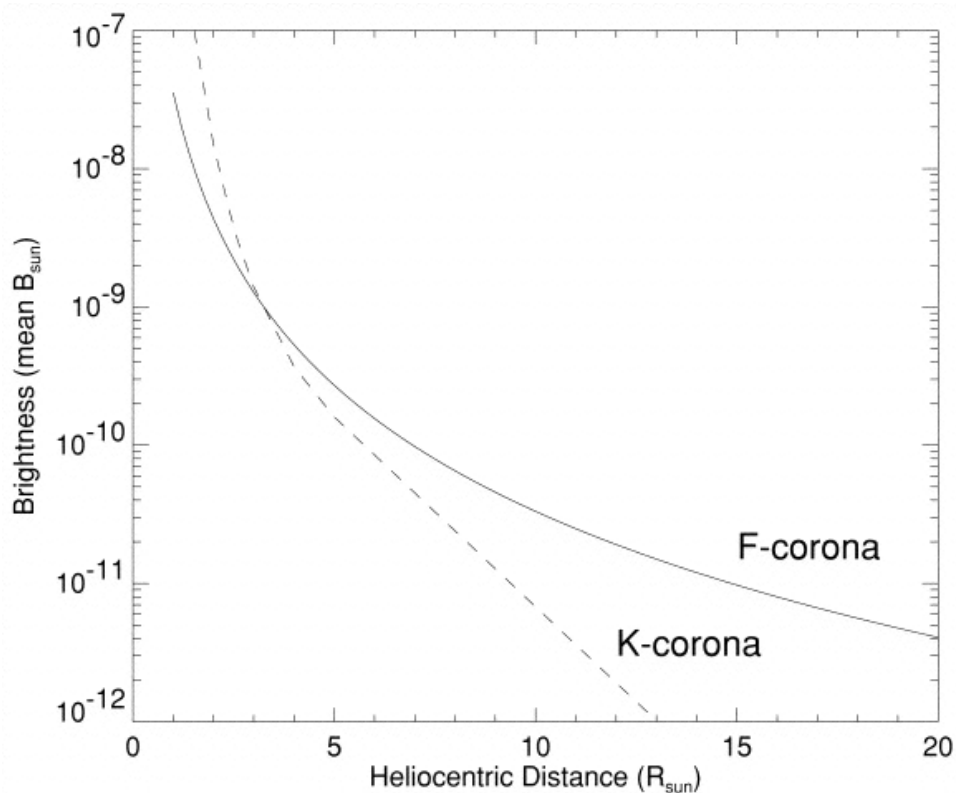
Figure 5.3.   Model equation brightness curves for K corona (Saito et al., 1977) and F corona (Koutchmy & Lamy, 1985). The F corona dominates the observed signal for heliocentric distances larger than about ~4 solar radii.
Source: Hayes el al. (2000).

In order to remove the K-corona, F-corona, and stray light from the images, a background model developed by the Naval Research Laboratory (NRL) was applied to the images. The background consists of the minimum over a 4 week period of daily median images.

5.3 The SOHO/LASCO CME Catalog

Coronal mass ejections identified in the images of solar corona obtained by LASCO since 1996 have been manually measured and their basic attributes are

cataloged in a data base known as the SOHO/LASCO CME Catalog, also known as CDAW catalog because it grew out of a coordinated data analysis workshop (CDAW) in 1999. For each CME many parameters are available like speed, acceleration, mass, kinetic energy, angular width etc. The catalog also has LASCO movies from the events and other parameters from different interplanetary and geomagnetic sources. The catalog is available at: http://cdaw.gsfc.nasa.gov/CME_list/. A general view of the catalog is shown in Figure 5.4 (YASHIRO et al., 2004).
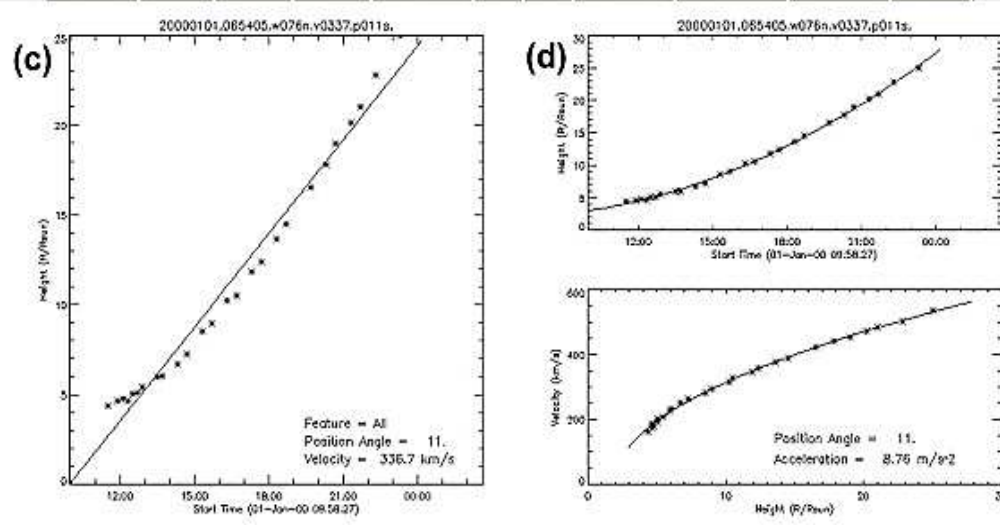
Figure 5.4. (a) Overview of online catalog as a matrix of years and months of observation. (b) A few of the entries in the catalog for January 1st and 2nd 2000. (c-d) Height-time plots in the catalog obtained by linear (left) and for quadratic (right) fits to the measurements (asterisks).
Source: Yashiro et al. (2004).

The catalog is done using the standard LASCO software available, as Interactive Data Language (IDL) routines in SolarSoft, available at http://www.lsal.com/solarsoft/ (Freeland and Handy, 1998), to run movies of LASCO images and measure the increase of height of CMEs as they expand away from the Sun. Typically, running difference images are used to better identify frame-to-frame changes in the corona (YASHIRO et al., 2004).

Any brightness enhancement (white light) moving outward in at least two consecutive LASCO images is defined as a CME. Even in a single LASCO image, if the shape of an enhancement is undoubtedly CME-like (e.g., the enhancement has typical CME three-part structure) it is listed as a CME in the catalog (YASHIRO et al., 2004).

Each CME is characterized by three speeds: 1) the linear speed obtained by fitting a straight line to the height-time measurements made at the fastest section of CMEs, 2) quadratic speed obtained by fitting a parabola and evaluating the speed at the time of final height measurement, and 3) speed obtain as in (2) but evaluating when CME is at height of 20 solar radii (YASHIRO et al., 2004).

From January 1996 to June 1998, St Cyr et al. (2000) identified, measured and listed 841 LASCO CMEs while Yashiro et al. (2004) identified 1084. Comparing differences of the catalogs, 23 CMEs listed in the work of St. Cyr et al. (2000) were not listed in Yashiro et al. (2004) and 265 from Yashiro et al. (2004) were not listed in St. Cyr et al. (2000). Out of the 265, 110 were identified and classified by St. Cyr et al. (2000) as "coronal anomalies". In this event brightness enhancement is detected in the coronal field of view but its outward motion is not clearly observed. Other explanations were also given for other discrepancies but after that no clear reason could explain the discrepancies of 50 events (7% of the total).

If taking a given CME identified by two different observers, in the same period, there are discrepancies between the estimated speeds. All the measurements in the catalog were manually done by visually inspecting the image. There is not any numerical criteria defined that could be applied to the images to know the exact boundaries of the CMEs. This Thesis work aims a more objective way to identify and estimate CMEs characteristics so that different observers could always have the same results since some parameters were specified and kept constant for a given event.

5.4 Automatic CME catalogs

One example of an automated catalog is the Computer Aides CME track (CACTus). CACTus autonomously detects CMEs in image sequences from LASCO C2 and C3. The output of the software is a list of events, similar to the SOHO/LASCO catalog, with principle angle, angular width and velocity estimation for each CME. In contrast to catalogs assembled by human operators, these CME detections, by software, can be faster and possibly also more objective, as the detection criterion is written explicitly in a program. The CME list is automatically generated by CACTus. There is no human intervention or supervision at this stage (ROBBRECHT, BERGHMANS; VAN DER LINDEN, 2009). CACTus is online available at http://sidc.oma.be/cactus/.

A height time map is made to identify the CME, where consecutive running difference images are combined to form a map of height, the distance in solar radii of the leading edge from the Sun (vertical) versus time (horizontal), which was introduced by Sheeley et al. (1999) and which can provide a much better contrast and contains less noise than in images by themselves. In this map, all CMEs are seen as inclined ridges where the inclination can be used for estimating the speed of the CME. A height time map is done for each angle and so a datacube is formed. A sample height time map is shown in the top panel of Figure 5.5.
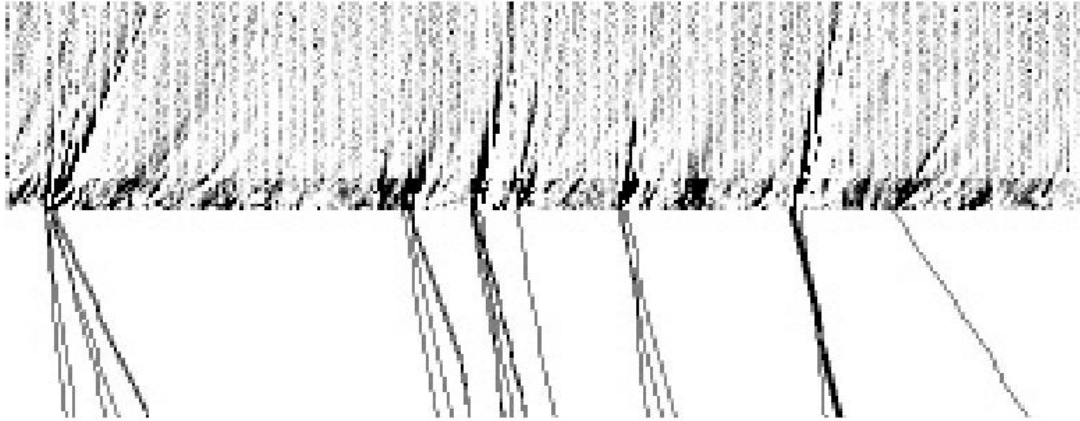
Figure 5.5.   Top: example of a (time, height) slice through the datacube at a given angle. Bottom: the corresponding ridges (set upside down) detected in this slice using the Hough transform. The horizontal range runs from November 9th to 14th 2003. In both panels the vertical range corresponds to the combined C2/C3 fields of view (FOV). The inclination angle of the ridges corresponds to the propagation velocity.
Source: Robbrecht and Berghmans (2004).

For detecting straight lines in noisy data, the Hough transform is used for parameterizing every straight line in the height time plot by two variables t and delta t, t being the coordinate of the intersection point with the time-axis and delta t being the distance in the time axis corresponding to the distance from the start to the end of the CME detection in the coronagraphs field of view. After this, for each angle, velocity and time can be derived and a [v,theta,t] datacube is formed. Finally, the datacube is integrated in the v-direction and clusters in the resulting [theta,t] map are identified (ROBBRECHT; BERGHMANS, 2004).

The output parameters from CACTus is a list of start time, duration, position angle and linear fit of the velocity in each angle over the angular range where the CME was detected, providing the mean, maximum and minimum in the range. Thus, a velocity profile is obtained (ROBBRECHT; BERGHMANS, 2004).

69

The CACTus software found 47 events whereas there are only 16 CME entries in the CDAW catalog. One limitation of CACTUS is that it splits a CME in subsequent events. It also produces some false alerts events which number is controlled by several imposed thresholds (ROBBRECHT; BERGHMANS, 2004).

5.5 Texture based CME tracking

It is clear from the previous sections that there are no universally accepted rules on how to define the boundaries of CMEs and there is a lack of agreement in kinetic properties of CMEs which can be seen both in manual and automatic catalogs. Several techniques to detect and track CMEs have been exercised on white-light coronagraph images (see Robbrecht and Berghmans, 2004; Liewer et al., 2005; Qu et al., 2006; Olmedo et al., 2008) but none of them is based on texture analysis. By human vision, texture analysis is one of the fundamental methods used to discriminate between a background and an object, in this case a CME. This approach, alone or combined with other features (e.g., shape, brightness, motion, etc.), is commonly applied in computer vision to distinguish, characterize, and eventually extract objects in digital images.

The first attempt to detect and track CME was done by Goussies et al. (2009) and Goussies et al. (2010). The work used textures analysis to provide characterization of coronal events both in LASCO C2, C3 and SECCHI-COR2. The authors were able to discriminate the coronal events from the background. The technique was called CORonal SEgmentation Technique (hereafter CORSET) and was run for 7 selected events in 2005 and 2008.

The objective of CORSET is isolate coronal features from the background in a given coronagraph image. In computer-vision terminology, this is called a bipartitioning segmentation problem. CORSET is a supervised procedure to separate the CME from the background. The method used an initial user input to give an initial estimate of the CME boundary in the first image in a series. The

algorithm that traces this boundary as it evolves in a sequence of images, by assigning pixels with common texture characteristics to the CME and the rest to the background (GOUSSIES et al., 2010).

5.6 Image texture

Briefly, image texture is defined as a function of the spatial variation of the pixel intensities (gray values). The problem that texture analysis research attempts to solve is that of the texture segmentation, where the goal is to obtain a boundary map separating the differently textured regions in an image. In 1973, the use of the so-called Gray Level Co-occurrence Matrix (GLCM) was proposed as a mean to capture and therefore characterize the texture of the different regions (HARALICK et al., 1973).

Suppose an image to be analyzed is rectangular and has N_x resolutions cells in the horizontal direction and N_y pixels and the vertical direction. Suppose that the gray tone is quantized to N_g levels. Let $L_x=\{1,2,...,N_x\}$ be to horizontal spatial domain and $L_y=\{1,2,...,N_y\}$ be to the vertical spatial domain, and $G=\{1,2,...,N_g\}$ to be the set of N_g quantized gray tones. The set $L_y \times L_x$ is the set of image resolutions cells of the image ordered by their row-column designations.

One considers a resolution cell – excluding those at the periphery of an image etc. - to have eight nearest-neighbor pixels as in Figure 5.6.
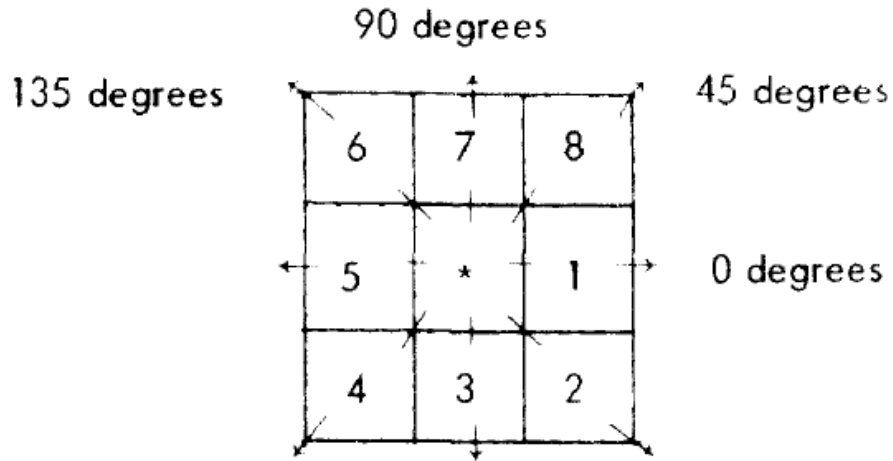
Figure 5.6.   Pixels 1 and 5 are 0 degree (horizontal) nearest neighbors to resolution cell *; resolution cell 2 and 6 are 135 degree nearest neighbors; pixels 3 and 7 are 90 degree nearest neighbors to *.
Source: Haralick et al. (1973).

It is assumed that the texture-context information in an image I is contained in the overall or "average" spatial relationship which the gray tones in image I have to one another. More specifically, one shall assume that this texture-content information is adequately specified by the matrix of relative frequencies P_{ij} with which two neighboring pixels, separated by distance d, occur on the image, one with gray tone i and the other with gray tone j. Such matrices of gray-tone spatial-dependence frequencies are a function of the angular relationship between the neighboring pixels as well as the function of the distance between them. For exemplification, the set of all horizontal neighboring pixels separated by distance 1 is shown in Figure 5.7.

(1,1)	(1,2)	(1,3)	(1,4)
(2,1)	(2,2)	(2,3)	(2,4)
(3,1)	(3,2)	(3,3)	(3,4)
(4,1)	(4,2)	(4,3)	(4,4)

$$L_y = \{1,2,3,4\}$$
$$L_x = \{1,2,3,4\}$$

$$
\begin{aligned}
R_H = \quad & \{((k,l),(m,n)) \in (L_y \times L_x) \times (L_y \times L_x) \mid k-m = 0, \ |l-n| = 1\} \\
= \quad & \{((1,1),(1,2)) \ , \ ((1,2),(1,1)) \ , \ ((1,2),(1,3)) \ , ((1,3),(1,2)) \ , \\
& ((1,3),(1,4)) \ , \ ((1,4),(1,3)) \ , \ ((2,1),(2,2)) \ , \ ((2,2),(2,1)) \ , \\
& ((2,2),(2,3)) \ , \ ((2,3),(2,2)) \ , \ ((2,3),(2,4)) \ , \ ((2,4),(2,3)) \ , \\[8pt]
& ((3,1),(3,2)) \ , \ ((3,2),(3,1)) \ , \ ((3,2),(3,3)) \ , \ ((3,3),(3,2)) \ , \\
& ((3,3),(3,4)) \ , \ ((3,4),(3,3)) \ , \ ((4,1),(4,2)) \ , \ ((4,2),(4,1)) \ , \\
& ((4,2),(4,3)) \ , \ ((4,3),(4,2)) \ , \ ((4,3),(4,4)) \ , \ ((4,4),(4,3))\}
\end{aligned}
$$

Figure 5.7.   Set of all distance 1 horizontal neighboring pixels on 4 x 4 image.
Source: Haralick et al. (1973).

Consider Figure 5.8(a), which represents a 4 x 4 image with four gray tones, ranging from 0 to 3. Figure 5.8(b) shows the general form of any gray-tone spatial-dependence matrix. For example, the element in the (2,1) position of the distance 1 horizontal P_H matrix, is the total number of times two gray tones of values 2 and 1 occurred horizontally, adjacent to each other. To determine this number, we count the number of pairs of pixels in R_H such that the first resolution cell of the pair has gray tone 2 and the second resolution cell of the pair has gray tone 1. Depending on the distance of neighboring pixels and direction, the number of pairs change and a normalization by the number of cells R is needed is needed.
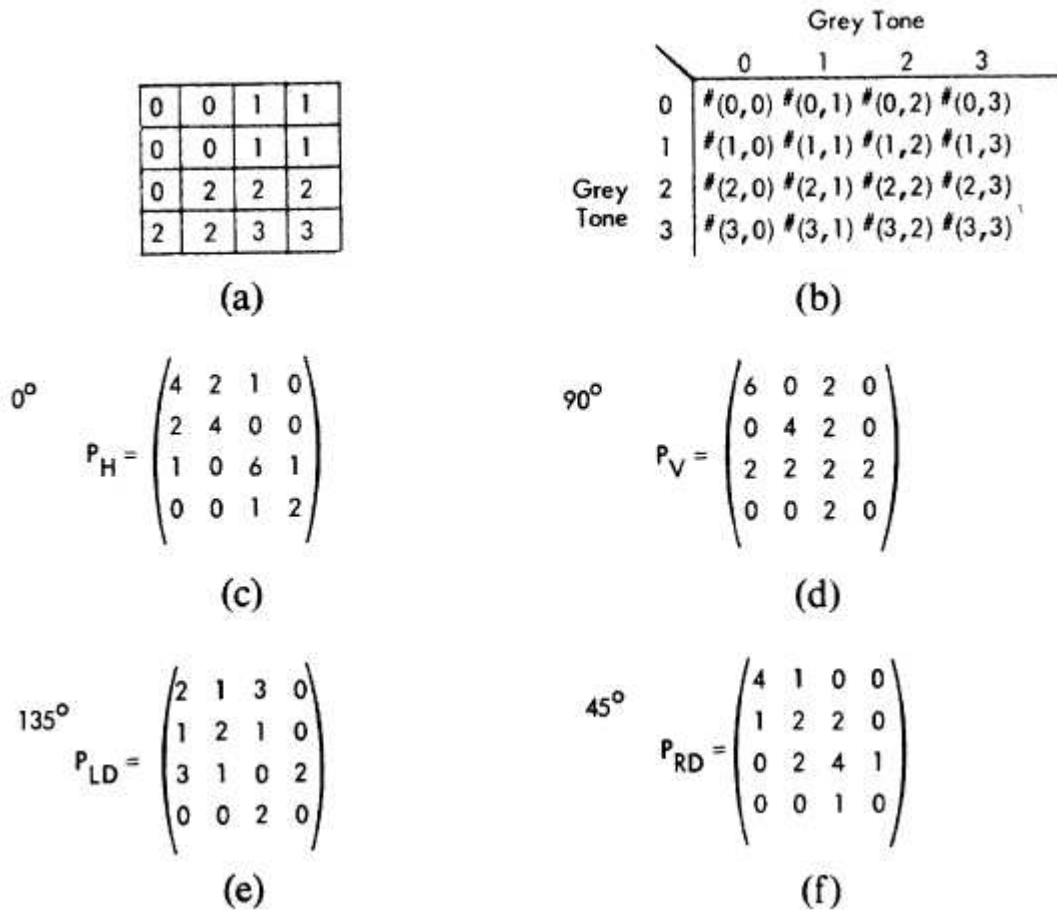
Figure 5.8.   (a) 4 x 4 image with four gray-tone values 0-3. (b) General form of any gray-tone spatial-dependence matrix for image with gray-tone values 0-3. #(i.j) stands for the number of times gray tones *i* and *j* have been neighbors (c)-(f) Calculations of all four distance 1 gray-tone spatial-dependence matrices.
Source: Haralick et al. (1973).

In other words, the GLCM associated with a given region of an image is a matrix that contains information about the distribution of the intensity levels inside the region. The elements of the GLCM are simply the relative frequencies of occurrence of pairs of gray-level values of pixels separated by a given distance and direction. Following the work from Goussies et al. (2010), the GLCM were computed using distance between pixels of one and direction of 45 degrees with size of 4 x 4.

74

5.7 Tracking CMEs with CORSET

CORSET (Coronal Segmentation Technique) does a bipartitioning segmentation to find a set of two regions such that:

a) each region is a subset of the image domain;

b) the region are pairwise disjoint, that is, there is no intersection in the two regions;

c) the union of the two regions covers the whole image domain;

d) the point in each region share common image characteristics.

To discern whether the texture that characterize a given pixel x resembles that of the foreground or that of the background, a chi-square test is made between a given window and the texture of the background and the foreground. Both textures must be computed at the beginning of the process. To create the foreground model, the user must identify the region of interest (i.e., an approximate area comprising the CME feature) in the image when the event is seen. Similarly, a region excluding the CME feature must be identified to the user for the background. This procedure needs to be done by the user manually for each event. The regions are located by delineating with the computer mouse a contour around the feature. Note that the region of interest does not have to exactly follow the boundaries of the feature. The important issue is that the region so defined must include the main texture characteristics of the event. An example of the areas selected by the user is shown in Figures 5.9 and 5.10.
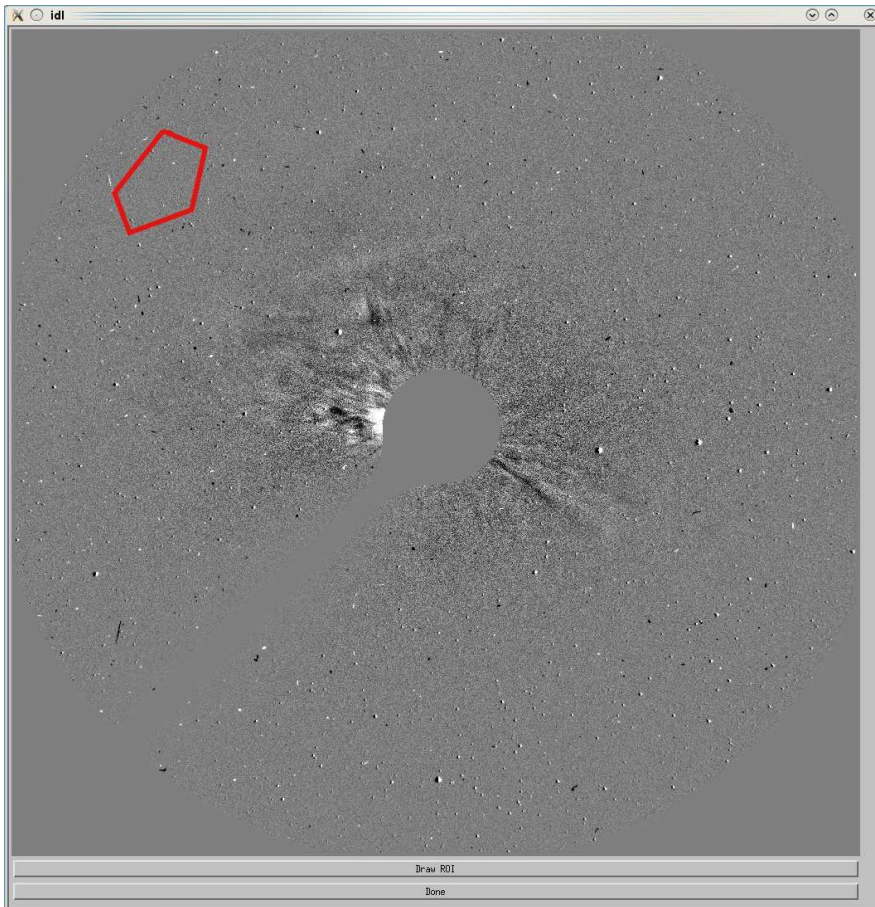
Figure 5.9.   Example of the user-selected areas (inside the red contour) for the background associated to the CME in June 30, 1999. A running difference of the two last images before the first CME appearance on the field of view is used.
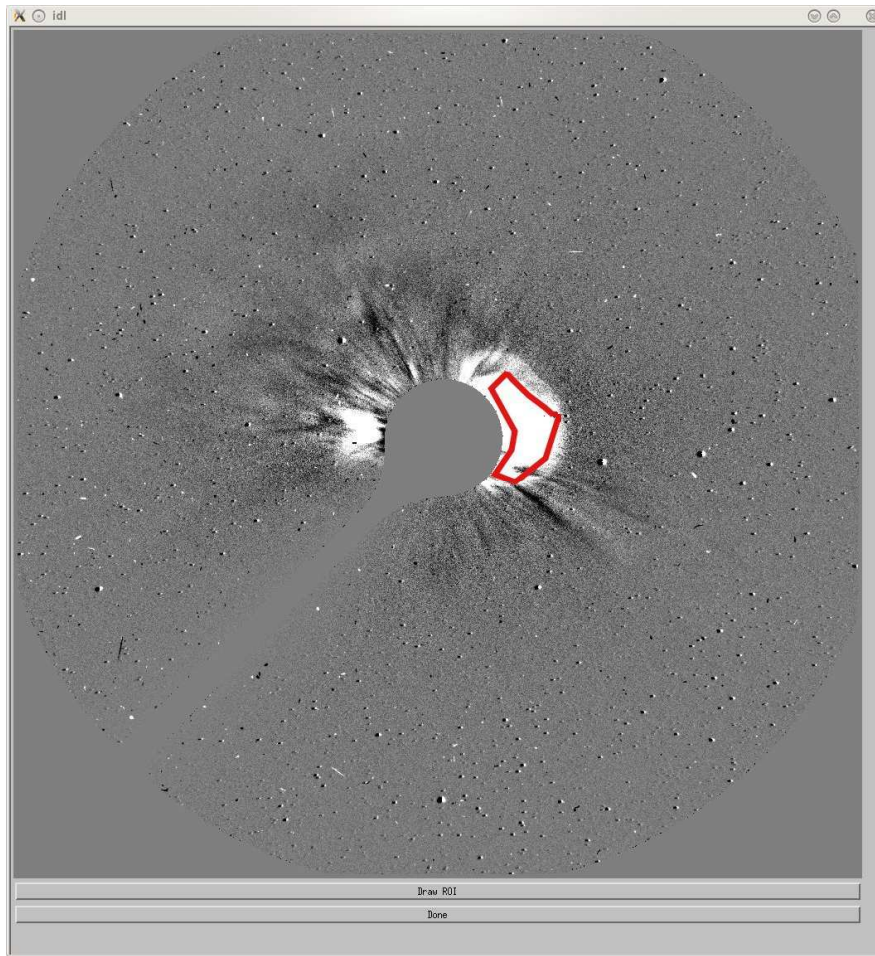
Figure 5.10.   Example of a user-selected area (inside the red contour) for the CME in June 30, 1999. Generally, a running difference of the first two images where the CME on the field of view is used.

Despite of the contour been arbitrarily selected, several tests were made by selecting different parts of the CME and the results found were very similar. So, if all the remaining parameters are the same, even if the areas arbitrarily selected for the CME were different, results from CORSET will remain the same. This is clearly an advantage of CORSET when comparing to catalogs done manually whose results can change if the observer is changed.

As mentioned by Goussies et al. (2000), some events, especially those that start with large speeds, do not keep a similar texture, especially during their

early development. To solve this issue the GLCM of the foreground is re-evaluated in a region corresponding to an expanded version of the region found in the previous frame. The new region is calculated expanding the previous region by *Z/Q* pixels in each direction, where *Z* is the size of the segmented region and *Q* is a used defined parameter between 1 and 60 (hereafter called expansion factor). If *Q=0*, no expansion is performed. In the current Thesis several tests have been made for choosing an appropriate value for *Q.*

The evolving contour using a signed function, where the zero level corresponds to the actual contour, positive values represent a given region and negative values represent the outside of this region, according to the Equation 5.1:

$$\frac{\partial \varphi}{\partial t}(x,t) = \left\| \nabla \varphi(x,t) \right\| \left[\lambda \nabla \cdot \left(\frac{\nabla \varphi(x,t)}{\left\| \nabla \varphi(x,t) \right\|} - \log\left(\frac{\chi^2(M_{\Omega 1}^{d,\varphi}, M_{\Omega 2}^{d,\varphi})}{\chi^2(M_{W(x)}^{d,\varphi}, M_{\Omega 2}^{d,\varphi})} \right) \right) \right] \tag{5.1}$$

where $M_{W(x)}^{d,\varphi}$ is the GLCM of an *m x m* window *W(x)* centered at the pixel x, and $M_{\Omega 1}^{d,\varphi}$, $M_{\Omega 2}^{d,\varphi}$ are the GLCM that captures the foreground and background texture, respectively. The size of the GLCM (s) will depend upon the number of gray-intensity intervals chosen. More details about the derivation of Equation 5.1 can be found in Goussies et al. (2009). For the Thesis work it is used $d = 1$ and $\varphi = 45°$.

A technique that seeks to combine the advantages of both difference-based techniques, from Goussies et al. (2010), was applied. It consists in the suppression of the streamers using running difference and the preservation of the inner morphological structure of the event using base difference. The technique consists of performing a running difference of the boundaries of the feature and a base difference inside it according to equations 5.2:

$$K_j(x) = I_1(x) - I_{base}(x) \text{ if } j = 1$$
$$K_j(x) = I_j(x) - I_{base}(x) \text{ if } j > 1 \text{ and } x \in R_{j-1},$$
$$K_j(x) = I_j(x) - I_{j-n}(x) \text{ if } j > 1 \text{ and } x \notin R_{j-1}$$

$$(5.2)$$

where I_{base} is the base frame, i. e., a frame prior to the first appearance of the event in the field of view of the instrument. Generally *n=2*, except for events faster than 1500km/s.

For the discussed technique all the data used is SOHO/LASCO C3 images with almost no pre-processing (level 0.5). All the images have 1024x1024 pixels. The typical cadence of the image is 40 minutes. The typical processing time in a personal computer is about half a minute for each event.

The inputs parameters that can change the results are:

a) frames to be used for creating a base: a mean of the selected images is used for the base;

b) frames used for tracking of the CME: the first and last frame need to be specified by the user;

c) running difference steps;

d) expansion factor Q;

e) smooth factor;

f) sample area for the background and CME.

Therefore, once specified all the parameters above, the same results can be reproduced by any user even if the sample area for the background and for the CME is not the same.

If parameters are changes, results (like estimated radial speed and expansion speed) not necessarily will be the same. In many tests done in the current Thesis work, with certain parameters no appropriate contour can be found at all. For example, in some cases almost the whole image is selected. In other, only a fraction of the CME is selected. Many tests were done for each event until an acceptable contour is found. There is no criterion for selecting the most appropriate set of parameters.

The outputs of CORSET are:

a) contours in each frame;

b) smooth of the contour;

c) angular width of the tracked CME is each frame;

d) angle of maximum instantaneous velocity;

e) instantaneous velocity for a given angle;

f) position of the contour as a function of time in a given angle;

g) instantaneous velocity as a function of the position along contour;

h) lateral expansion of the CME as a function of time;

i) expansion velocity (calculated by linear and second order fit);

j) radial speed for a given angle (and maximum for any angle).

The items from "c" to "j" were included in CORSET in the present Thesis work. More details about them are described in this chapter and in Chapter 7. As a sample of the outputs, the event in June 30, 1999 is described here in the Thesis work.

Five frames were selected for running CORSET and the contours found are shown in Figure 5.11 and in Figure 5.12. As the contour is quite irregular, a smooth is applied, as in Figure 5.13.
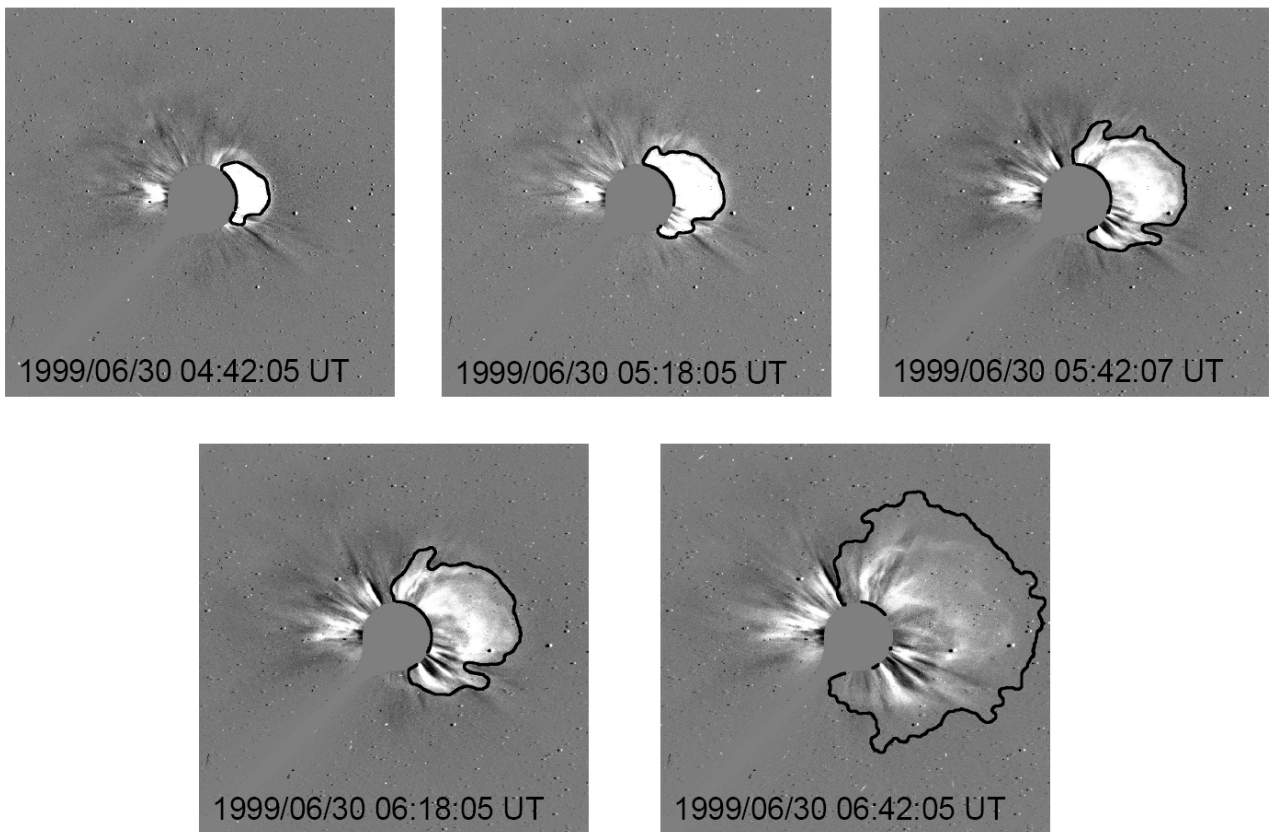
Figure 5.11. The contour found by CORSET in the CME in June 30, 1999.
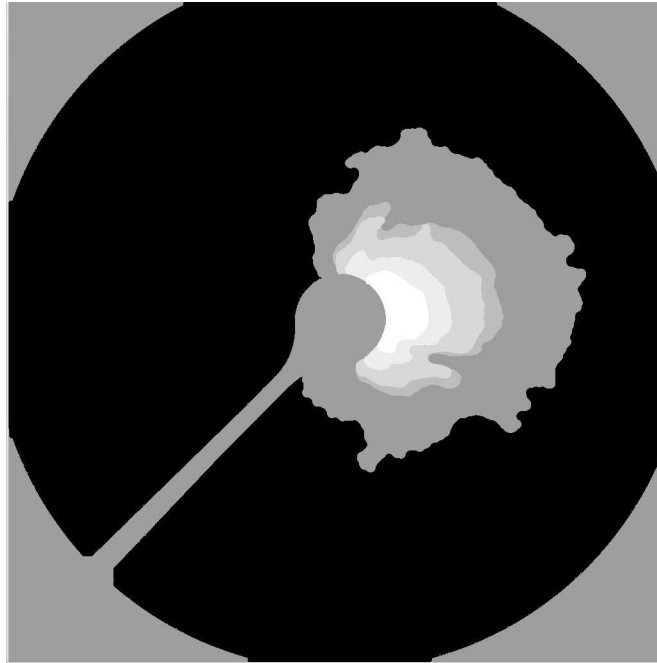
Figure 5.12. Superposition of contour found in the CME in June 30, 1999
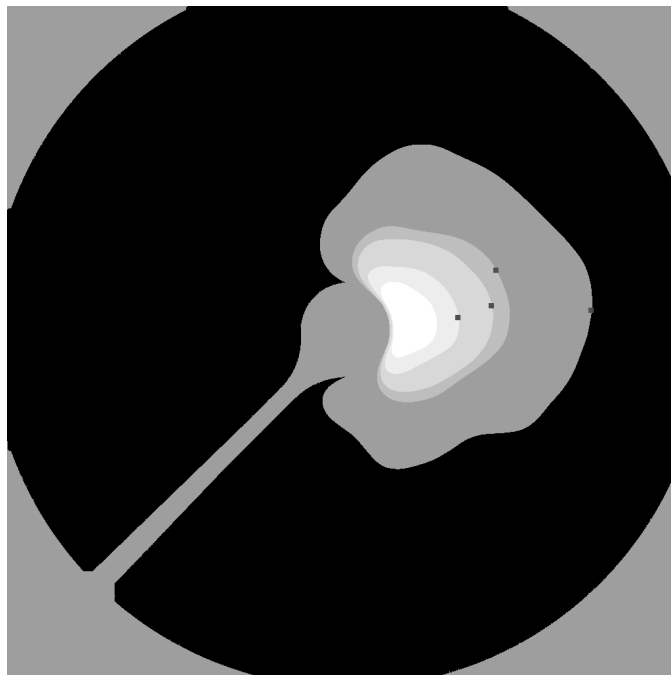
Figure 5.13. Superposition of contour found in the CME in June 30, 1999 (after smoothing). The small squares over each contour show the direction of maximum instantaneous velocity.

5.8 Radial propagation of CME at travel time to 1AU

The radial propagation of CME is discussed by Schwenn et al. (2005). Assuming a constant speed of a shock associated to the CME observed in the SOLWIND coronagraph image, in the Helios 1 and at 1 AU. The travel time to 1 AU was estimated and the following conclusions were reached: a large group of very low starting CME (< 500km/s) arrives substantially earlier than expected, and the majority of CMEs in the group from 750km/s to 1000 km/s arrive later than expected. These results confirmed that slow CMEs are pos-accelerated by the ambient solar wind, and the fast ones are decelerated. However, these were shown to be very scattered. Possible explanations for the scatter were: 1) The CME speeds may not be have good measurement (slow CMEs could be underestimated); 2) Helios 1 was certainly not always hit by the fastest parts of the ICMEs; 3) a delay between the shock and the ejecta, because ejecta follow the shocks a few hours later; and 4) different types of ambient solar wind can made a big deviation a prediction with a simple kinematic model.

CORSET calculates the distance of a point in the contour, in each frame, from the center of the image. By the slope of a linear fit between distance and time, CORSET estimates the radial speed (Figure 5.14). This procedure is done for all angles which have any contour identified. At this point user needs to select a valid angular range. Taking point close to the boundary of the CME could lead to errors and sometimes speeds can be abnormally high. Between these regions, the radial speed versus angle profile has a Gaussian like profile with a

After this, an angular range where the contours of all frames are present needs to be selected by the user. If some frames do not have contour in a given angle, the radial velocity may be overestimated.
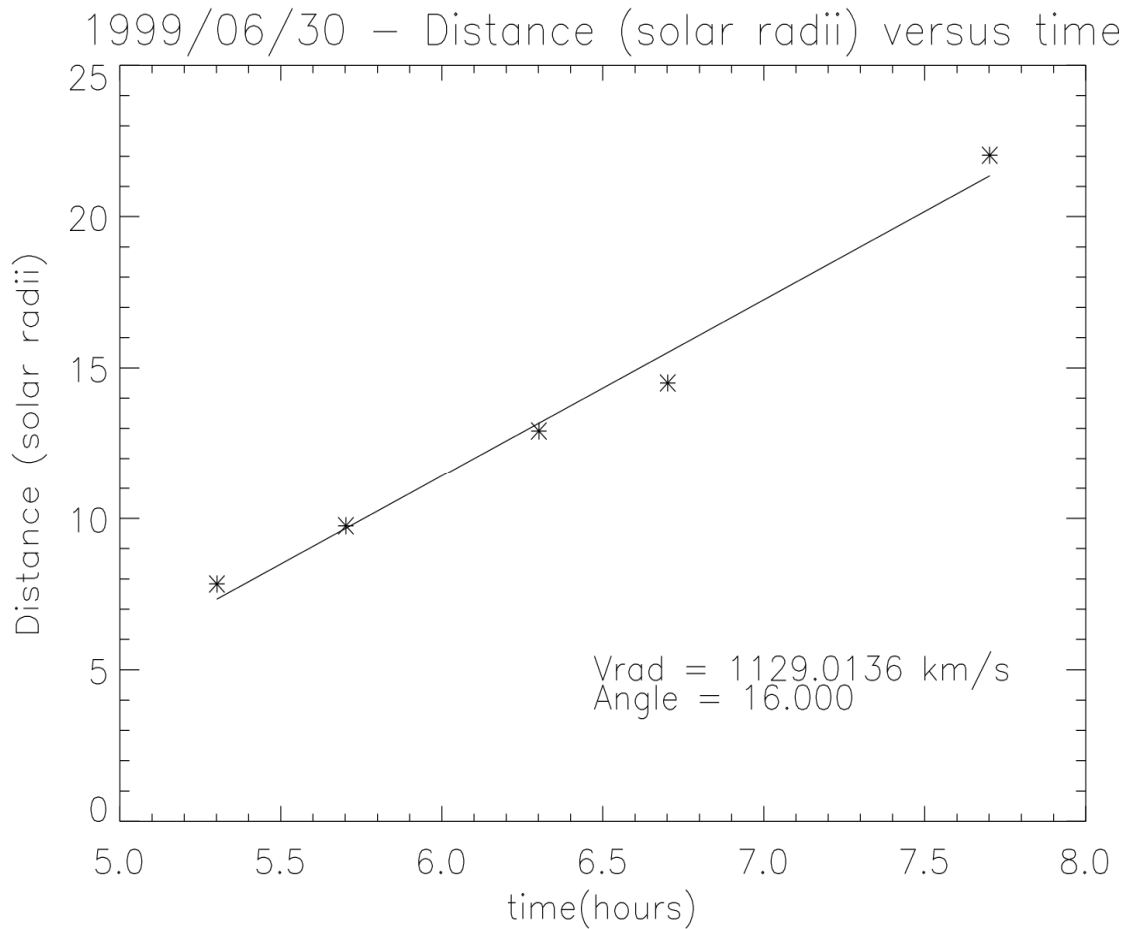
Figure 5.14. Estimation of the radial speed *Vrad* of the CME in June 30, 1999.

5.9 The expansion speed as a proxy for the CMEs radial speed

Schwenn et al. (2005) studied a number of limb CMEs observed by LASCO where the radial speed *Vrad* and the expansion speed *Vexp* could be both measured, in order to check the value of the latter one as proxy data for the other one. Upon inspecting many hundreds of CMEs observed from SOHO, Schween et al. (2005) confirmed the observations by Plunkett el al. (1998) that for limb events the cone angle of expansion and, more generally, the shapes of the expanding CMEs were strikingly maintained (the term "cone angle" mean the angle between the outer edges of the opposing flanks of limb CMEs). The CME shapes remained "self-similar" throughout the LASCO field-of-view. In

other words, the ratio between the lateral expansion and the radial propagation appears to be constant for most CMEs. A typical example is shown in Figure 5.15.
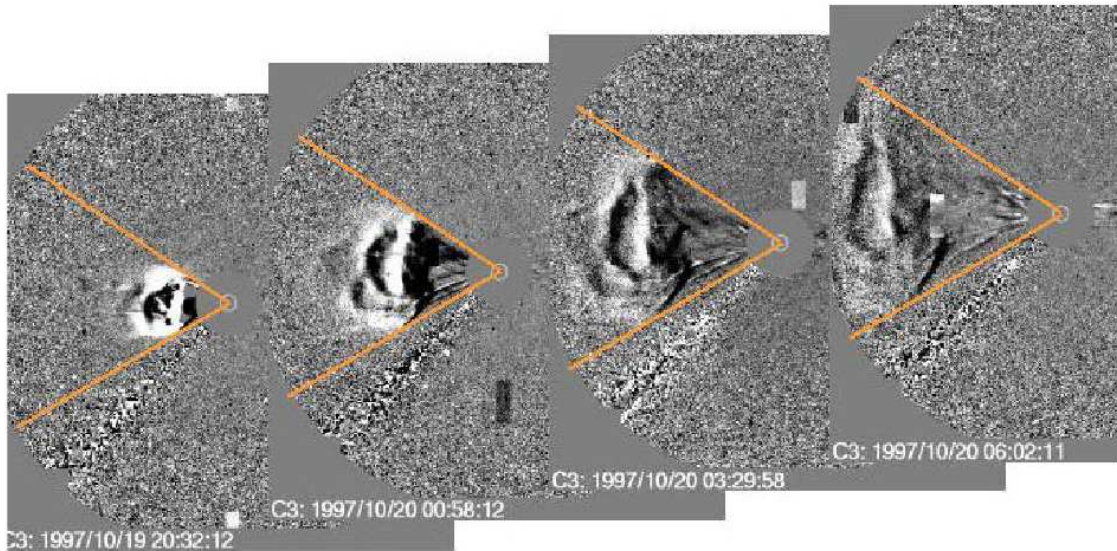
Figure 5.15. Self-similarity of CMEs: the limb CME of October, 19th 1997 is a typical example showing how well the opening angle and the general shape of a CME are maintained, at least up to 32 solar radii. The term "cone angle" denotes the angle between the outer edge of opposing flanks of limb CMEs. It would amount to 65 degrees in this case. The images are running differences between LASCO-C3 images.
Source: Schwenn et al. (2005).

The way to determine the radial speed and expansion speed of a CME is illustrated in Figure 5.16. A set of 57 limb CMEs where EIT images showed a uniquely associated erupting feature within 30 degrees, in longitude to the solar limb and within a reasonable time window of a few hours. Further, sufficient coverage in C3 images was required. For those events, both the radial speed of the fastest feature projected onto the plane of the sky and the expansion speed measured across the full CME in the direction perpendicular to *Vrad* were determined. They were measured when they had reached constant values, i.e., usually at around 10 solar radii. Hereafter, the results of this set of CMEs will we referred as D2005.

The list of the events is presented in Table 5.2 and the results are shown in Figure 5.17. A fairly good correlation between the two quantities was obtained. A linear fit through the data yields:

$$Vrad = 0.88 \cdot Vexp \qquad (5.3)$$

with a correlation coefficient of 0.86. Apparently, the correlation shown in Figure 5.17 holds for the slow CMEs, as well as for the fast ones, for the narrow ones, as well as for the wide ones. The correlation even holds in the extreme cases where a cloud expands faster than it moves as a whole; the front motion would then mainly be due to the expansion alone, where the cone angle amounts to 180 degrees and *Vrad* would be about equal to *Vexp*, in fairly good agreement with Equation 5.3. An example of the limb CME of April 20th 1998, is shown in Figure 5.17. This was an extremely fast event right behind the west limb with *Vrad=1944 km/s* and *Vexp=1930 km/s* and a cone angle of 170 degrees.
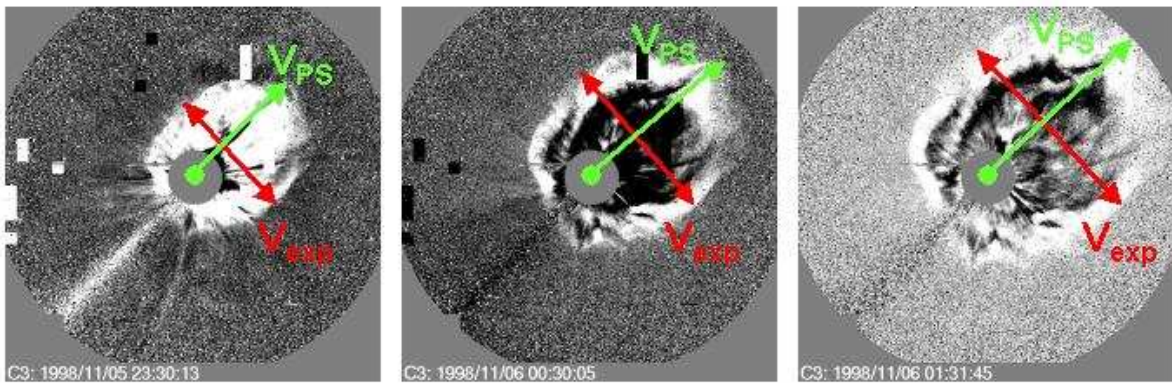
Figure 5.16.   Determine the radial speed (green arrow, Vps) and the expansion speed (red arrow, Vexp) in running difference images of LASCO-C3 in three consecutive frames.
Source: Schween et al. (2005).
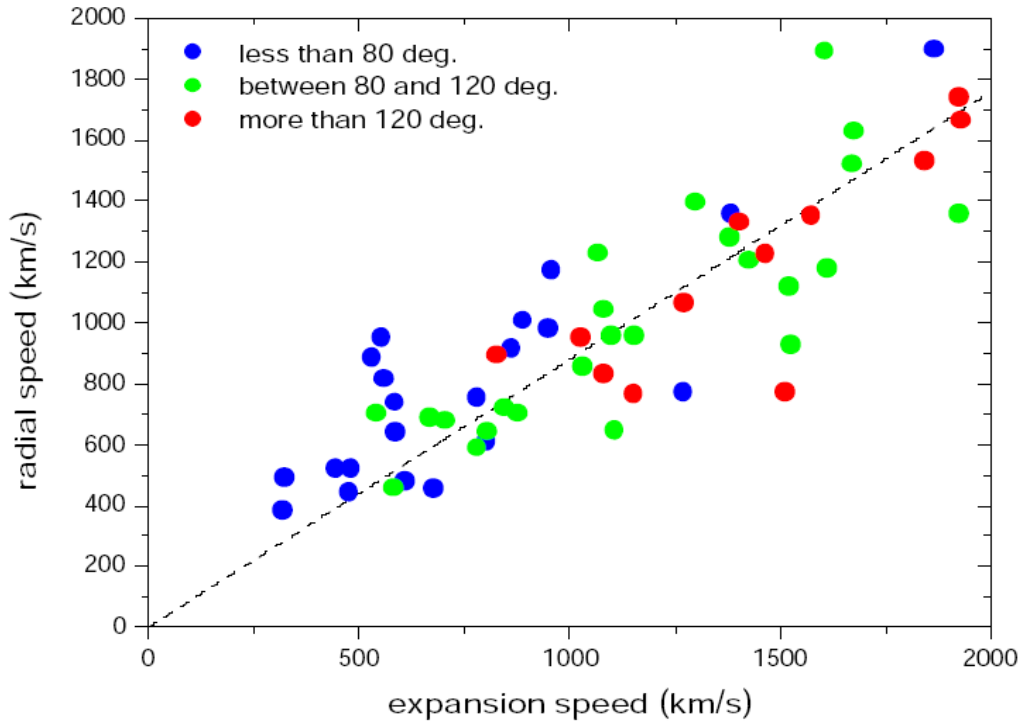
Figure 5.17.   The correlation between radial CME speed Vrad and the lateral speed
                Vexp for limb CMEs observed by LASCO between January 1997 and
                April 15th 2001.
                Source: Schwenn et al. (2005).

Table 5.2. List of limb events analyzed by Schwenn et al. (2005), hereafter D2005.

Event number	Day (DD/MM/YYYY)	Time of first observation at C2	Position angle	Radial speed (km/s)	Expansion speed (km/s)
1	14/11/1997	10:14:00	70	980	951
2	18/03/1998	07:33:00	99	719	847
3	20/04/1998	10:07:00	275	1664	1930
4	23/04/1998	05:55:00	105	1522	1672
5	09/05/1998	03:35:00	285	1892	1607
6	27/05/1998	13:45:00	270	588	781
7	11/06/1998	10:28:00	90	1230	1069
8	16/06/1998	18:27:00	270	1629	1676
9	08/05/1999	14:50:00	300	854	1032
10	02/06/1999	21:26:00	310	701	878
11	11/06/1999	11:26:00	70	926	1526
12	14/06/1999	12:50:00	145	640	588
13	30/06/1999	04:30:00	275	1045	1081
14	25/07/1999	13:31:00	280	1205	1427
15	08/09/1999	11:54:00	230	488	325
16	21/09/1999	03:30:00	320	1172	957

(continues)

Table 5.2. Conclusion

Event number	Day (DD/MM/YYYY)	Time of first observation at C2	Position angle	Radial speed (km/s)	Expansion speed (km/s)
17	03/03/2000	02:30:00	219	701	541
18	03/03/2000	05:30:00	130	830	1082
19	18/03/2000	23:54:00	115	1357	1384
20	21/03/2000	09:06:00	328	383	320
21	04/04/2000	16:32:00	325	1739	1927
22	05/04/2000	00:06:00	212	951	553
23	08/04/2000	15:54:00	231	477	611
24	11/04/2000	20:30:00	211	738	585
25	18/04/2000	14:54:00	209	677	706
26	23/04/2000	14:54:00	285	1280	1381
27	27/04/2000	14:30:00	275	1008	889
28	04/05/2000	11:26:00	215	1117	1523
29	05/05/2000	15:50:00	205	1356	1925
30	15/05/2000	08:50:00	71	1531	1843
31	15/05/2000	16:26:00	230	1226	1466
32	27/05/2000	19:31:00	90	915	862
33	02/06/2000	04:30:00	90	520	444
34	02/06/2000	20:30:00	75	647	1107
35	21/06/2000	19:31:00	240	455	679
36	23/06/2000	14:54:00	289	949	1028
37	27/06/2000	10:54:00	325	458	582
38	28/06/2000	19:31:00	265	1350	1576
39	12/07/2000	02:50:00	90	752	779
40	02/08/2000	17:54:00	40	642	805
41	03/08/2000	08:30:00	285	957	1100
42	13/08/2000	06:06:00	295	893	828
43	29/08/2000	07:54:00	220	520	481
44	30/09/2000	18:06:00	107	609	804
45	16/10/2000	07:27:00	270	1330	1404
46	22/10/2000	00:50:00	125	958	1155
47	30/10/2000	18:06:00	120	886	530
48	02/11/2000	16:26:00	305	688	668
49	14/11/2000	08:30:00	135	441	477
50	23/11/2000	21:30:00	140	1066	1274
51	03/12/2000	05:50:00	285	763	1152
52	14/01/2001	06:30:00	327	771	1270
53	28/01/2001	15:54:00	265	770	1513
54	03/02/2001	00:03:00	82	815	560
55	11/02/2001	01:31:00	279	1178	1613
56	02/04/2001	22:06:00	255	1900	1867
57	15/04/2001	14:06:00	253	1397	1300

Source: Private communication with Alisson Dal Lago (2010).

In order to calculate the expansion speed, for each frame the following steps are done for all frames:

- an angular range where the CME is located is selected by searching for point in the contour: if two points are present in a given angle, this angle is included in the angular range;

- the radial distance from the center of the Sun to the outer contour is computed in the CME angular range. The direction of maximum radial distance is called *R* (see Figure 5.18). A plot of the radius versus angle is plotted in Figure 5.19 for all the frames (the asterisks are the points extracted from the contour). Separately for each frame a second order fit and a smooth is applied (continuous and dashed line in Figure 5.20, respectively);

- the direction of the expansion is determined by two points located in opposite sides of *R* both with the same radius. The distance between these points is computed for radial distances with steps of 5 pixels and the maximum *E* is chosen and called expansion of each frame.

The expansion speed is then estimated by the slope of a first and second order fit of *E* versus time. An example is shown in Figure 5.22 and Figure 5.23. Three ways to determine the contour are adopted: the points obtained previously by CORSET (*Vexp_dat,* the asterisks in the plots), the smoothed contour (*Vexp_smo,* the dashed line in the plots) and a parabolic fit of the contour (*Vexp_par,* the continuous line in the plots).
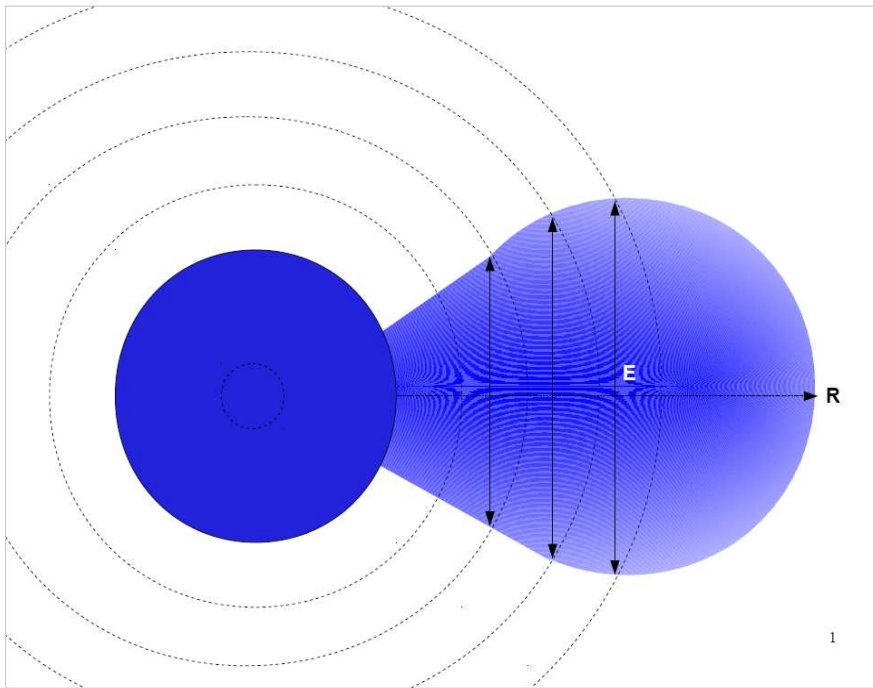
Figure 5.18.   Sketch explaining how the expansion *E* of each frame is obtained if *R* is determined. Once *E* is obtained for each frame, the expansion speed can be estimated.
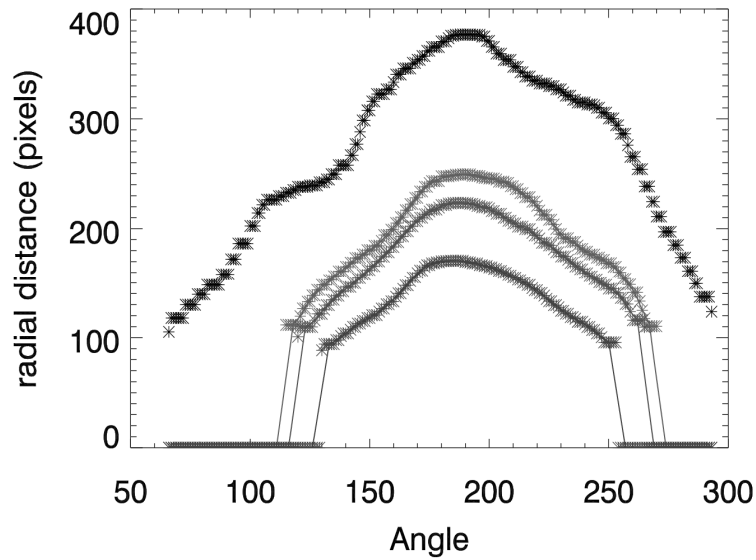
Figure 5.19.   Radial distance (pixels) versus angle (degrees) for the four frames in the CME in June 30, 1999. In these plots the reference of the angle is between the third and forth quadrant of the image (left of the image).
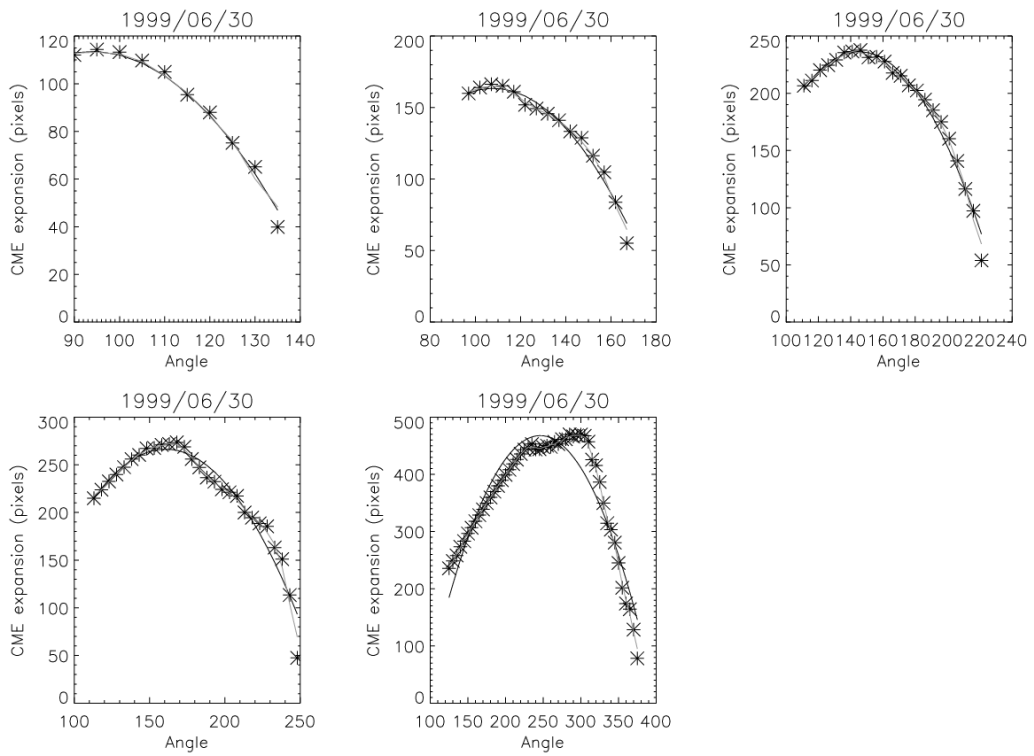
Figure 5.20. Radial distance ("CME expansion") in pixels versus angle (degrees) for each frame. In this plot the reference of the angle is between the third and forth quadrant of the image (left of the image).

91
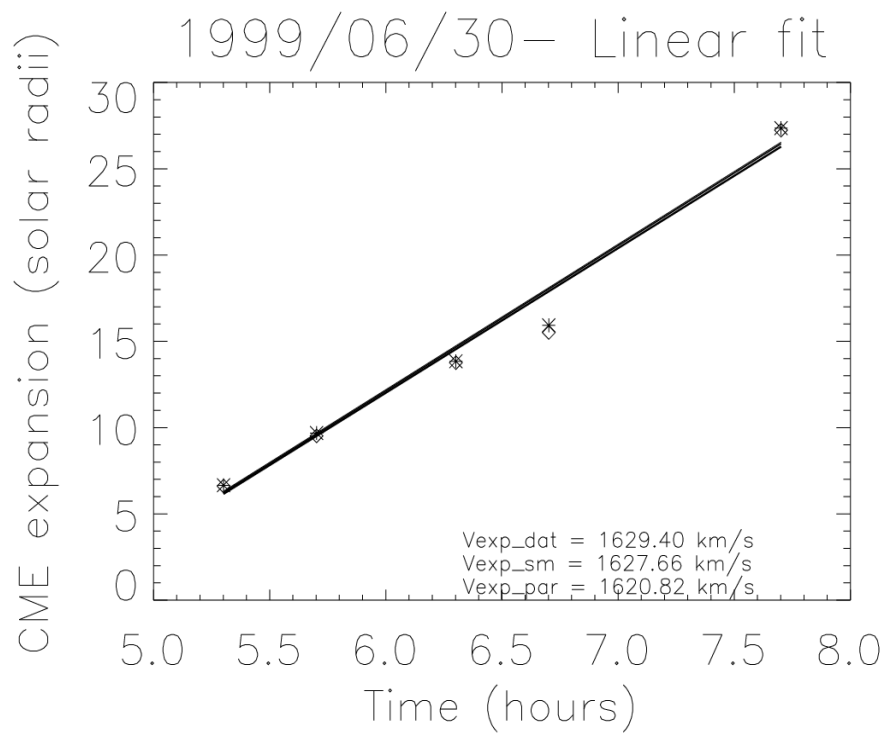
Figure 5.21. The expansion speed of the CME in June 30, 1999 by linear fit.
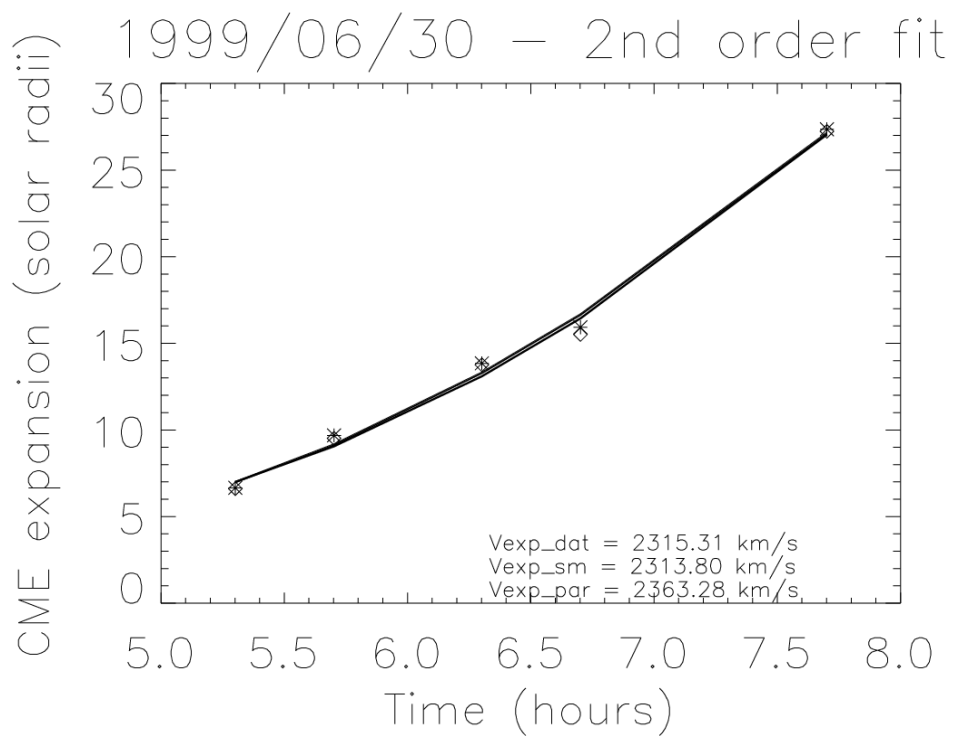
Figure 5.22. The expansion speed of the CME in June 30, 1999 by second order fit.

6 RESULTS FROM GMDN

In Chapter 6, the results of the search for precursors of weak and moderate geomagnetic storms that occurred in 2008 are presented and discussed. Some papers like Gosling et al. (1990), Nagashima et al. (1992), Munakata et al. (2000) and Da Silva (2009) have done similar analysis but the events used were selected according to the maximum Kp index, or in association with interplanetary shocks. In this Thesis work many events studied were not associated with interplanetary shocks and the events were selected according to the Disturbance Storm-Time (Dst) Index.

All the geomagnetic storms from February 12th 2008 to December 31st 2008 are analyzed in this Thesis adopting the criteria for geomagnetic storms classification by Gonzalez et al. (1994): i) small if the minimum Dst index is not lower than -30 nT and ii) moderate if the minimum Dst index is not lower than -50 nT. None of the storms have Dst index lower than -100 nT so there is no intense geomagnetic storms in the period. The Kp index maximum in the period is below 6+. All the events are associated with at least one storm sudden commencement (SSC) and the onset of the SSC was used as the storm onset time. The 16 events found are presented in Table 6.1. For all the 16 events no significant Forbush Decrease was observed by the GMDN.

In order to correct the temperature effect, all the previous works described above used only the first order anisotropy. This Thesis work is probably the first attempt to look for precursors of moderate and small geomagnetic storms using high atmosphere temperature data combined with the first order anisotropy.

Table 6.1. List of geomagnetic storms from February 12th 2008 to December 31st 2008 analyzed in this Thesis. All the events are associated with at least one storm sudden commencement (SSC) and the onset of the SSC was used as the storm onset time.

Event number	Date	Time (UT)	Kp peak
1	2008/03/08	11:42	6-
2	2008/03/26	09:36	5
3	2008/04/04	15:03 15:10	5-
4	2008/04/15	13:40	4
5	2008/04/22	17:22	4+
6	2008/04/30	15:57	5-
7	2008/05/28	02:24	4-
8	2008/06/14	12:23	6-
9	2008/06/24	20:10	4
10	2008/07/12	00:38	4+
11	2008/08/08	23:44	5+
12	2008/09/03 2008/09/03	06:40 15:42	6
13	2008/09/14	19:13	4-
14	2008/11/07	03:53	4+
15	2008/11/15	16:25	4-
16	2008/11/24	23:51	4-

Two ways to show the pitch angle distribution versus time are adopted. One is called "muon pitch angle" (hereafter MPA) which uses the deviation after all the corrections described in Chapter 4. The other which is called "variation pitch angle" (hereafter VPA) uses the difference between the deviation at a time t and the previous one at the time $t-1$ and is meant to emphasize sudden variations in the count rate generally associated to interplanetary shocks.

All the pitch angle distributions presented in Chapter 6 show a 24-hour period preceding the SSC in two different panels. The upper panel shows the results from the application of the MPA methodology while the lower shows the results

from the application of the VPA methodology. Each bubble in the figures represents the data in a directional channel as a function of the pitch angle (ordinate) and time before the SSC (abscissa). For each bubble, the red (blue) color denotes a decrease (increase), while the diameter is proportional to the magnitude of the normalized data. The bigger the magnitude of a positive (negative) deviation, the bigger the diameter of the blue (red) bubble. For size comparison, the black bubble shows a sample diameter for the deviation with intensity indicated besides the bubble. The 0^0 pitch angle corresponds to the sunward direction along the IMF while the 180^0 correspond to the anti-sunward direction along the IMF. All the pitch angle distributions from this point on follow what is described in the current paragraph.

The results from the application of the MPA and VPA methodologies for the event number 16 in November 24th 2008 are shown in Figure 6.1. The MPA shows two systematic decreases: one for small pitch angles about ~15 hours before the SSC and other for big pitch angles a few hours before the SSC.
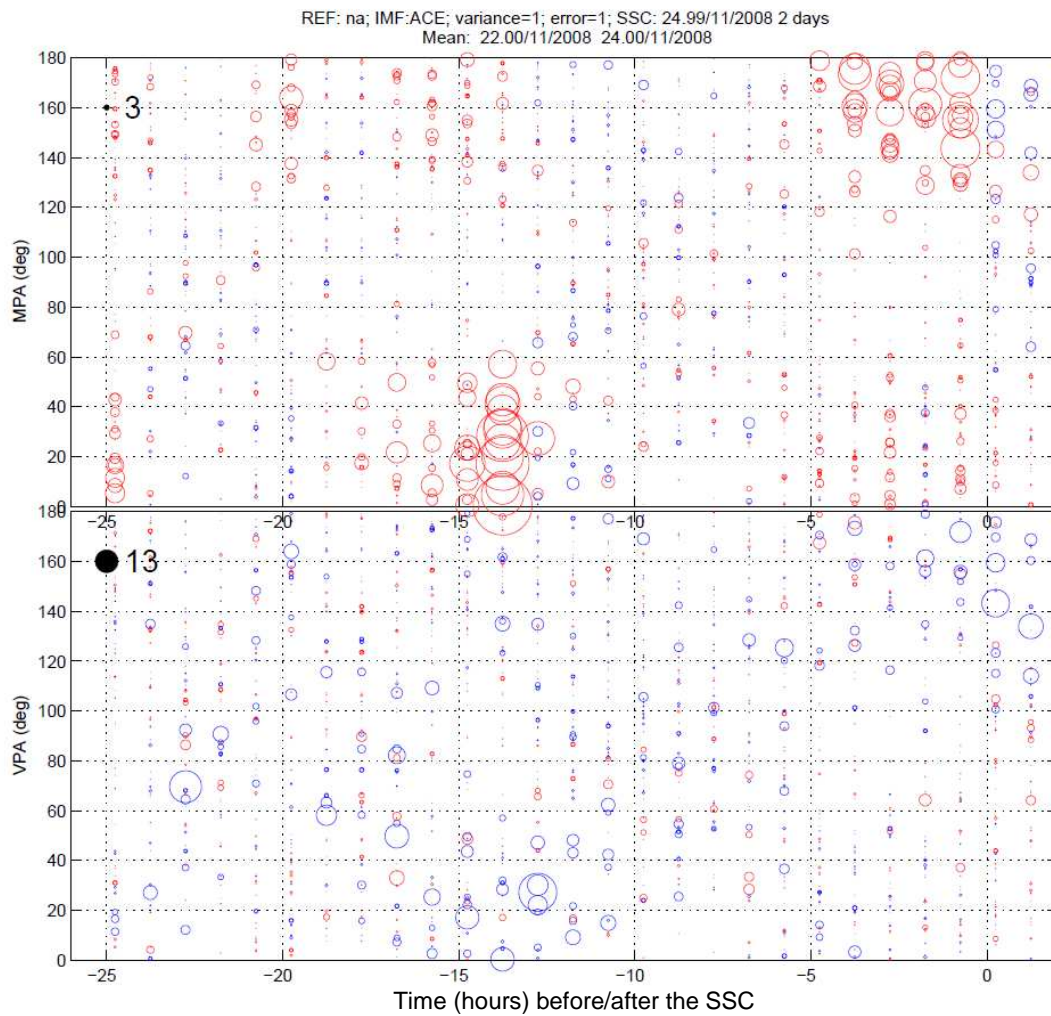
Figure 6.1.   Pitch angle distributions for the application of the MPA and VPA methodologies on the event #16 dataset, observed in November 24th 2008.

For event #15, the pitch angle distributions are shown in Figure 6.2. In this event, two systematic decreases can be identified: one around the anti-sunward direction (large pitch angles) ~5 hours before the SSC and the other, between 10 h and 5 h before the SSC, around the sunward direction (small pitch angles).
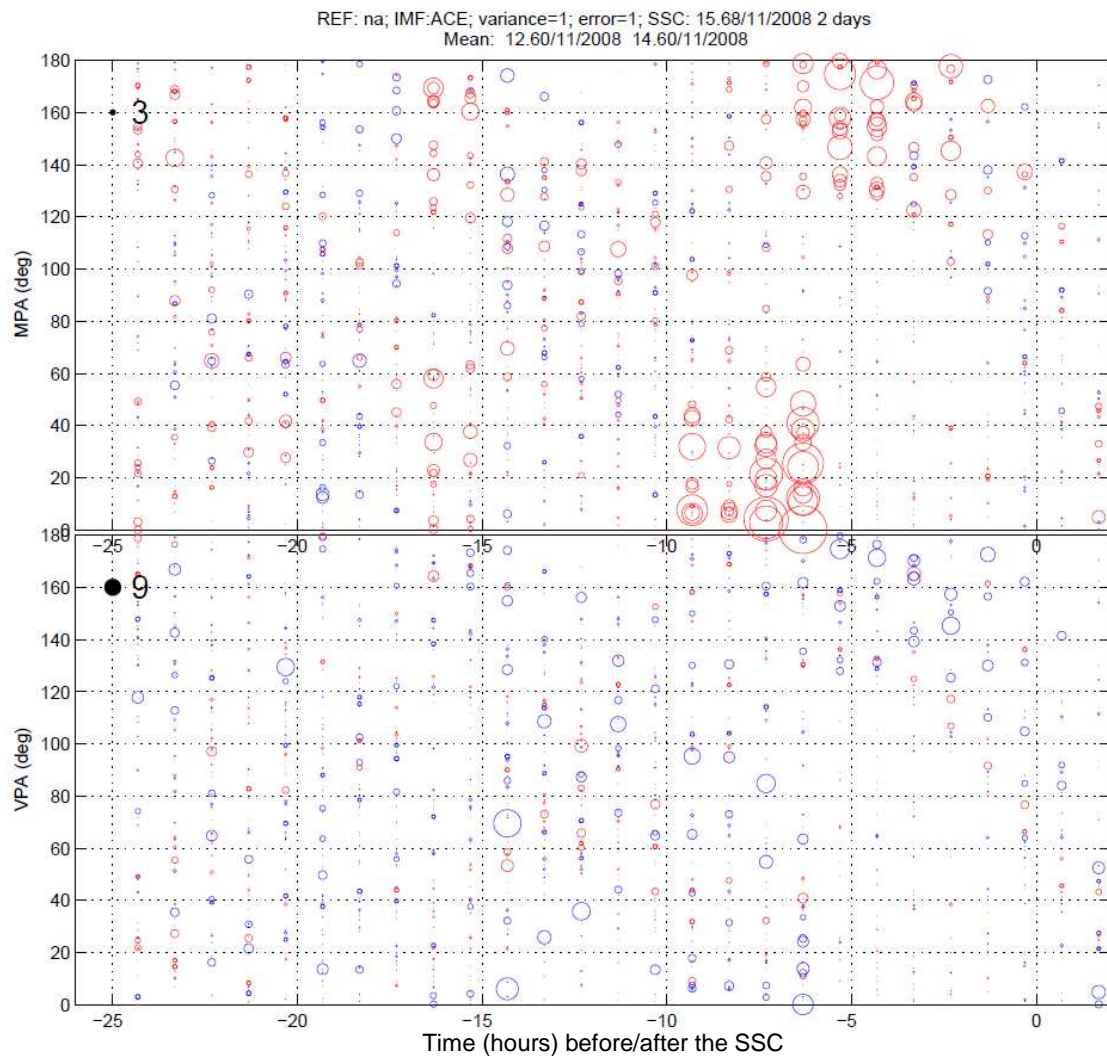
Figure 6.2.   Pitch angle distribution for the application of the MPA and VPA methodologies on the event #15 dataset, observed in November 15th 2008.

In many events a loss cone (LC) effect as described by Munakata et al. (2000) can be identified, as is the case of events #15 and #16. The LC is characterized by an intensity decrease confined in a small pitch angle region around the sunward IMF direction. Figure 6.3 shows a possible LC for 3 events.
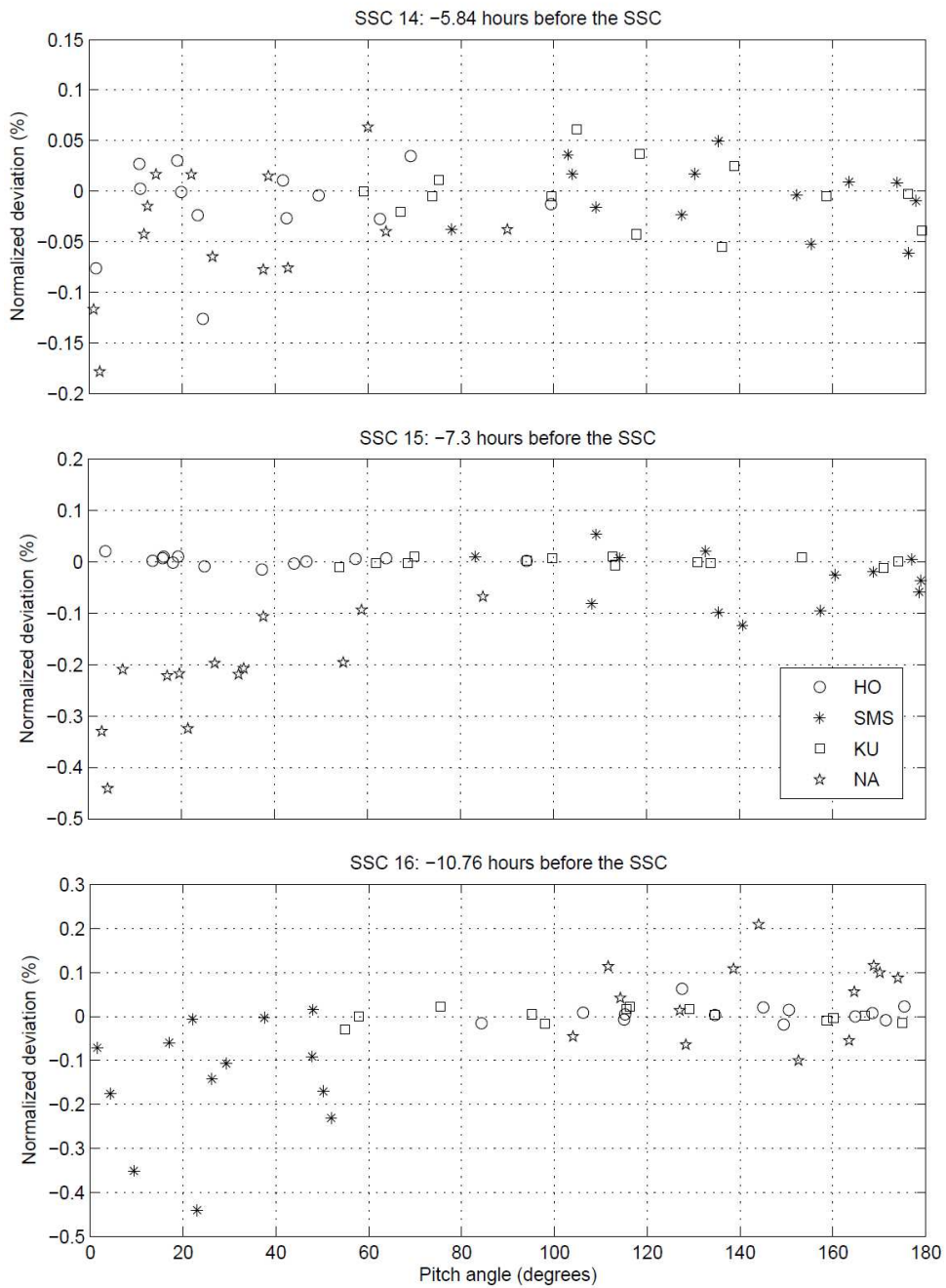
Figure 6.3.   A loss cone effect can be seen before the SSC in some events such as #14, 15 and 16 (from the upper to the lower panels). Each marker represents a different directional channel and different types of markers represent different detectors (see legend in the panel in the middle). For each event, the normalized deviation is plotted for a selected period of one hour which is indicated over each panel.

In events number #3 and #11 (Figure 6.4) no clear systemic increase and/or decrease can be seen. If one takes just the data at 5th hourly period before the SSC, a possible signature of a LC can be identified. As it lasts no more than one hour, it will not be considered as a possible signature in this Thesis work. Until now there is no reason why in some events signatures are very clear (for example, event #15) and in others not. A first idea would be that the IMF magnitude is lower in these events than in the others. Looking at ACE data, the maximum magnitude of the IMF after the SSC is ~10 nT for the event #3 and ~20 nT for the event #11, while it is ~10 nT for the remaining events. Therefore, there is no clear direct influence of the magnitude of the IMF.

REF: na; IMF:ACE; variance=1; error=1; SSC: 4.63/ 4/2008 2 days
Mean: 1.50/04/2008 3.60/04/2008
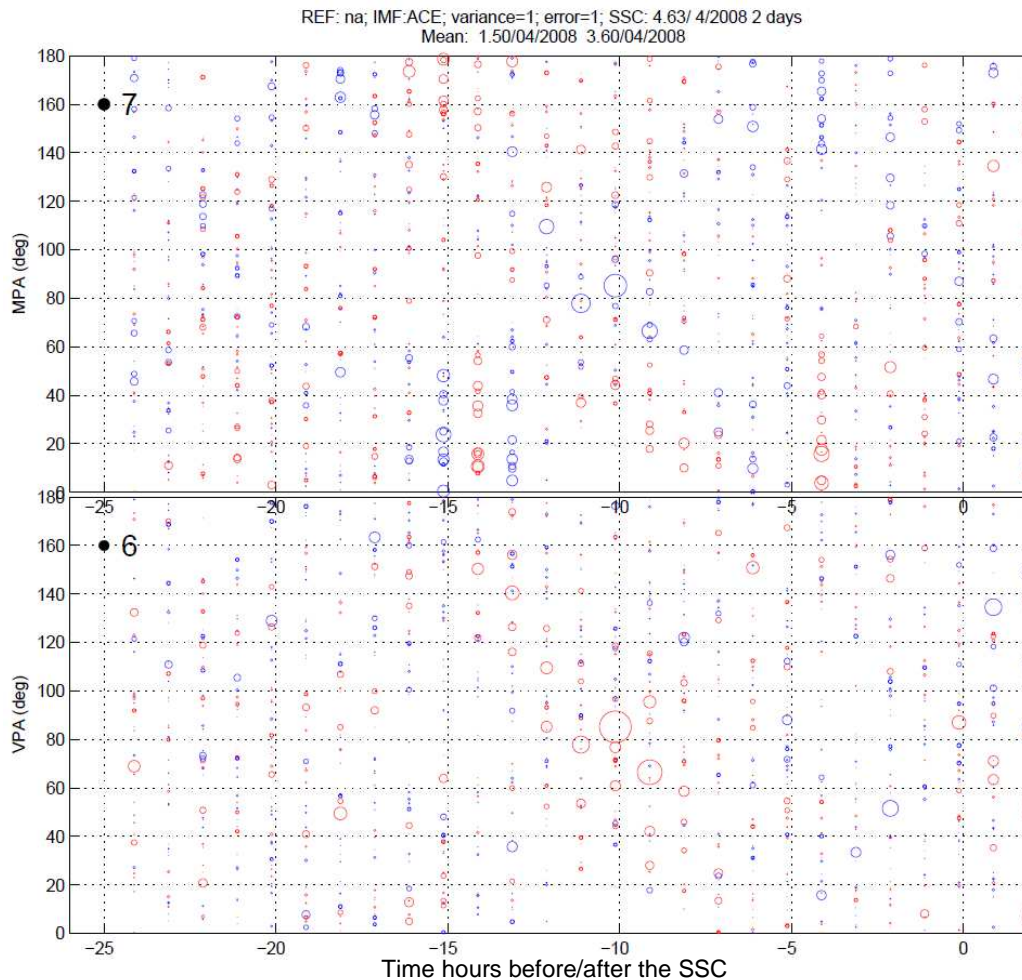
Figure 6.4. Pitch angle distribution for the application of the MPA and VPA methodologies on the event #3 dataset, observed in April 4th 2008. No clear systematic increase/decrease can be seen in this event as well as in event #11.

Systematic decreases can be seen in the majority of the events, sometimes accompanied with systematic increases in lower amplitudes. In the other way, systematic increases can be seen in some events such as: #2, #4 (Figure 6.5), #5, #10 and #13. It is common to explain the increases on the amplitude of the observed cosmic ray by the reflection of particles upstream of the shock. Using muon detectors, this effect has first been observed in detail by Fushishita et al. (2010).
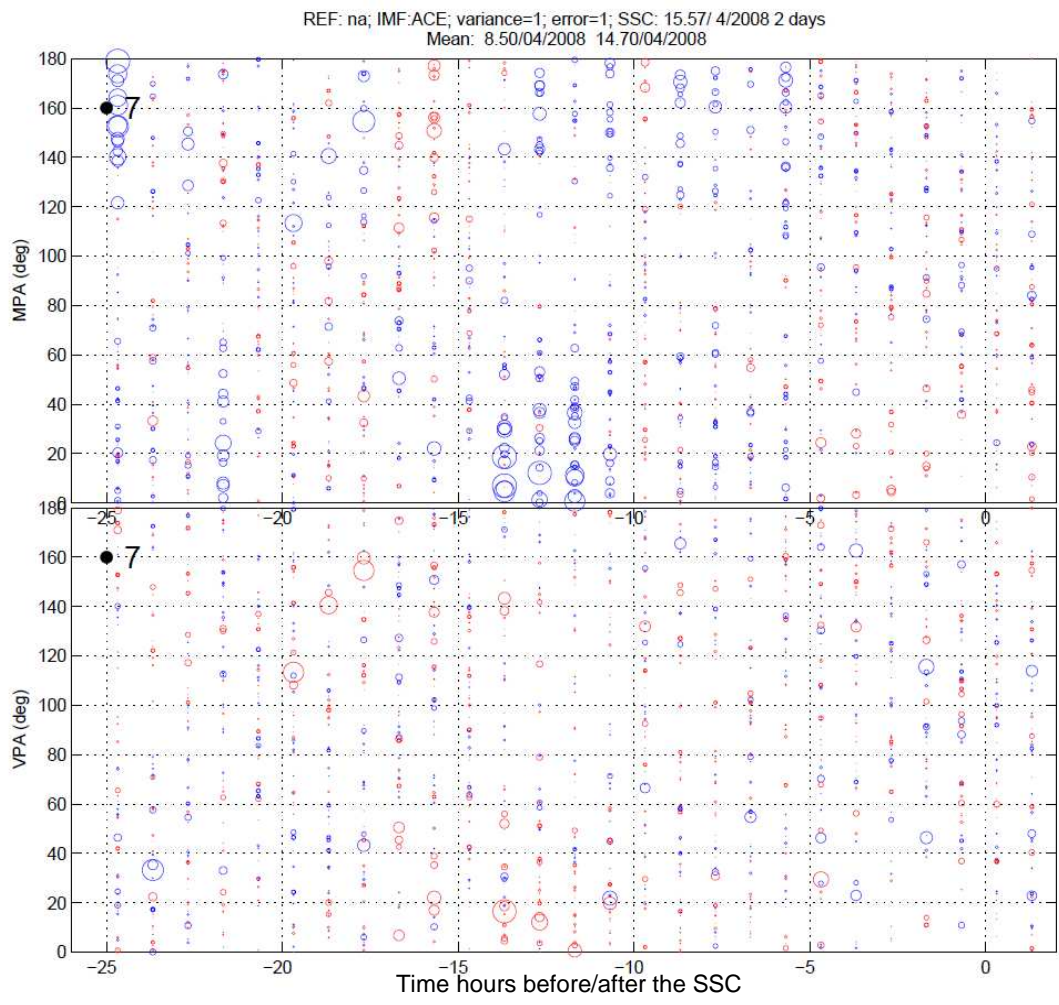
Figure 6.5.   Pitch angle distribution for the application of the MPA and VPA methodologies on the event #4 dataset, observed in April 15th 2008. A systematic increase can be observed between 15 and 20 hours before the SSC in the sunward direction.

In all the pitch angle distributions Figure plots, no systematic behavior can be clearly identified in the results obtained by the application of the VPA methodology. Previous attempts to use VPA were successful to show some signatures for the same event in a similar way than MPA shows. These attempts did not use the trailing moving average (TMA) or the first order anisotropy or any other temperature correction. More attempts to produce VPA methodology with TMA and first order anisotropy are needed. It is hoped than VPA methodology uses difference of the count rates in two consecutive hours,

as the temperature in the atmosphere do not change dramatically in two consecutive hours, the temperature effect is partially removed from the data.

Up to now it is not clear whether is better to use the IMF data or use the Parker model for calculating the pitch angle distribution of cosmic ray. Regarding the large gyro radius of cosmic ray, it is expected that the particles will only follow the average behavior the IMF direction and that short time fluctuations will not affect the direction of the cosmic ray. Some previous works (see Fushishita et al. 2000) chose the Parker nominal field for this reason. Others always used the hourly mean of the IMF direction (see Da Silva, 2009 and Munakata et al., 2000).

For each event in Table 6.1, the MPA methodology result was plotted using both the daily mean and the hourly mean of the IMF direction observed *in situ* by ACE spacecraft. For 10 events (#1, 3, 4, 5, 6, 9, 10, 13, 15, 16) the results of the MPA methodology are very similar when using both periods for the mean, see Figure 6.6 for event #13 and Figure 6.7 for the hourly IMF direction. For four events (#2, 7, 12, 14) some systematic decreases/increases are not present when plotting the results obtained by the MPA methodology with hourly mean IMF, but can be visualized when using daily mean of the IMF, see Figure 6.8 and Figure 6.9, which show event #12. Differently, for events #8 and #11 the hourly mean seems to be better, see Figure 6.10 and Figure 6.11 for event #8.
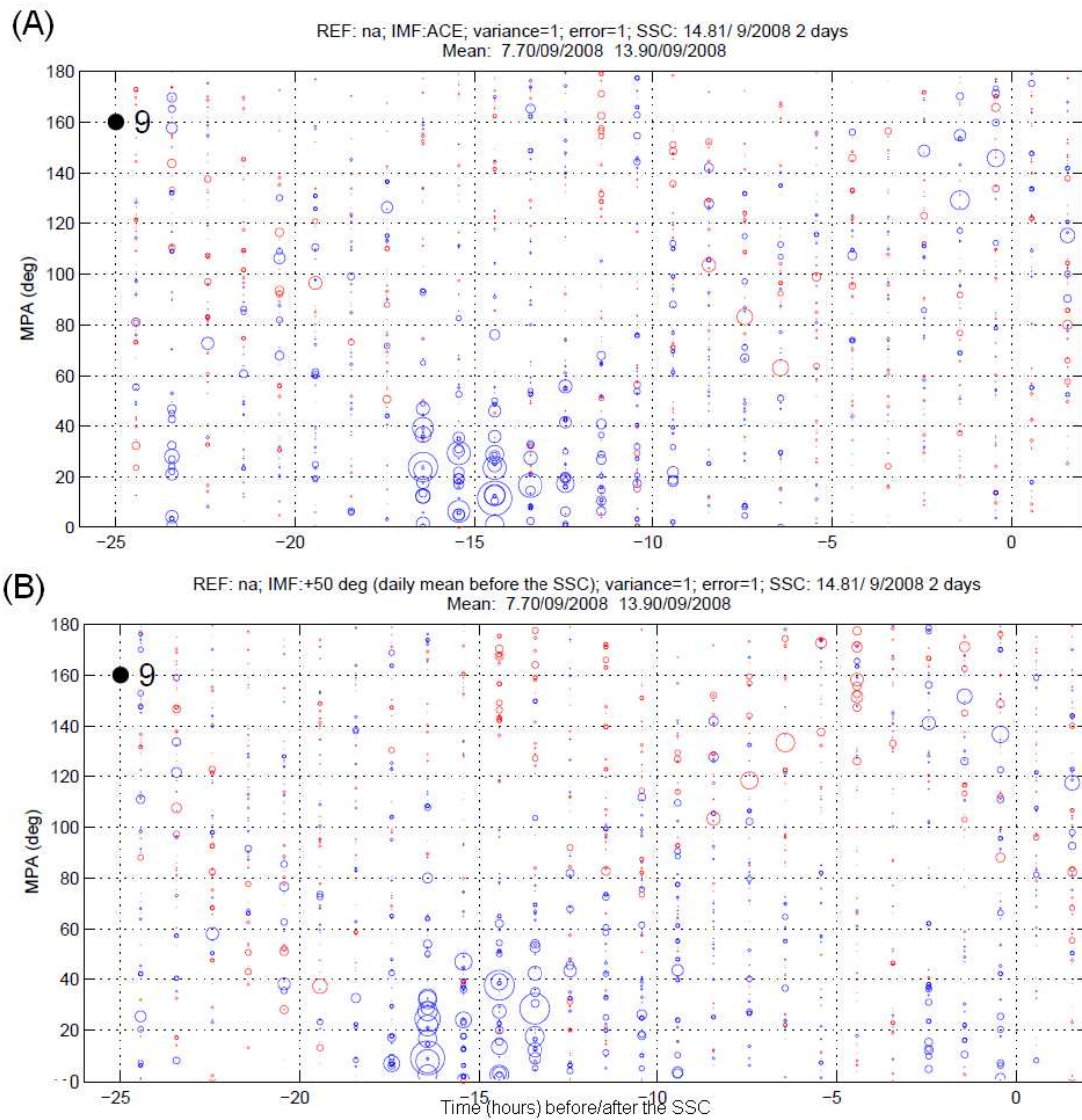
Figure 6.6. Comparison the results obtained from the MPA methodology with hourly (A) and daily (B) mean of the IMF direction for event #13 dataset, observed in September 13th 2008. Both panels are very similar.

103
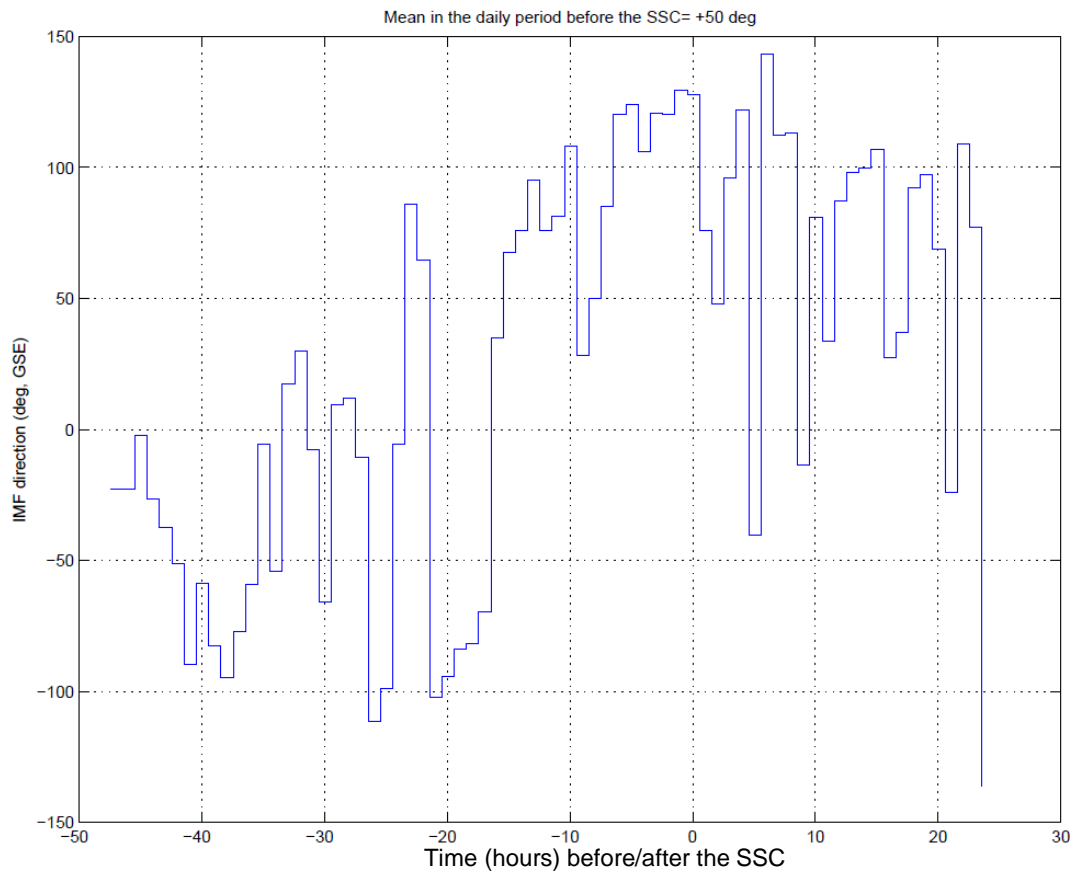
Figure 6.7.   The hourly IMF direction for event #13 observed in September 13th 2008. The mean direction in the daily period before the SSC is +50º.
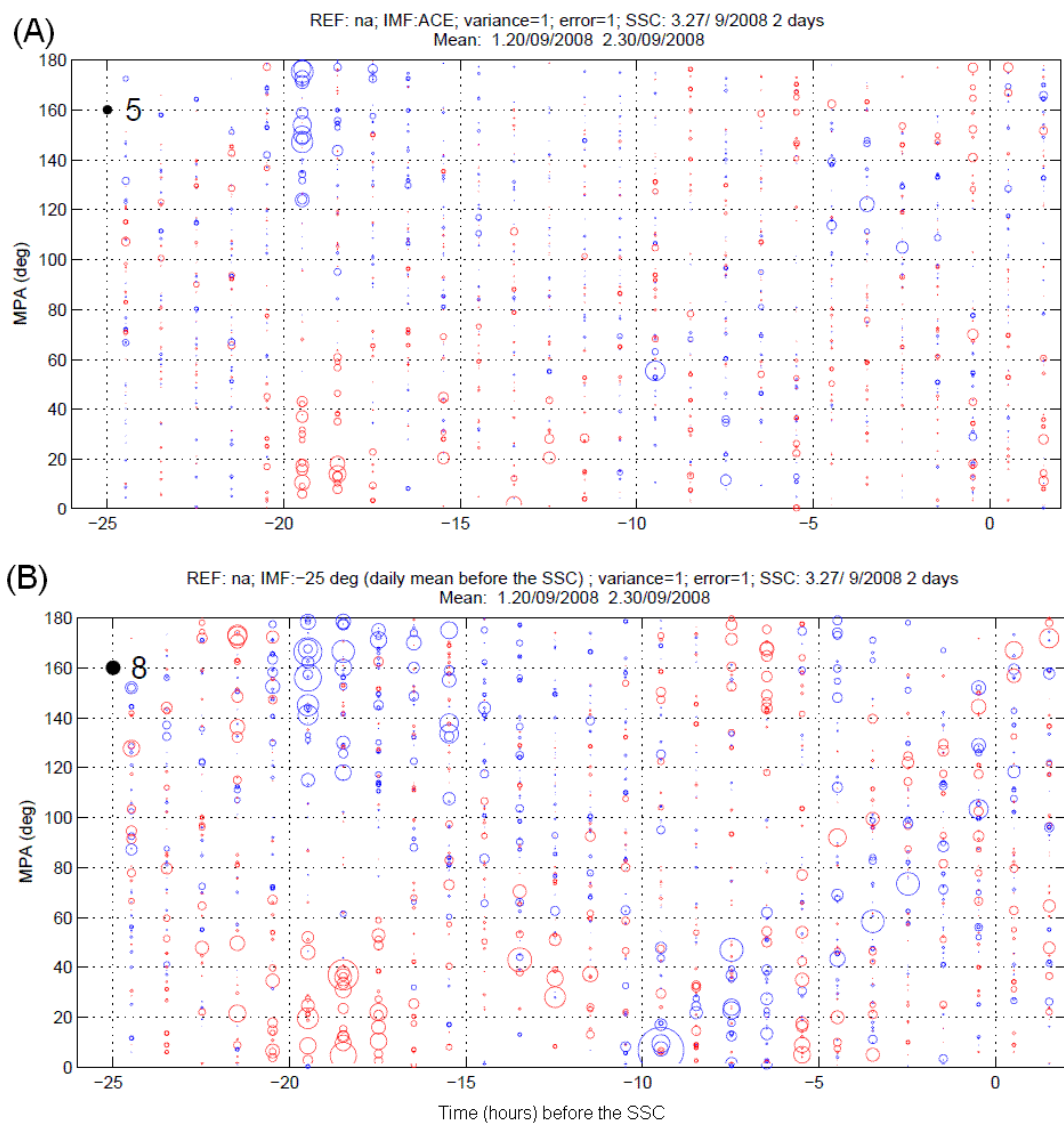
Figure 6.8. Comparison of the results obtained by theMPA methodology with hourly (A) and daily (B) mean of the IMF direction for event #12 dataset, observed in September 3rd 2008. While a loss cone signature is clear between 20 and 15 hours before the SSC in panel (B), it is not clear in panel (A).

105
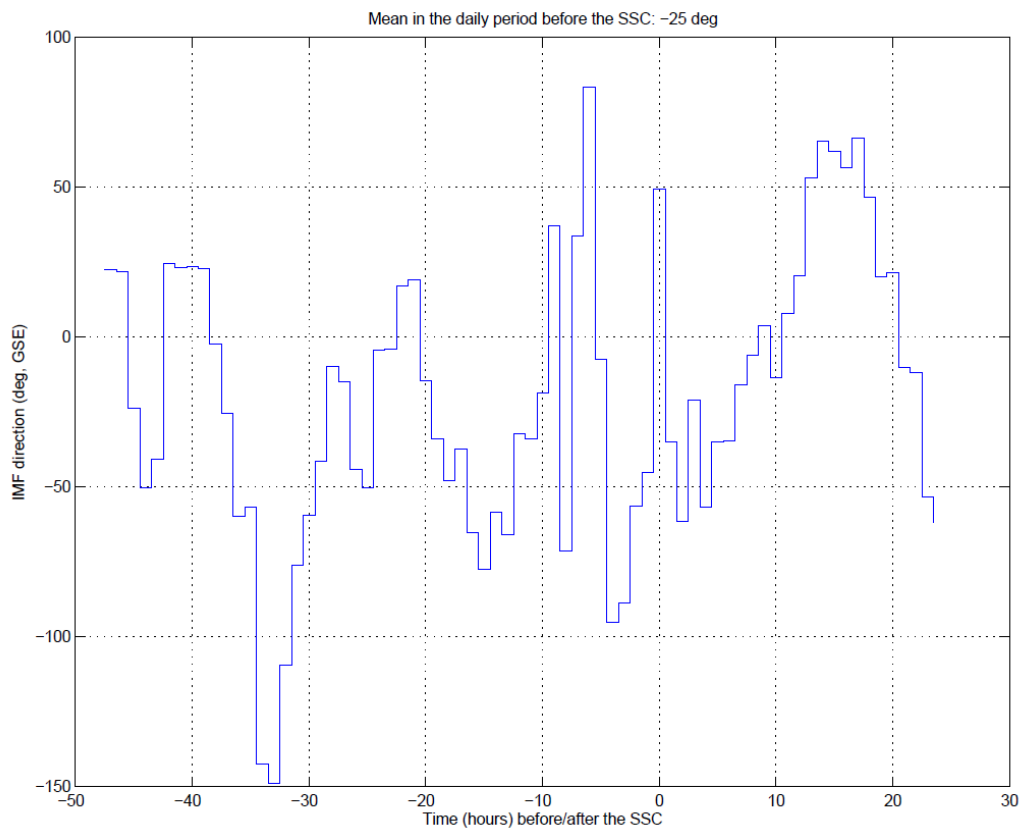
Figure 6.9.   The hourly IMF direction for event #12 observed in September 3rd 2008.
The mean direction in the daily period before the SSC is -25º.
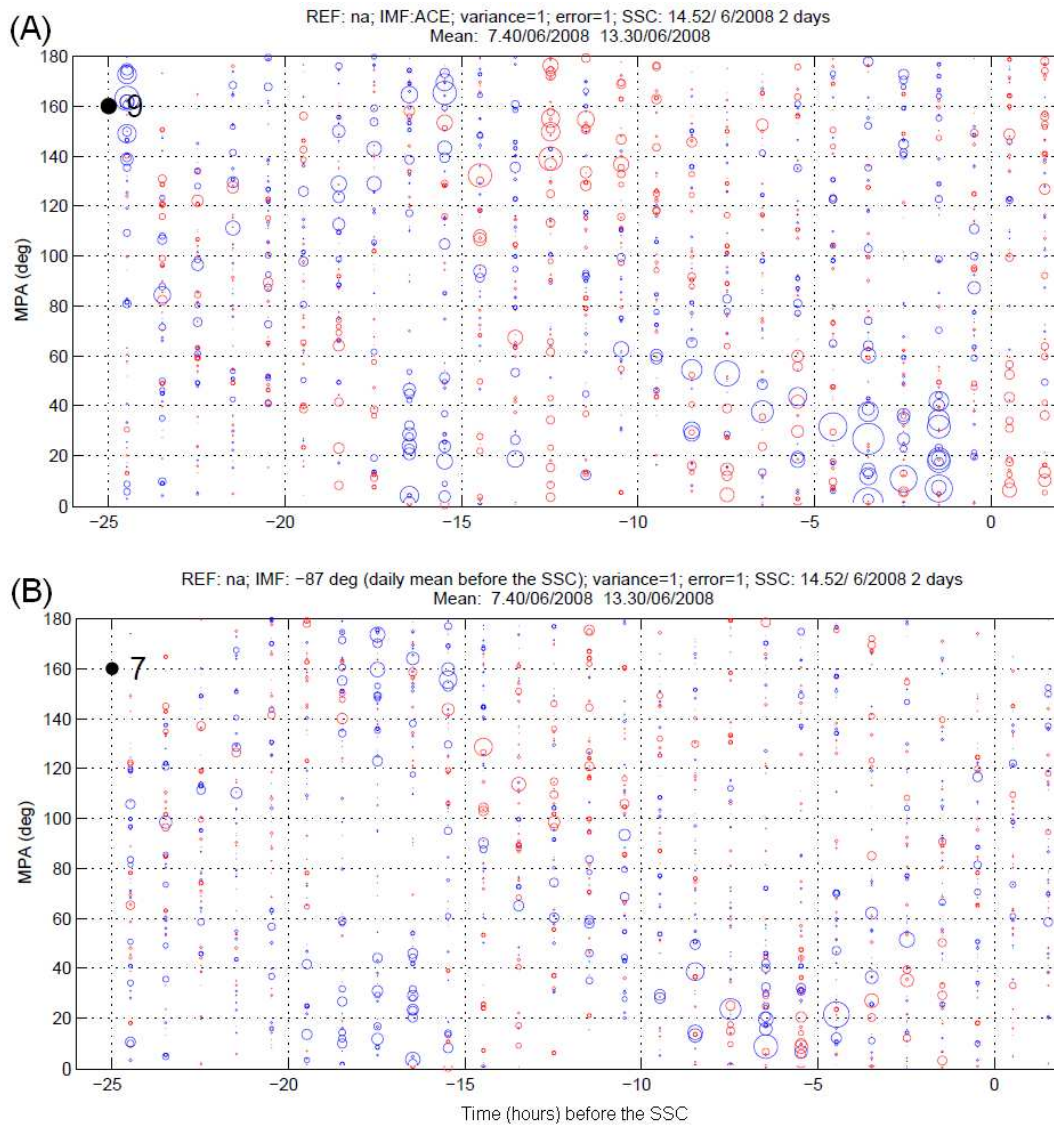
Figure 6.10.   Comparison of the results obtained by the MPA methodology with hourly (A) and daily (B) mean of the IMF direction for event #8 dataset, observed in June 14th 2008. While a systemic increase is clear after 5 hours before the SSC in (A), it is not clear in (B).
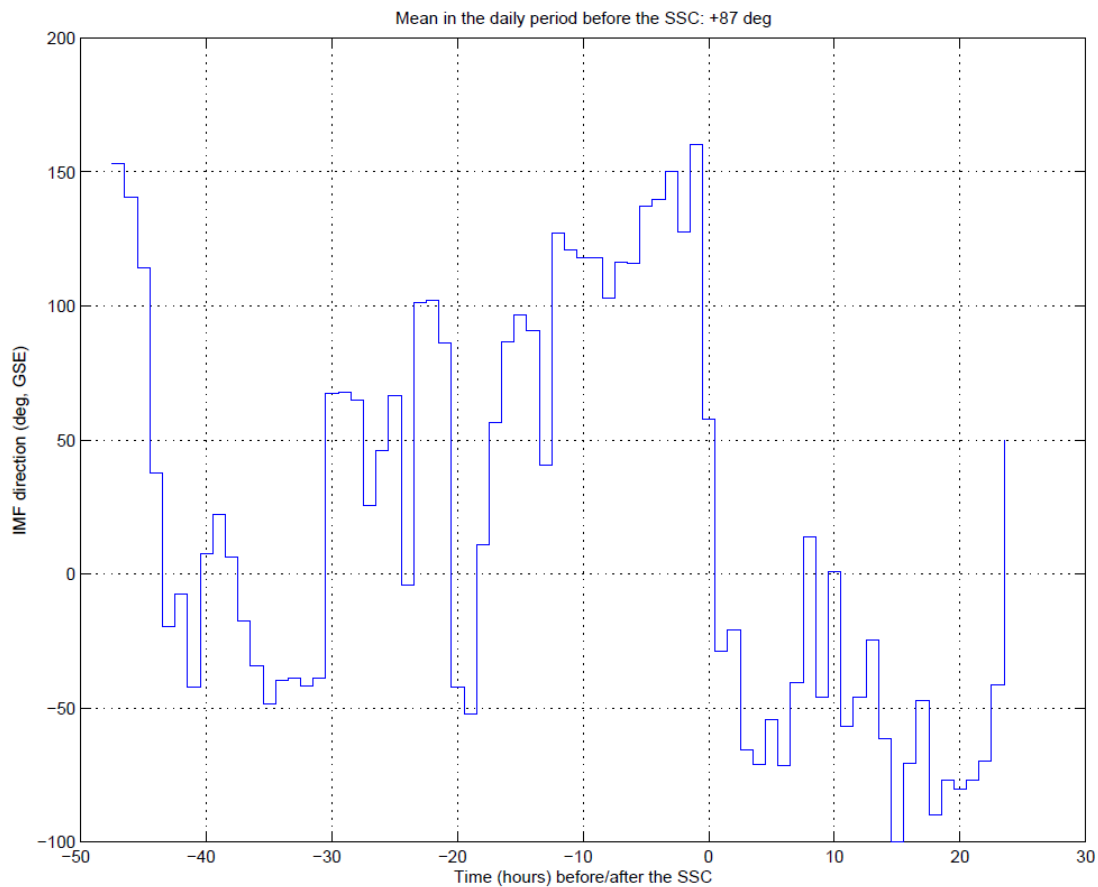
Figure 6.11. The hourly IMF direction for event #8 observed in June 14th 2008. The mean direction in the daily period before the SSC is -25º.

Since 2008 is a period of minimum solar activity, a significant percentage of geomagnetically disturbed periods are expected to be associated with sector crossing of the heliospheric current sheet. Thus, the dates of the 16 SSCs in the Table 6.1 were compared to a list of sector crossing days from the Wilcox Solar Observatory available at http://quake.stanford.edu/~wso/sb/sb.html. The list is derived using the Svalgaard criterion for characterizing a sector crossing: a polarity should be kept the same for at least four days before and after a given moment where polarity change is observed. Mixed or tiny sector are not included in this list because are automatically removed by smoothing. In the GSE coordinate system used in this Thesis work an angle between -90º and 0º

108

is expected for the toward sector and between 90⁰ and 180⁰ for the away sector. The following nine events (52.94%) are coincident with sector crossing: #1, 2, 3, 5, 7, 9, 13, 14 and 15. For events #2, 5 and 15 the crossing change from toward to away (T-A) the Sun. For the remaining, the crossing is away to toward (A-T).

6.1 Case study: the SSC in November 24th 2008

In this Section 6.1 the data analysis of event #16 observed in November 24th 2008 23:51 UT is detailed. The methodology MPA applied here is described in the last sections of Chapter 4. Here, each step is illustrated with plots and compared with the previous one.

The first step is correcting the dataset for both by pressure and temperature, as described previously in Chapter 4. This step is shown in Figure 6.4 where the panels show the deviations of four vertical channels of the GMDN. The crosses indicate pressure corrected data and the asterisks indicate temperature and pressure corrected data. The percentual deviations $\delta C_{i,j}(t)$ for each station i and directional channel j as a function of time t is calculated as follows:

$$\delta C_{i,j}(t) = 100 \cdot \left(\frac{C_{i,j}(t) - \overline{C}_{i,j}}{\overline{C}_{i,j}} \right) \tag{6.1}$$

where $C_{i,j}$ is the hourly count rate and $\overline{C}_{i,j}$ is the mean hourly count rate in the period from November 22nd 2008, 00:00 UT, to November 24th 2008, 00:00 UT (hereafter pre-storm period, which is always indicated in the title of each panel of MPA and VPA in all Figures in this Chapter 6). This pre-storm period is chosen arbitrarily ending one day before the SSC. After the SSC cosmic ray can be modulated in association to the storm and a Forbush decrease can be seen. In the daily period preceding the SSC precursory phenomena like precursory increases or loss cones can possibly be present.

109

Details about the temperature effect are presented in Table 6.2. For the MMD stations of São Martinho da Serra and of Hobart, which are in the south hemisphere and, therefore, are in the summer, the mean altitude of the 100 hPa layer in the period is above the yearly average. Thus, the temperature has a negative effect and the corrected count rate should be higher than the observed. This is shown by the mean of the count rate of corrected data which is bigger than the mean of the not corrected one. The deviation of the corrected data, although, is lower than the not corrected because of the difference in the mean count rate (see Figure 6.12). For the MMD stations of Nagoya and Kuwait, which are in the north hemisphere, the situation is the opposite: the mean altitude of the 100 hPa layer in the period is under the yearly average, the temperature and a positive effect and the corrected count rate is lower than the uncorrected.

Table 6.2. The temperature effect in the vertical channels of the four stations of the GMDN.

Station	Yearly mean altitude of the 100 hPa layer (m)	Pre-storm mean altitude of the 100 hPa layer	Pre-storm mean temperature effect	Pre-storm mean hourly count rate for the vertical direction (pressure corrected)	Pre-storm mean hourly count rate for the vertical direction (temperature and pressure corrected)
Nagoya	16373	-	+	2.9592×10^6	2.9346×10^6
São Martinho da Serra	16418	+	-	2.5692×10^6	2.5867×10^6
Kuwait	16503	-	+	8.6655×10^5	8.6360×10^5
Hobart	16184	+	-	8.3769×10^5	8.4086×10^5
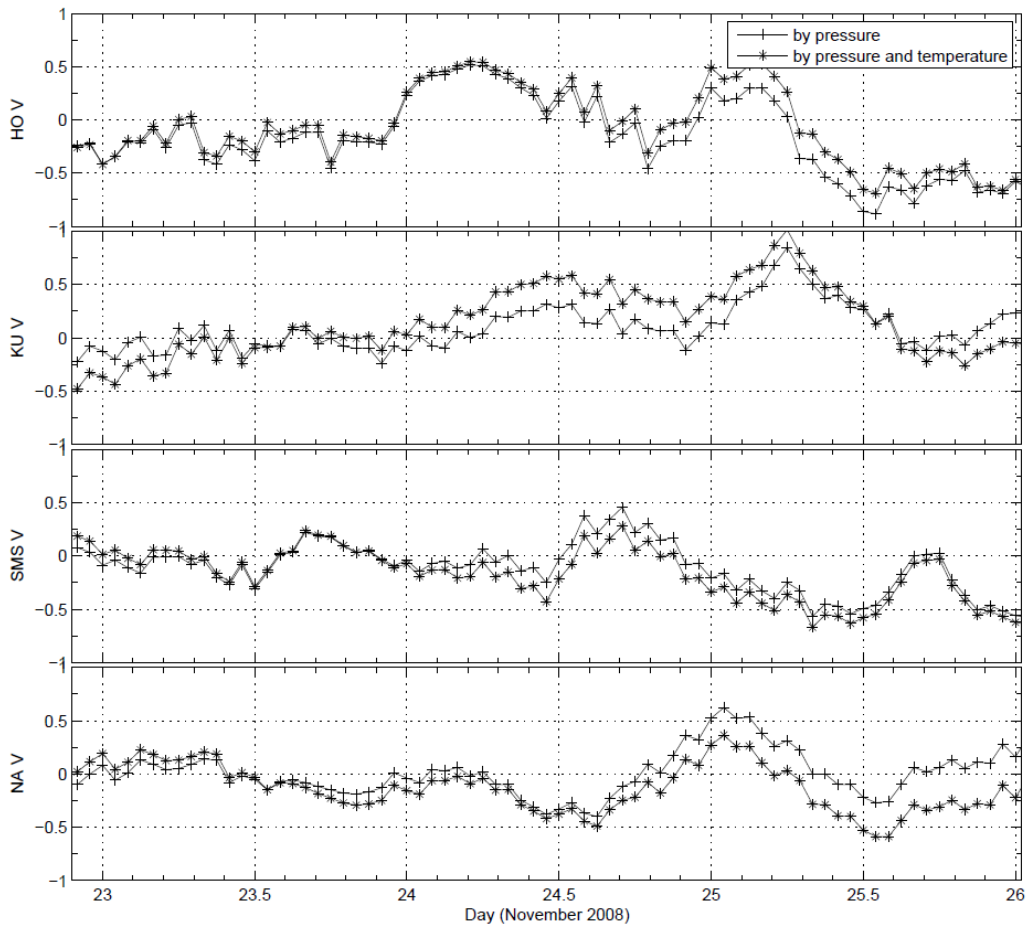
Figure 6.12. The four GMDN vertical channels' deviation corrected only for the pressure effect (crosses) and both for pressure and temperature effect (asterisks).

The next step is calculating the trailing moving average (TMA) on the temperature corrected data. The vertical channel of Nagoya is adopted as the reference. This channel is generally used as a reference in several papers (see Okazaki et al., 2008) because it has the smallest statistical error (0.06%, see Table 4.1).

The TMA of the four vertical channels are shown in Figure 6.13 by the circles and the temperature corrected data is represented by crosses. In the first 24-hour period of the plotted data, the TMA is not calculated because previous

dataset is necessary and the focus in this Thesis workis only the daily period before the SSC. The corrected TMA data (after applying equation 4.5) is shown in Figure 6.14. The data for the vertical channel is not affected by the correction since it is the reference.
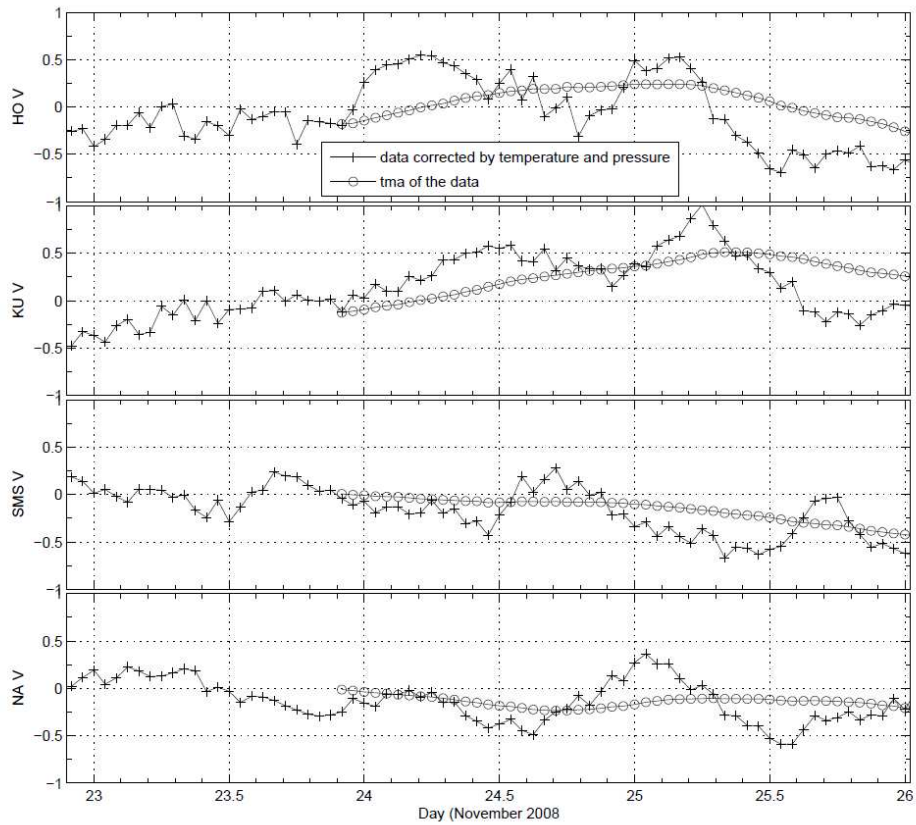
Figure 6.13. The four GMDN vertical channels' deviation previously corrected by temperature and pressure, before the TMA application (crosses). The TMA of the four vertical channels deviations to be applied of the four vertical channels (circles).

.
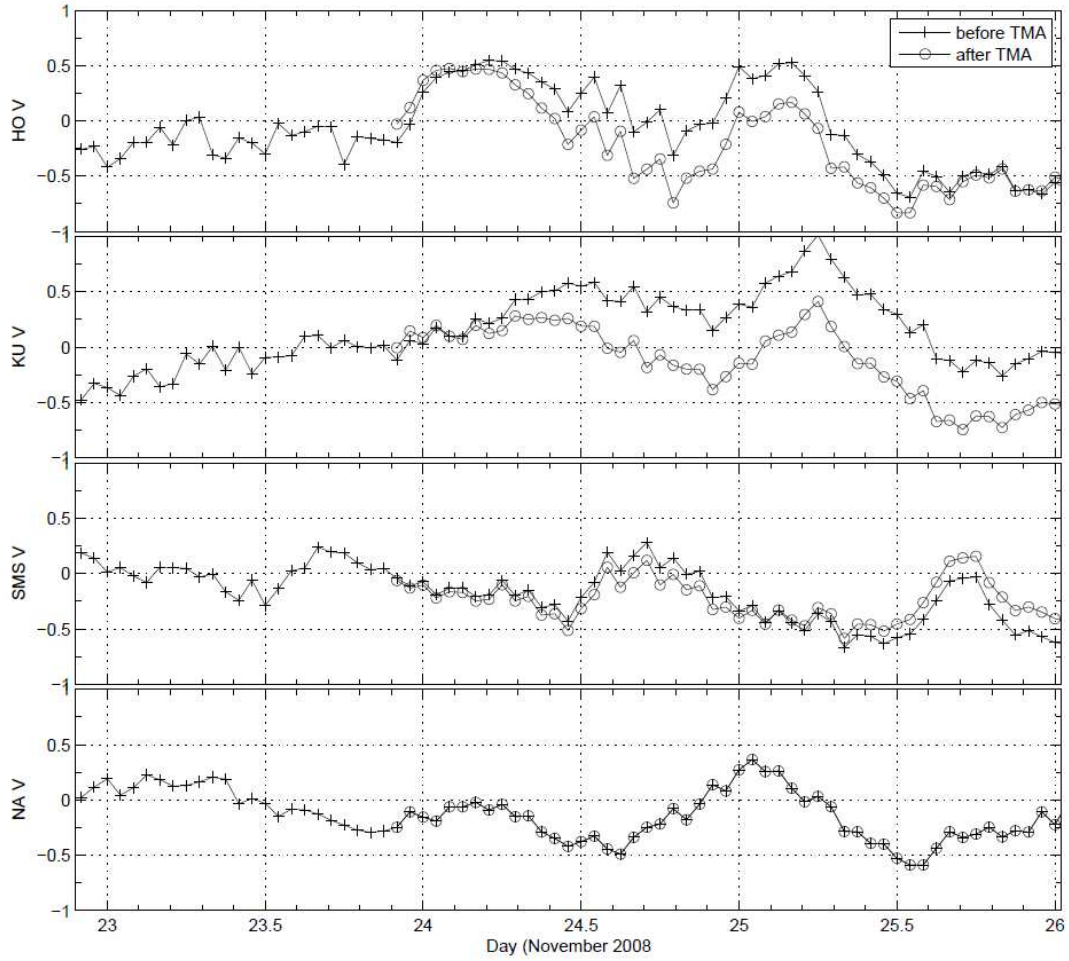
Figure 6.14.   The four GMDN vertical channels' deviations before (crosses) and after (circles) the Normalization by the TMA.

After this, the TMA corrected data $J_{i,j}(t)$ is normalized by the statistical error (σ, see Table 4.1) using the statistical error of the vertical direction of Nagoya $\sigma_{1,1}$ as a reference, according to the Equation 6.2.

$$L_{i,j}(t) = J_{i,j}(t) \cdot \frac{\sigma_{1,1}}{\sigma_{i,j}} \qquad (6.2)$$

By applying Equation 6.2, the directional channels with bigger errors will have their deviation reduced. The data of vertical channel of Nagoya, again, keep the

113

same values. The results for the vertical channels are shown in Figure 6.15. The bigger changes can be seen in Hobart dataset which have the biggest error.
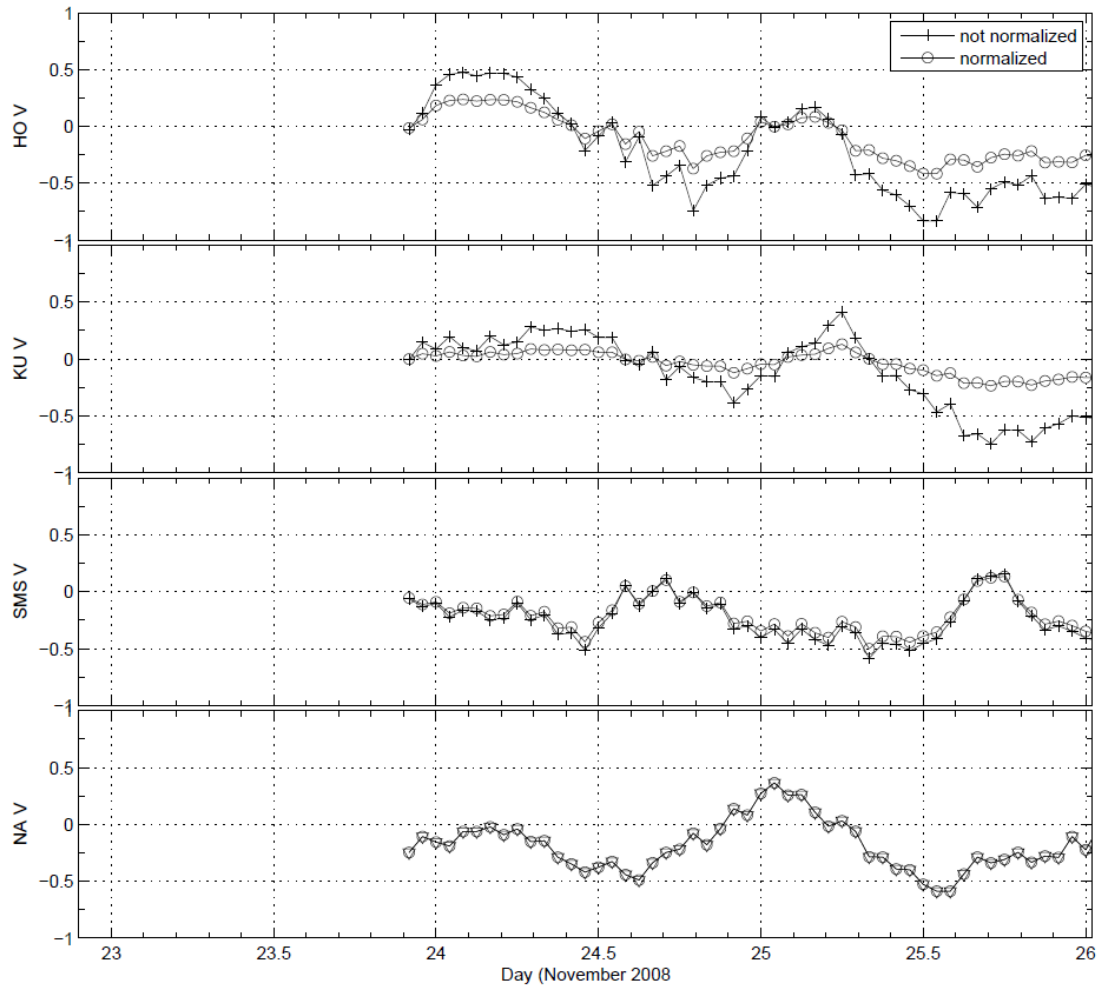
Figure 6.15.   The four GMDN vertical channels' deviations before (crosses) and after (circles) normalization by the statistical error.

Normalization by the variance of each channel is done in a similar way than done for the statistical error, according to:

$$M_{i,j}(t) = L_{i,j}(t) \cdot \frac{\langle L_{1,1} \rangle}{\langle L_{i,j} \rangle} \tag{6.3}$$

where $M_{i,j}(t)$ is data normalized by variance, $\langle L_{1,1} \rangle$ is the variance of the reference channel which is the vertical of Nagoya and $\langle L_{i,j} \rangle$ is the variance of the j-th of the i-th station. All the variances are calculated using dataset from the period plotted in Figure 6.7. The results are shown in Figure 6.16. The variance of the vertical channels of each station is written in the correspondent panel. The station with lower variance for the vertical channel is Kuwait, even Kuwait not being the station with the lowest statistical error. One possible reason for this is the instrumental differences between Kuwait and the other three stations: while Kuwait is a hodoscope made of proportional counter tubes (PCTs), the remaining stations are made of scintillators coupled with photomultipliers.
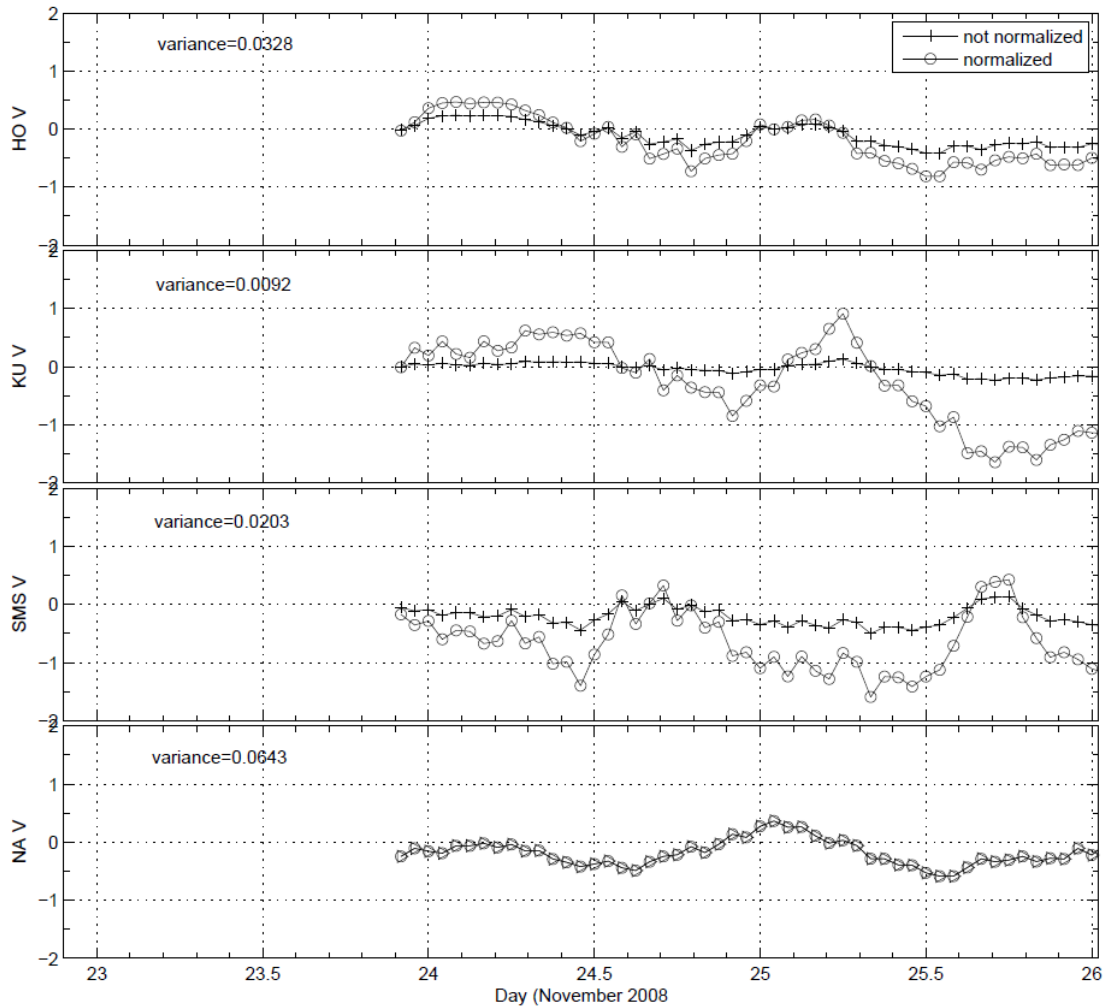
Figure 6.16.   The four GMDN vertical channels' deviations before (crosses) and after (circles) normalization by the variance.

To calculate the pitch angles, the first step is to obtain the interplanetary magnetic field (IMF) direction. The hourly the IMF direction as observed by ACE is shown in the upper panel of Figure 6.17. The remaining panels show the vertical percent deviations after normalization by the variance. The IMF direction is calculated in degrees in the GSE coordinate system. Zero is toward the Sun and 90 degrees is toward the dusk. In the 12-hour before the SSC the mean direction of the IMF is -55 degrees. A vertical channel observes the Sun-Earth line toward the Sun (0 degree direction) at midday and the IMF direction,

in average, in the morning about 10 am local time. This mean direction is quite similar than the direction of the IMF expected by a Parker spiral with solar wind speed of 400 km/s which is -45 degrees.

Fushishita et al., 2010 comment that cosmic ray anisotropy change only gradually if the IMF direction shows a large fluctuation and, in this way, choosing the nominal Parker spiral tends to be better than using the observed IMF for calculating the pitch angle distribution. As in the 12-hour period before the SSC there are not large fluctuations in the IMF direction, choosing the observed hourly IMF for calculating the pitch angle seems to be appropriate.
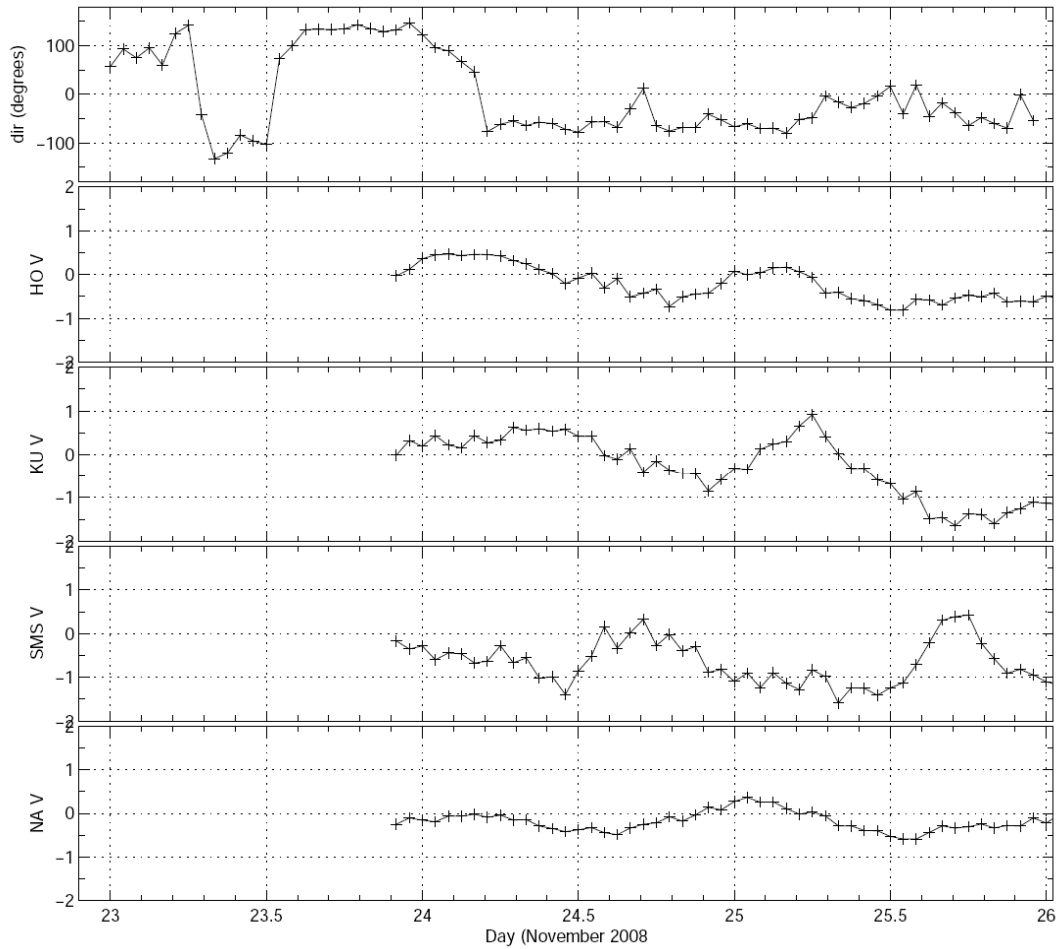
Figure 6.17.   The direction of the magnetic field (in degrees, GSE coordinate system) is shown in the upper panel. The remaining panels show the four GMDN vertical channels' deviation after normalization by the variation.

The next step is calculating the first order anisotropy to the dataset by subtracting the J_i^0 to the data, according to Equation 4.6. J_i^0 represents effects which are common for all directional channels in a given station and include the temperature effect. Dataset before (crosses) and after (circles) the correction is shown in Figure 6.18. J_i^0 and the dataset after its subtraction are compared in Figure 6.19.

118
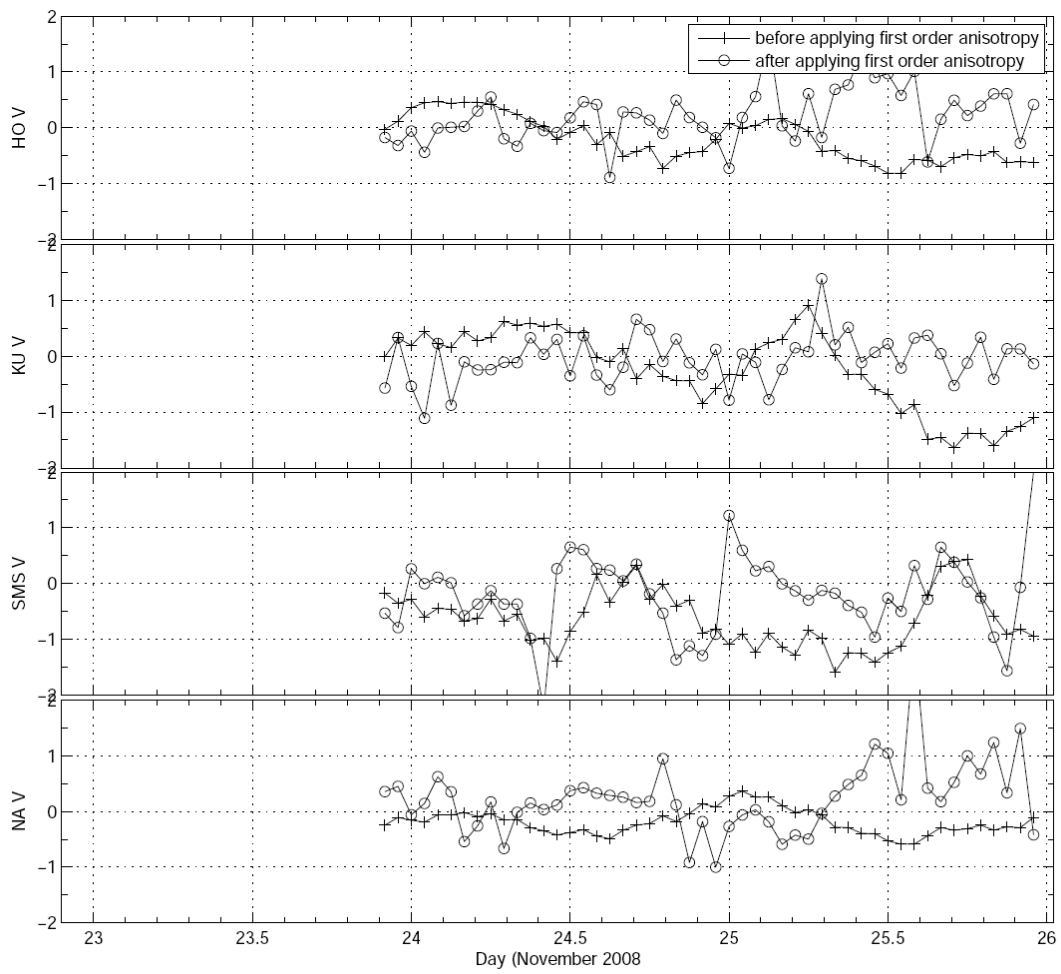
Figure 6.18.   The four GMDN directional channels' deviations before (crosses) and after (circles) calculating the first order anisotropy.

119
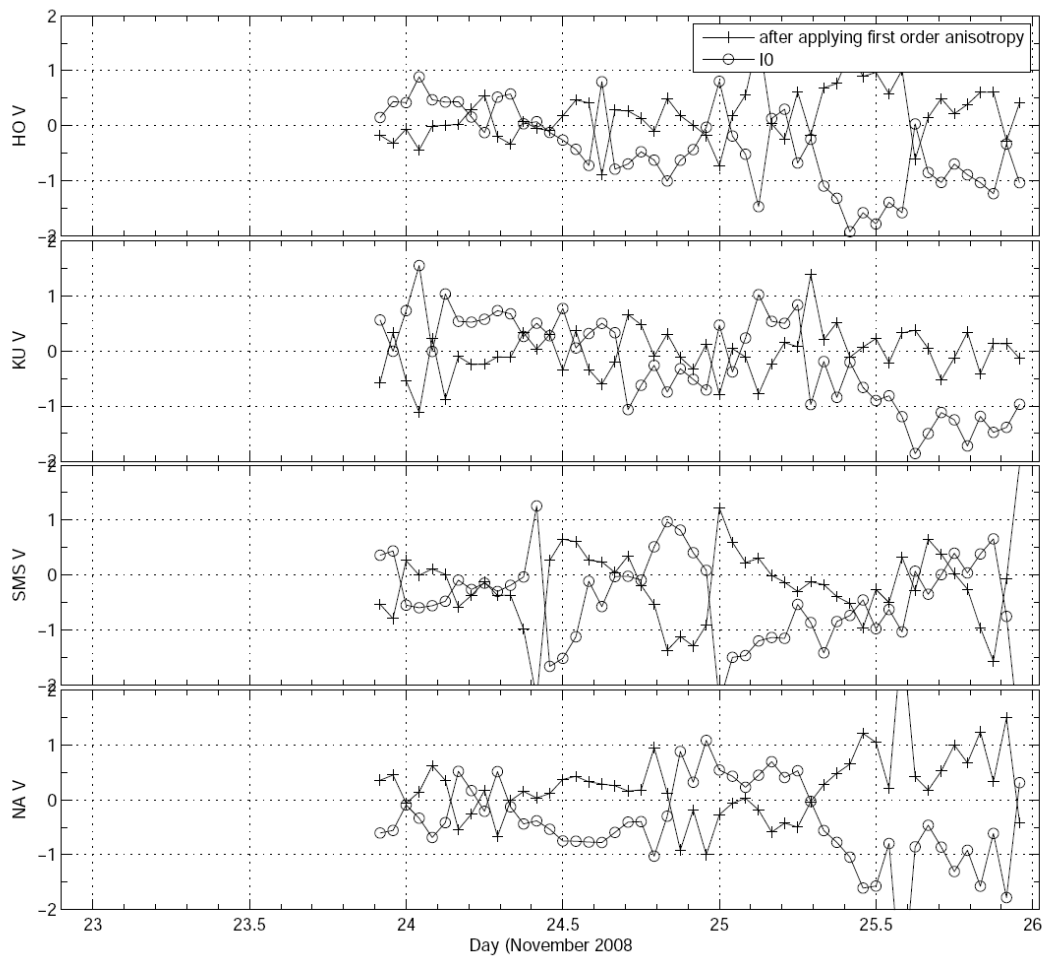
Figure 6.19.   The four GMDN vertical channels' deviations after applying the first order anisotropy (crosses) and the Jo component (referred as Io, represented by the circles) which was subtracted from the observed data.

The mean deviation of all GMDN directional channels in each hour is shown in Figure 6.20. No significant Forbush decrease can be seen in the pos-SSC period. Two major decreases can be seen in day 24 which can possibly be precursory signatures of the storm.
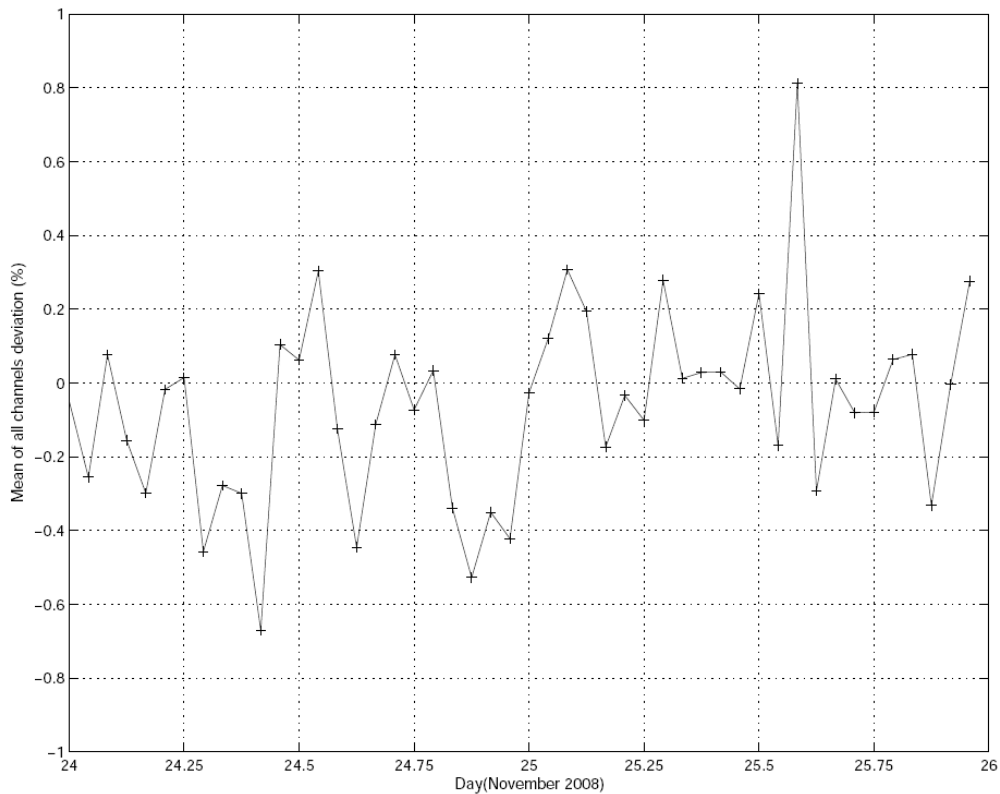
Figure 6.20.   The mean deviation of all directional channels of the GMDN as a function of time (From November 24th to 26th 2008).

Finally, the pitch angles are calculated as explained in section 4.8. The resulting MPA pitch angle distribution is shown in Figure 6.21 with different symbols for different GMDN stations: squares for São Martinho da Serra, diamonds for Kuwait, stars for Hobart and circles for Nagoya. The two systematic decreases are mainly observed by MMD at Sao Martinho da Serra and partially by the MMD at Hobart. The one which is aligned with the IMF direction toward the Sun could be due to reflection of cosmic ray particles, traveling though the IMF lines, when they reach a region with higher IMF intensity. The other, which is in the anti sunward direction, can possible be due to the Compton-Getting effect, due to the convection of the solar wind which tend to increase the observed count rate in the sunward direction and consequently to decrease in the anti sunward direction. The Compton-Getting effect should be proportional to the velocity of

121

the solar wind which is almost constant with speed ~ 400 km/s before the SSC and after increases to about to ~500 km/s. In this Thesis work no correction for the Compton-Getting effect is done.
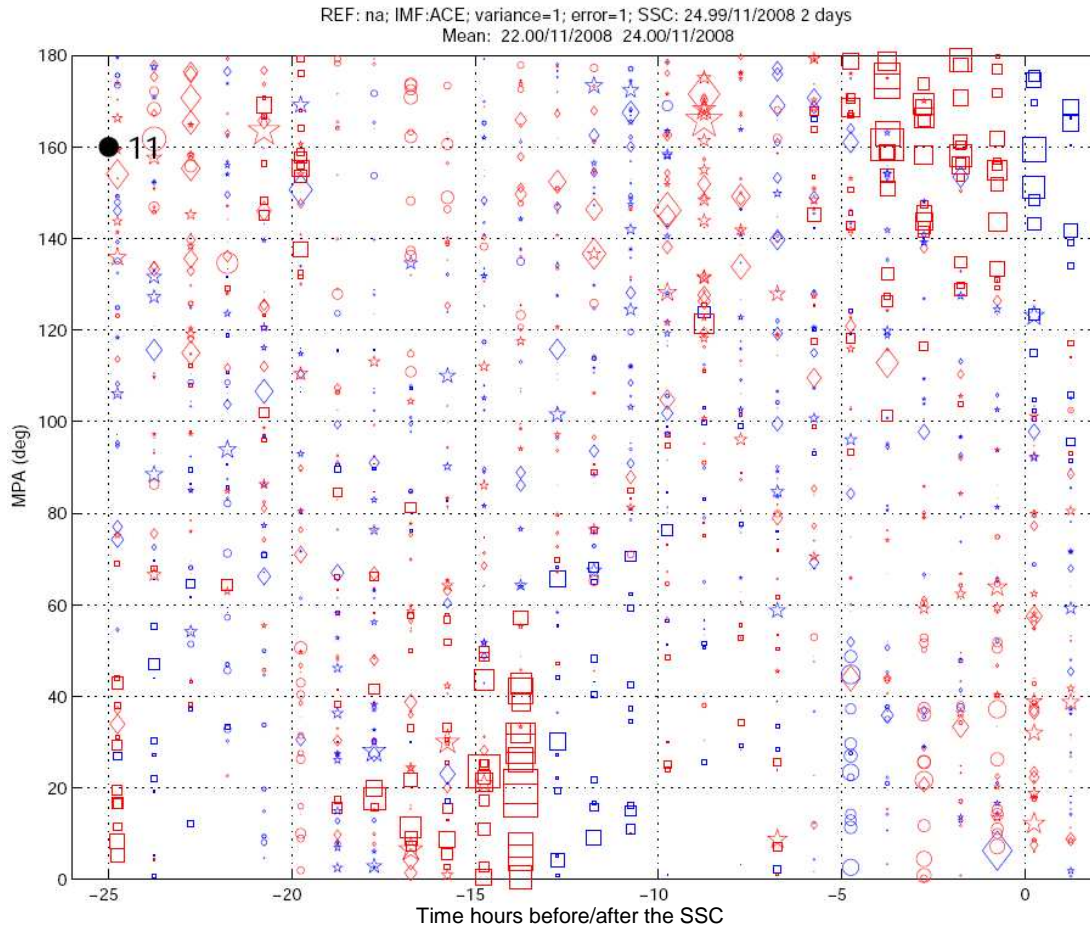
Figure 6.21.   The MPA pitch angle distribution using different symbols for different stations: squares for São Martinho da Serra, diamonds for Kuwait, stars for Hobart and circles for Nagoya.

The distribution of the deviation as a function of the angle is shown in Figure 6.22. If observing the GMDN stations of Nagoya, Kuwait and Hobart, a linear trend can be observed. Despite been possible to identify such trend in the channels of Nagoya, Kuwait and Hobart, the channels of Sao Martinho da Serra clearly do not follow this trend.

122

One concern about dataset from the station of São Martinho da Serra is that some directional channels, from the MMD of Hobart and Kuwait, located in similar pitch angles than some directional channels of São Martinho da Serra, have quite different deviation. This fact lead to the idea that some kind of inter-calibration between datasets from the MMD at Sao Martinho da Serra and the neighboring MMDs, like Hobart and Kuwait, should be done. Some attempts to do these calibrations have been done by Munakata et al. (2000) and Da Silva (2009), but have not been done in the present Thesis work.

Figure 6.22.   The percent deviation of the directional channel of different stations (according to the symbols represented in the legend) as a function of the pitch angle, in a given period of one hour ending 2.28 hours before the SSC.

7 RESULTS FROM CORSET

Chapter 7 summarizes the results obtained after running a set of 57 CMEs in CORSET and comparing with the results from the CDAW CME catalog, as well as from Dal Lago et al. (2004) and Schween et al. (2005), hereafter D2005. In this Chapter 7 radial speed and expansion speed of the CMEs are also compared.

The set of events is exactly the same analyzed by Schween et al. (2005) and which is shown in Table 5.2. It includes all the limb CMEs observed by LASCO C3 between 1997/11/14 and 2001/04/15 where EIT images showed a uniquely associated erupting feature within 30 degrees in longitude to the solar limb and within a reasonable time window of a few hours.

For each event several tests have been made trying to find the most appropriate set of frames to be used for finding the contour and/or parameters explained in Chapter 5.

7.1 Not successful events

From the 57 events, CORSET was able to identify acceptable contours for 49 (86%) of the events. In the 6 remaining events, the contour found was not coherent with the definition of CMEs or was limited to a small fraction of the CME. Careful inspection of these 6 individual events allowed us to identify the reasons as of why the segmentation failed. Namely:

- #5: data gaps and exposure different;

- #12: CME partially hidden by the pylon, very faint;

- #24: superposition of two events which CORSET was not able to separate them;

- #31: same as in event #24;

- #46: same as in event #12;

- #54: impossible to select an appropriate image base because another
  event was identified within the same angular range.

7.2 The radial speed

In this Thesis work a new routine for calculating the radial speed starting from the contours found was included in CORSET. The speed is calculated in a way to have similar results than previous catalogs.

The routine looks for points in the contour for each angle in each frame and calculates the radial speed for each angle. If there is not any point found in a given angle, the radial speed is set as zero for this angle. Finally, the routine finds the maximum radial speed. In this step a valid angular range for finding the maximum needs to be set by the user. This is necessary because in some angles close to the boundary of the CME, some frames do not have any point in the contour and the radial speed cannot be computed properly. Removing some angles close to the boundaries does not change the final result since the maximum radial speed is not expected to be close to the boundaries. The radial speed versus angle plot generally is a smooth curve with maximum close to the central angle of the CME.

The maximum radial speed is found and the radial speed in this angle is compared with previous works. Hereafter it will be mentioned simply as radial speed. In a similar way, in the CDAW and D2005 catalogs, the radial speeds are measured in the direction with the fastest leading edge.

The radial speed estimated for the 57 events by CORSET are presented in Table 7.1. It also shows the deviation of the radial speed derived by $Dev(\%)$ to the mean of the three radial speeds calculated with the three methods $Vrad_{mean}$ (last three column of the table) by Equation 7.1:

$$Dev(\%) = 100 \cdot \frac{Vrad - Vrad_{mean}}{Vrad_{mean}} \ . \tag{7.1}$$

Scatter plots comparing radial speeds of two given techniques are shown in Figures 7.1, 7.2 and 7.3. In the three plots the correlation coefficient is high and the highest is the one comparing CDAW and D2005. By comparing the regression of the three methods, CDAW has bigger radial speeds than D2005 and D2005 has bigger speeds than CORSET. So, in general, speeds found by CORSET are smaller than speeds found by manual catalogs. Probably this happens because some parts of the CMEs do have texture very similar to the background and sometimes these parts are not included in the contour found by CORSET. Generally is easy to identify the core of the CME which is totally included by CORSET with no need for specific parameters. The leading edge and sometimes the void, although, are very weak and it is difficult to decide whether some region is part of the CME or not. In these areas, CORSET tends to select smaller regions that CDAW or D2005.

Table 7.1. Radial speed for each event analyzed by CORSET, compared to D2005 and CDAW.

Event number	D2005	CDAW	CORSET	Mean three methods	D2005	CDAW	CORSET
	Radial speed (km/s)				Percent deviation		
1	980	1042	927	983	0%	6%	-6%
2	719	636	582	646	11%	-2%	-10%
3	1664	1863	1575	1701	-2%	10%	-7%
4	1522	1691	1140	1451	5%	17%	-21%
5	1892	2331	-	2111	-10%	10%	-
6	588	878	818	761	-23%	15%	7%
7	1230	1223	907	1120	10%	9%	-19%
8	1629	1484	1307	1473	11%	1%	-11%
9	854	641	743	746	14%	-14%	0%
10	701	874	757	777	-10%	12%	-3%
11	926	1569	1345	1280	-28%	23%	5%
12	640	560	-	600	7%	-7%	-
13	1045	1049	1361	1152	-9%	-9%	18%
14	1205	1389	1254	1283	-6%	8%	-2%
15	488	490	471	483	1%	1%	-2%
16	1172	1402	1232	1269	-8%	11%	-3%
17	701	841	815	786	-11%	7%	4%

127

(continues)

Table 7.1. Conclusion

Event number	D2005	CDAW	CORSET	Mean three methods	D2005	CDAW	CORSET
	Radial speed (km/s)				Percent deviation		
18	830	793	934	852	-3%	-7%	10%
19	1357	1384	1545	1429	-5%	-3%	8%
20	383	396	475	418	-8%	-5%	14%
21	1739	1188	1445	1457	19%	-18%	-1%
22	951	898	983	944	1%	-5%	4%
23	477	709	542	576	-17%	23%	-6%
24	738	699	-	719	3%	-3%	-
25	677	668	648	664	2%	1%	-2%
26	1280	1187	1065	1177	9%	1%	-10%
27	1008	1110	886	1001	1%	11%	-12%
28	1117	1117	1390	1208	-8%	-8%	15%
29	1356	1594	1356	1435	-6%	11%	-6%
30	1531	1549	1258	1446	6%	7%	-13%
31	1226	1212	-	1219	1%	-1%	-
32	915	935	695	848	8%	10%	-18%
33	520	526	547	531	-2%	-1%	3%
34	647	731	980	786	-18%	-7%	25%
35	455	423	589	489	-7%	-13%	20%
36	949	847	915	904	5%	-6%	1%
37	458	811	541	603	-24%	34%	-10%
38	1350	1198	941	1163	16%	3%	-19%
39	752	613	911	759	-1%	-19%	20%
40	642	585	720	649	-1%	-10%	11%
41	957	896	913	922	4%	-3%	-1%
42	893	883	923	900	-1%	-2%	3%
43	520	516	530	522	0%	-1%	2%
44	609	703	745	686	-11%	3%	9%
45	1330	1336	1199	1288	3%	4%	-7%
46	958	1024	-	991	-3%	3%	-
47	886	785	919	863	3%	-9%	6%
48	688	499	651	613	12%	-19%	6%
49	441	408	645	498	-11%	-18%	29%
50	1066	1198	1970	1411	-24%	-15%	40%
51	763	751	815	776	-2%	-3%	5%
52	771	945	778	831	-7%	14%	-6%
65	770	916	898	861	-11%	6%	4%
54	815	639	-	727	12%	-12%	-
55	1178	1183	880	1080	9%	9%	-19%
56	1900	2505	1950	2118	-10%	18%	-8%
57	1397	1199	1154	1250	12%	-4%	-8%
Mean of the absolute values					8%	9%	9%
Standard Deviation					7%	7%	8%
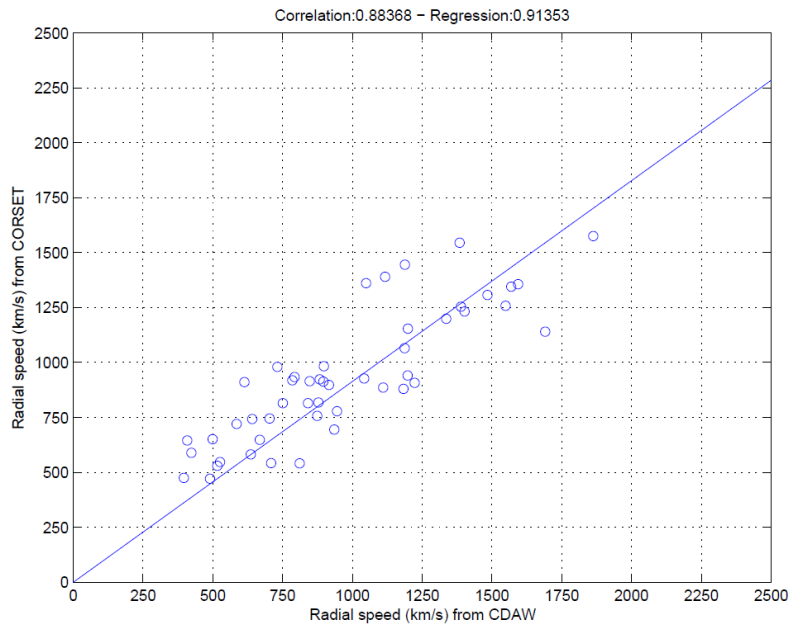
Figure 7.1.   Scatter plot comparing radial speeds from 57 CMEs analyzed both by CORSET and CDAW.
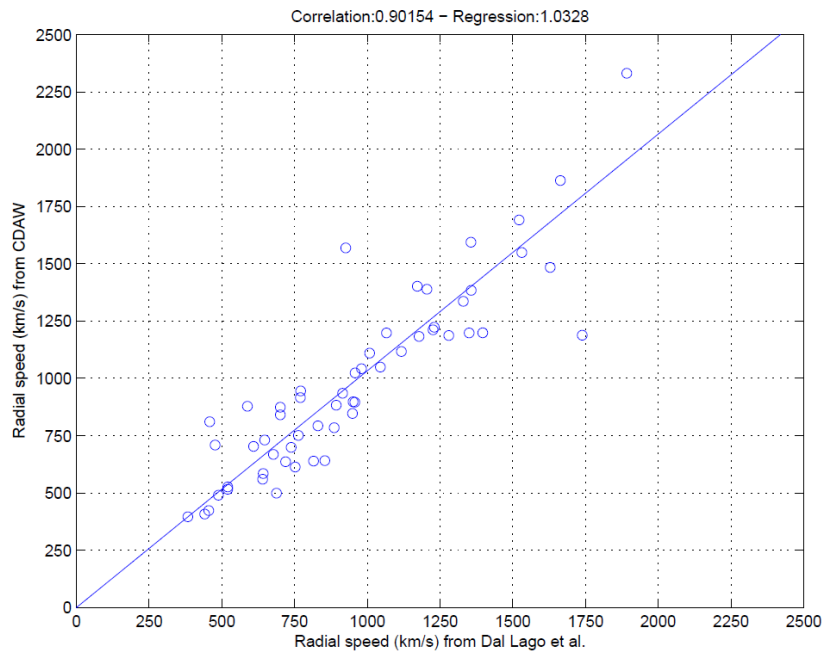
Figure 7.2.   Scatter plot comparing radial speeds from 57 CMEs analyzed both by CDAW and D2005.

129
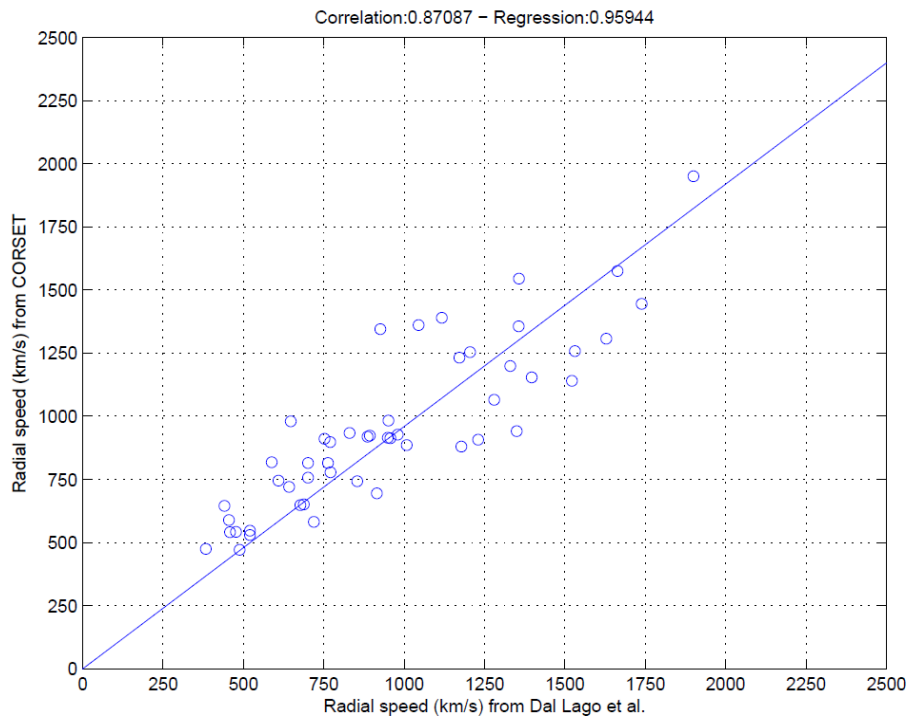
Figure 7.3.   Scatter plot comparing radial speeds of 57 CMEs analyzed both by CORSET and D2005.

7.3 The expansion speed

In this Thesis work a new routine for calculating the expansion speed starting from the contours found was included in CORSET. The speed is calculated in a way to have similar results than D2005, as explained in section 5.9.

The expansion speeds estimated by CORSET are shown in Table 7.2 and compared with previous results from D2005. CDAW does not have any estimate for the expansion speed. In the last column of the Table 7.2 is written 1 (2) for events where the first (second) order fit using the actual point in the contour is closer to the estimate from D2005.

For only 10 (17.5% of 57 CMEs) events the second order fit does have a better result than the first order fit. Generally for the events which the first order fit is better, the second order fit do not have sense at all. For the events for which the second order fit is better, generally the first order fit is still acceptable although worse than the second order fit. For both first and second fit, the expansions speeds found using the actual points in the contour, the smoothed points or the parabolic fit are very similar. From this point on only the first order fit expansion speed with the actual contour of the CME is used in this Thesis work.

A scatter plot of the expansion speed found by D2005 and CORSET is shown in Figure 7.4. The regression coefficient found clearly indicates that in general the expansion speeds found by CORSET are smaller than those found in D2005, in a similar way that was found for the radial speed. The correlation for the expansion speed is lower than the correlations found for the radial speed. The correlation of the radial and expansion speed both from D2005 and both from CORSET are shown in Figure 7.5 and Figure 7.6. By a linear fit on CORSET results we obtain:

$$V_{rad} = 0.96 \times V_{exp} \tag{7.2}$$

while the result with D2005 data is:

$$V_{rad} = 0.88 \times V_{exp} \tag{7.3}$$

Therefore, for limb CMEs the radial speed V_{rad} is almost the same as the expansion speed V_{exp}. It is possible to say that the expansion speed is a fairly reliable proxy for the radial speed since, in other words, the ration between the lateral expansion and radial propagation appears to be constant for most CMEs, confirming the conclusions from Schwenn et al. (2005).

Table 7.2. The expansion speeds found by D2005 and by CORSET

Event number	D2005 (km/s)	first order fit with CORSET data (km/s)	first order fit with CORSET smoothed data (km/s)	first order fit with CORSET data fit by a parabola (km/s)	first order fit with CORSET smoothed data (km/s)	first order fit with CORSET data (km/s)	first order fit with CORSET data fit by a parabola (km/s)	Order with better fit
1	951	596	560	513	1265	1277	1142	2
2	847	406	400	394	617	607	620	2
3	1930	2059	2053	1953	3606	3614	3696	1
4	1672	1450	1010	403	804	-723	-1188	1
5	1607	-	-	-	-	-	-	-
6	781	1042	1039	1168	1111	1089	1517	1
7	1069	1217	1206	1234	1197	1172	1376	2
8	1676	2100	2105	2086	2785	2793	2462	1
9	1032	1003	1009	1029	578	572	623	1
10	878	970	967	996	962	948	977	2
11	1526	1123	1109	1046	1718	1661	1351	2
12	588	-	-	-	-	-	-	-
13	1081	1629	1628	1620	2315	2313	2363	1
14	1427	1087	1069	1171	1288	1223	1549	2
15	325	228	226	235	22	21	10	1
16	957	1063	1056	1062	452	408	416	1
17	541	574	568	580	732	728	759	1
18	1082	1239	1222	1331	-370	-369	-41	1
19	1384	704	683	629	1387	1415	1465	2
20	320	402	400	415	-303	-308	-301	1
21	1927	2301	2277	2647	1195	1097	2512	1
22	553	433	408	398	-24	-16	116	1
23	611	443	440	421	430	425	365	1
24	585	-	-	-	-	-	-	-
25	706	620	619	560	782	766	548	2
26	1381	1448	1450	1492	1262	1263	1377	1
27	889	437	441	448	432	399	387	1
28	1523	938	941	1004	942	975	963	2
29	1925	1946	1927	1930	1518	1517	1717	1
30	1843	1195	1192	1154	808	820	581	1
31	1466	-	-	-	-	-	-	-
32	862	386	387	372	-120	-102	-209	1
33	444	382	381	370	376	392	431	1
34	1107	1309	1301	1278	1929	1915	1178	1
35	679	689	684	719	815	799	793	1
36	1028	927	933	912	1243	1258	1205	1
37	582	457	450	467	464	447	462	2
38	1576	424	470	481	1098	1364	1374	2
39	779	741	737	728	1072	1062	988	1
40	805	849	841	880	797	760	825	2
41	1100	1104	1105	1111	1503	1498	1457	1
42	828	1233	1233	1233	1187	1191	1062	2
43	481	523	522	470	710	712	546	1

132

(continues)

Table 7.2. Conclusion

Event number	D2005 (km/s)	first order fit with CORSET data (km/s)	first order fit with CORSET smoothed data (km/s)	first order fit with CORSET data fit by a parabola (km/s)	first order fit with CORSET smoothed data (km/s)	first order fit with CORSET data (km/s)	first order fit with CORSET data fit by a parabola (km/s)	Order with better fit
44	804	764	771	781	456	429	400	1
45	1404	1444	1438	1248	1955	1934	-639	1
46	1155	-	-	-	-	-	-	-
47	530	373	373	296	-461	-461	-340	1
48	668	705	711	757	832	831	979	1
49	477	409	394	291	-1059	-1165	-1130	1
50	1274	2095	2068	2106	610	595	1095	2
51	1152	959	947	1013	447	386	559	1
52	1270	1009	1002	937	1079	1073	901	2
53	1513	1385	1425	1507	-550	-714	-1338	1
54	560	-	-	-	-	-	-	-
55	1613	411	416	424	104	120	-70	1
56	1867	2012	1997	2014	4503	4389	4649	1
57	1300	1439	1413	1465	787	790	739	1

133
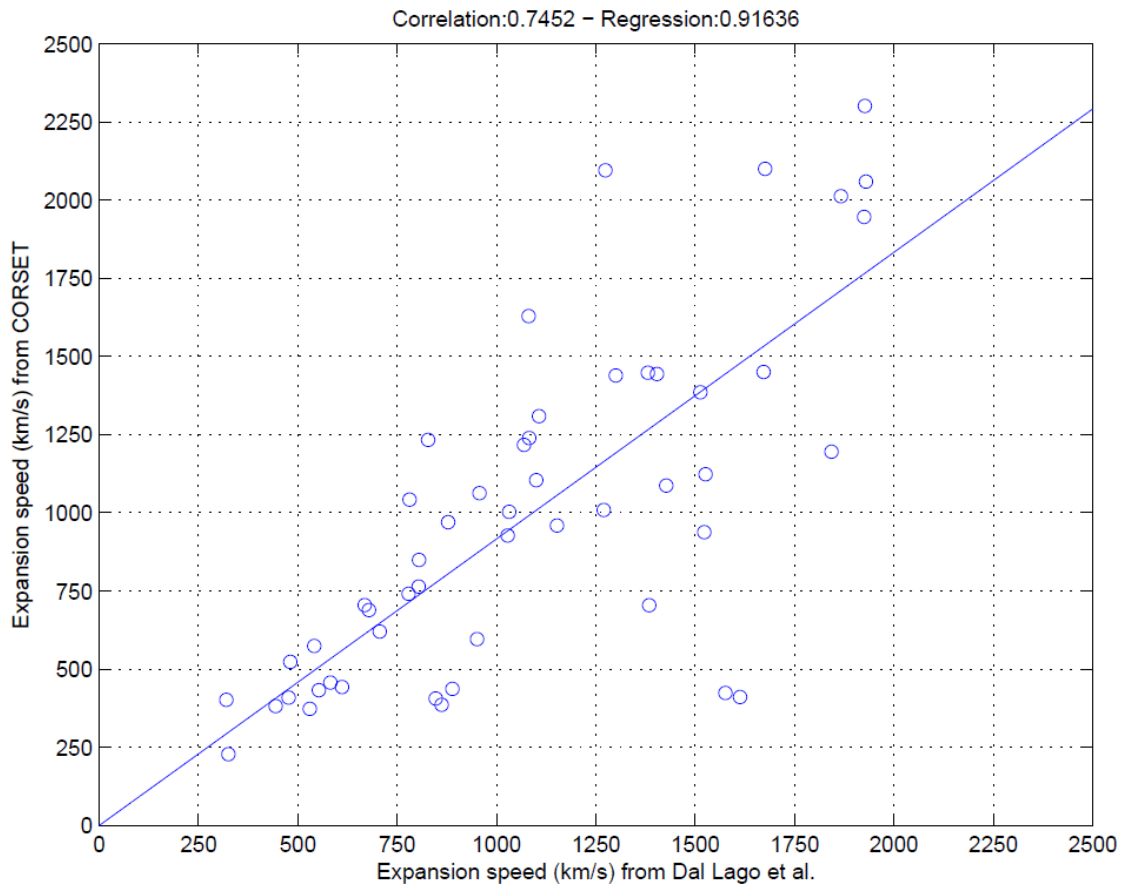
Figure 7.4.   Scatter plot comparing expansion speed from the 57 CMEs analyzed both by D2005 and CORSET
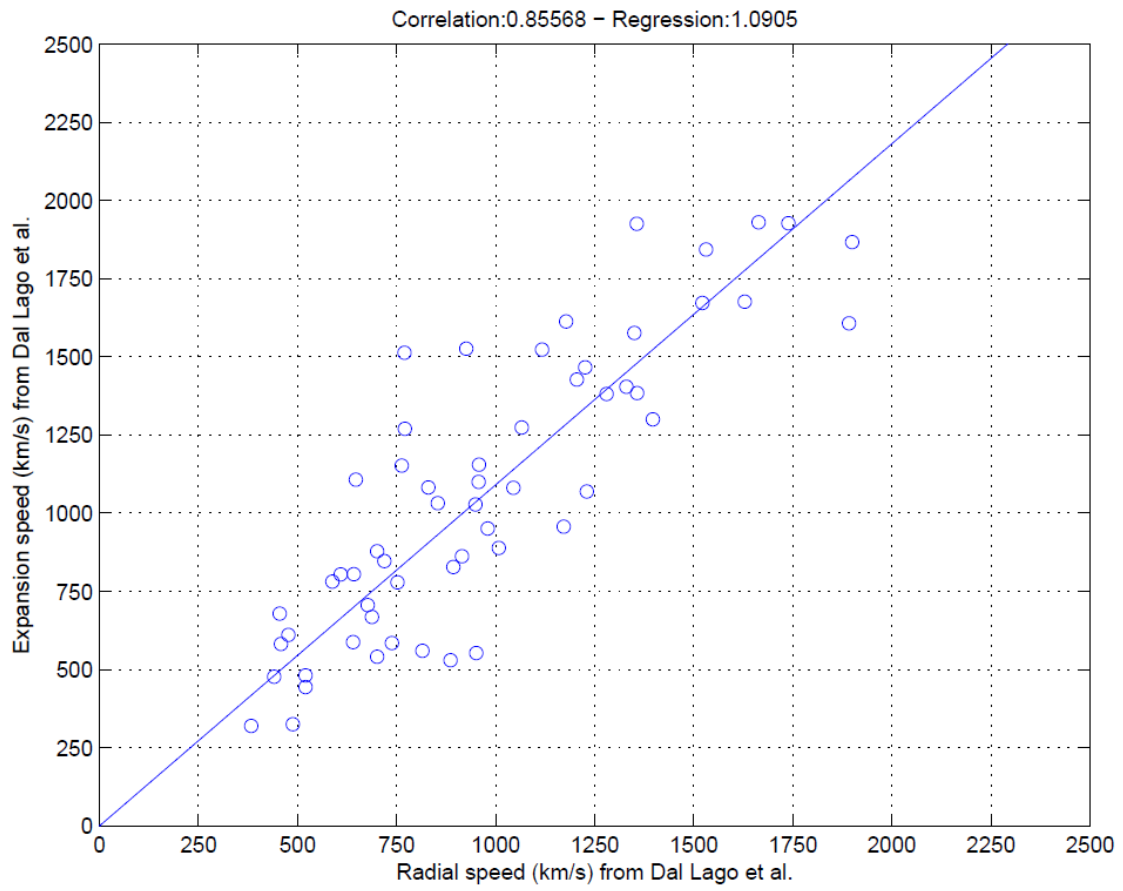
Figure 7.5.   Scatter plot comparing the radial and expansion speeds found by D2005.
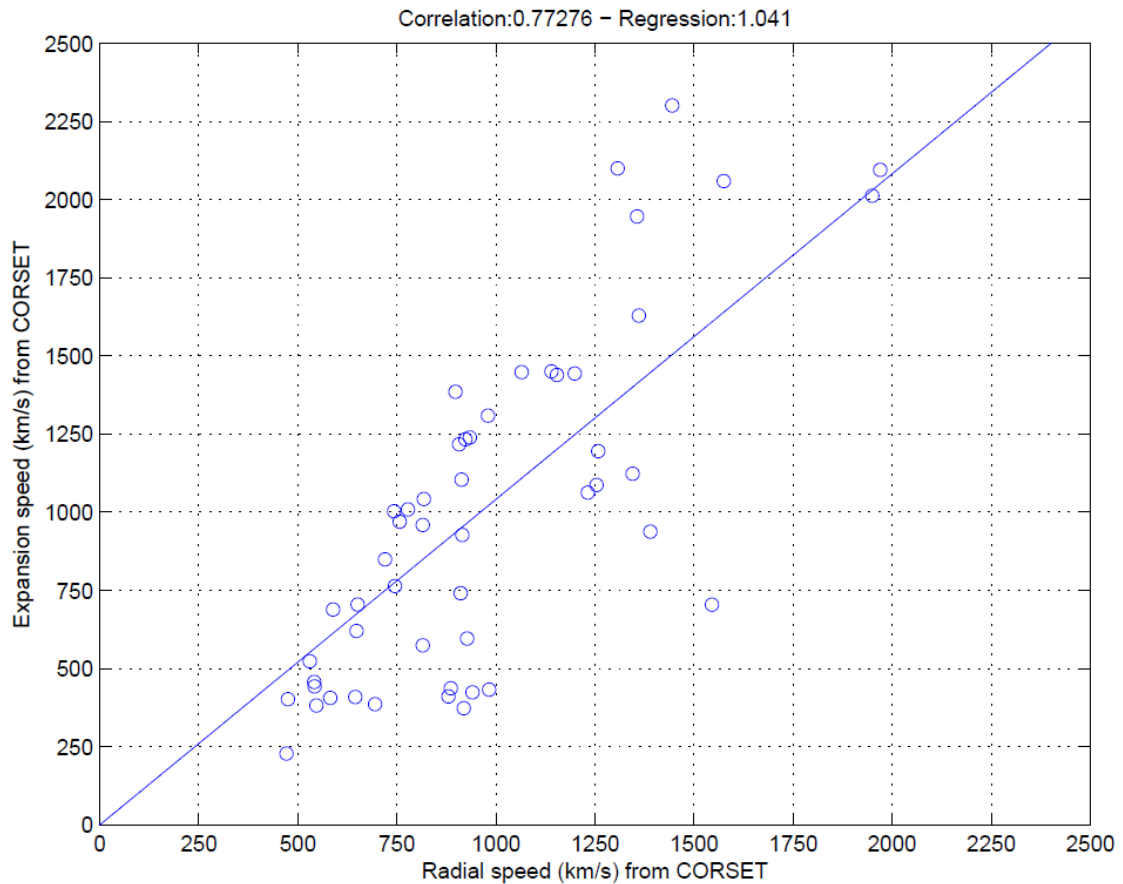
Figure 7.6.   Scatter plot comparing the radial and expansion speeds found by CORSET.

7.4 The main position angle

We define the main position angle (MPA) as the angle of maximum radial speed for a given CME observed in the coronagraph field of view and is computed as explained in section 7.2. This is one of the improvements made on CORSET in the present Thesis work.

A scatter plot comparing CDAW and CORSET main position angle is shown in Figures 7.7. An angle of zero means the north of the Sun and the angles increase counterclockwise.

The results from the two methods are similar. There are not CMEs with MPA in the range close to 0⁰ and 360⁰, since these ranges correspond to the poles of the Sun. For CORSET there is a lack of coverage for angles from ~120⁰ up to the pole of the Sun, due to the pylon of LASCO-C3, which cover the CMEs partially and does not allow a proper contour selection by CORSET. Three CME were identified in the MPA by CDAW.

Table 7.3. The main position angle results of the 57 CMEs analyzed by CORSET. Results are compared to previous from CDAW and D2005

Event	CDAW MPA (degrees)	CORSET MPA (degrees)	Event	CDAW MPA (degrees)	CORSET MPA (degrees)
1	67	69	30	70	54
2	98	72	31	239	-
3	278	244	32	89	83
4	115	93	33	96	95
5	275	-	34	121	37
6	306	267	35	244	254
7	97	72	36	293	276
8	278	273	37	350	357
9	268	305	38	294	281
10	276	300	39	90	111
11	38	30	40	44	59
12	144	-	41	295	289
13	272	326	42	290	298
14	284	295	43	229	254
15	233	234	44	124	110
16	299	317	45	270	266
17	229	222	46	130	-
18	124	131	47	122	121
19	96	97	48	288	311
20	342	304	49	131	127
21	264	255	50	144	115
22	220	225	51	304	301
23	265	246	52	356	331
24	211	-	65	254	319
25	181	172	54	81	0
26	281	253	55	335	291
27	301	301	56	293	278
28	258	190	57	268	272
29	265	190			
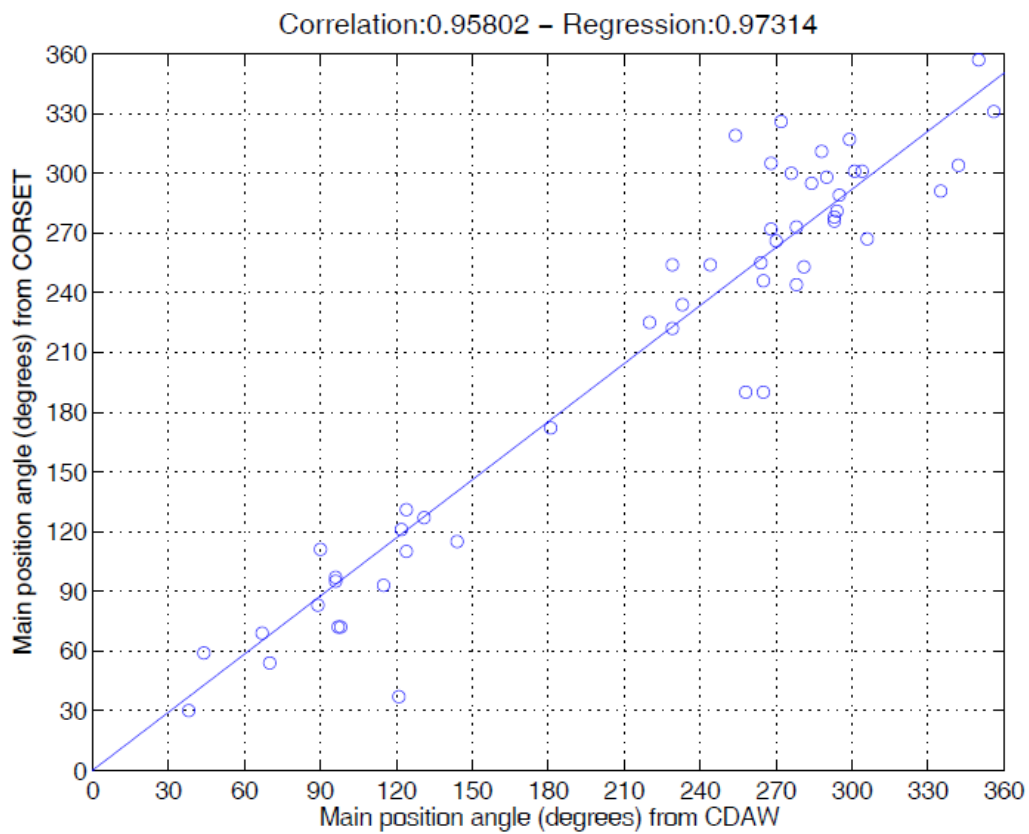
Figure 7.7.   Scatter plot comparing the main position angle of 57 CMEs analyzed both CORSET and CDAW.

8 SUMMARY AND CONCLUSIONS

In this Thesis work two different ways to study disturbances in the interplanetary medium are used: (i) indirect information about the interplanetary medium by the observation of the modulation of high energy cosmic ray particles and, (ii) observations of the Solar corona which can identify transient phenomena like coronal mass ejections.

Observing a global distribution of cosmic ray modulation seems to be able to identify disturbances in the interplanetary medium related to weak and moderate geomagnetic activity. The geomagnetic activity in the period, from February 12th 2008 to December 31st 2008, is weak and moderate and is basically associated in 9 of 16 geomagnetic storms with sector crossing of the heliospheric current sheet.

Many corrections are needed in the observed cosmic ray count rates before a proper positive analysis of the pitch angle distribution can be made. If any of the corrections mentioned in this Thesis work are removed, the visualization of signatures is not possible for many of the studied events. The modulation regarded to interplanetary disturbances for the events studied in 2008 is generally lower than 1%, therefore, a lot of care is needed while working with the data processing, reduction and analysis. One challenge is that different directional channels and different stations have different observation areas and, thus, different statistical errors. In this way, on December 2010, the multidirectional muon detector, MMD, installed in Hobart, Australia, was upgraded, and the observation area changed from 9 m^2 to 16 m^2, reducing the statistical error which was the biggest in the GMDN. One interesting possibility which has been studied recently is the installation of new detectors in the next years. These detectors could fill small gaps in the world surface coverage and create areas of superposition of two MMD' coverage area, which could help the (inter and intra) calibrations among different MMDs.

139

One important step when working with the GMDN is the temperature correction, which is shown to have an up to 2% correction in a yearly perspective. In a daily perspective, it is possible to have an appropriate estimate of the magnitude of the effect, since only two measurements are available per day, in the altitude of the 100hPa equi-pressure layer, where secondary cosmic ray particles are mainly produced. For better temperature corrections in a daily perspective, the first order anisotropy was applied. One missing step in this Thesis work, already done in previous works, is the Compton-Getting effect correction which is due to the solar wind convection and due to the Earth's rotation.

After performing all the data reduction and corrections, some signatures can be clearly identified for 14 of the 16 events analyzed when applying the MPA pitch angle distribution methodology. These signatures last for at least two hours, in a certain group of directional channels for one or more stations, which are confined in a pitch angle range of ~ 50^0. Some signatures are of the type "loss cone" where a decrease is found in the sunward directions. This signature is regarded to the suppression of particles located downstream of an interplanetary disturbance which leaks to the upstream region. Other signatures are of the precursory increases type, which are possibly due to a head-on collision of upstream particles with an approaching interplanetary shock.

Two (12.5%) of the 16 events studied do not show any clear signature. There is no direct relation between the magnitude of the IMF and the presence or not of signatures.

In this Thesis work the results of the MPA methodology application on the data reduction are compared, when using the hourly and daily mean of the ACE *in situ* IMF direction, for calculating the pitch angle directions. Generally, results with the daily mean are very similar to the results with the hourly and daily mean and so, the signatures seen in MPA with both mean periods, which is the case of 10 events among 16 analyzed. For the 6 remaining events, although, the

results are different between the hourly and daily mean of the IMF. In this case, the hourly mean is better for 4 of the 6 events.

The data application of VPA methodology, although, do not show any signature in all the 16 events, from 2008, analyzed in this Thesis work. Preliminary results without temperature correction, TMA, and first order anisotropy, have shown good perspectives for observing signatures with the VPA methodology, but these signatures disappeared after applying some of the discussed corrections. The VPA methodology is expected to be a way to subtract the temperature effect if temperature does not change substantially in two consecutive hours. More attempts to use the VPA methodology on the data analysis could possibly lead to better results.

On the other hand, this Thesis work also gives special attention to the analysis of the coronal mass ejections (CMEs). CMEs have widely been observed for more than thirty years and many features like speed, acceleration, mass and kinetic energy, have been widely studied and estimates have been done. Even though, many features like speed are not consensus and are subject to judgment of an observer. The CORonal Segmentation Technique (CORSET) is a supervised methodology (not fully automatic as the Computer Aided CME Tracking - CACTUS - is) which attempts to solve discrepancies in the estimated speeds of CMEs.

In this Thesis several routines to compute kinematical properties of CMEs (like radial speed, expansion speed, position angle etc) have been developed and included in CORSET. We tested it in a set of 57 limbs events and found that CORSET is able to identify correctly in 86% of the cases the contours of CMEs. An appropriate set of frames where the CME is present needs to be selected by an observer. CORSET is a step forward when looking for agreement of estimative of radial and expansion speeds of CMEs. Once the frames to be used are selected and some parameters are specified, the results do not depend on the observer judgment, as is the case of manual catalogs.

CORSET was run for a set of 57 limb CMEs and was able to properly identify the contour layout of 86% in these contours, which are in agreement with the definition of CME. The CORSET results have a high correlation with previous catalogs like CDAW (the SOHO/LASCO CME Catalog is also known as CDAW catalog) and D2005. In a general term, the estimations for the radial speed are smaller than previous catalogs: about 0.91 times the radial speed of CDAW, and about 0.95 times the ones of D2005. For the expansion speed, the estimations from CORSET are 0.92 times the ones from D2005. Therefore, one can conclude that CORSET estimations are slightly smaller than in other catalogs.

The results from CORSET confirmed previous results from Schwenn et al. (2005), which show that the expansion speed can be used as a proxy for the radial speed. These results lead to the possibility of using the expansion speed of any CME (even for not limb CMEs) as a way to estimate the radial speed, which cannot be measured directly when a CME is a not a limb, since the CME is out of the plane of the sky, and LASCO shows only the projection of the CME in the plane. Once the radial speed is estimated, the CME travel time from the Sun to the Earth can be better estimated.

The CORSET methodology still needs to be tested with halo CMEs, which are very faint and, thus, more difficult to be identified. Anyway, as CORSET can properly work with a set of 57 events, it is believed that CORSET can be applied to all CMEs observed by LASCO in a way to produce a catalog with a good success rate.

The known limitations of the CORSET methodology are: a) tracking a CME when it is under the pylon; b) tracking a CME when the data has gaps; c) tracking two consecutive CMEs, because in this case it is difficult to define a background for the second event. These 3 limitations can explain the 6 events where CORSET was not successful on finding a contour coherent with the definition of CME.

One suggestion for future work is using the contour of the CME and search whether a CME is symmetric or not, trying to find a relation between the profiles of the leading edge of the CME with the solar wind speed distribution in the same region.

REFERENCES

ANDREWS, M. D. A search for CME associated with big flares. **Solar Physics**, v. 218, p. 261-279, 2003.

ASCHWANDER, M. J. **Physics of the solar corona** – an introduction. Springer, 2004. 842p. ISBN: 3-540-22321-5.

BERNHOHR. **Cosmic-ray air showers**. Max-Planck-Institut für Kernphysik. Available at: http://www.mpi-hd.mpg.de/hfm/CosmicRay/Showers.html, accessed on January 12th 2010.

BLACKETT, P. M. S. On the Instability of the Barytron and the Temperature Effect of Cosmic Rays. **Physical Review Letters,** v. 54, p. 973-974, 1938

BOTHE, W.; KOLHORSTER, W. Das Wesen der Hohenstrahlung. **Zeitschrift fur Physik**, v. 56, n. 11-12, p. 751-777, 1929.

BRUECKNER, G. E.; HOWARD, R. A.; KOOMEN, M. J.; KORENDYKE, C. M.; MICHELS, D. J.;MOSES, J. D.; SOCKER, D. G.; DERE, K. P.; LAMY, P. L.; LLEBARIA, A.; BOUT, M. V.;SIMNETT, G. M.; BEDFORD, D. K.; EYLES, C. J. The large angle spectroscopic coronograph (LASCO). **Solar Physics**, v.162, n. 1-2, p. 357-402, 1995.

CANE, H. V.; RICHARDSON, I. G.; ST. CYR, O. C. Coronal mass ejections, interplanetary ejecta and geomagnetic storms. **Geophysical Research Letters,** v. 27, n. 21, p. 3591-3594, 2000.

CARGILL, P.; HARRA, L. K. Coronal Mass Ejections. In: In: KAMILDE, Y. CHIAN, A. **Handbook of the Solar-Terrestrial Environment**. Springer, 2007. 539 p. ISBN: 978-3-540-46314-6.

CHIAN, A. C. L. & KAMILDE, Y. An Overview of the Solar-Terrestrial Environment. In: KAMILDE, Y. CHIAN, A.(eds.). **Handbook of the Solar-Terrestrial Environment**. Springer, 2007. 539 p. ISBN: 978-3-540-46314-6

CLAY, J.; BERLAGE, H. P. Variation der Ultrastrahlung mit der geographischen Breite und dem Erdmagnetismus. **Die Naturwissenschaften**, v. 20, n. 37, p. 687-688, 1932.

CREMADES, M. H. **Three-Dimensional Configuration and Evolution of Coronal Mass Ejections**. Ph.D. Dissertation. Fakultät für Physik und Geowissenschaften der Technischen Universität Carolo-Wilhelmina, Braunschweig, Germany, 2005.

DA SILVA, M. R. **Detecção ao de distúrbios solar-interplanetários combinando observações de satélite e de raios cósmicos de superfície para aplicação em clima espacial.** Ph. D. dissertation in Space Geophysics – National Institute for Space Research, São José dos Campos, Brazil, 2009.

DAL LAGO, A.; SCHWENN, R.; GONZALEZ, W. D. Relation between the radial speed and the expansion speed of coronal mass ejections. **Advances in Space Research**, v. 32, n. 12, p. 2637-2640, 2004.

DOMINGO, V.; FLECK, B.; POLAND, A. I. The SOHO Mission: An Overview. **Solar Physics**, v. 162, p. 1-37, 1995.

DULDIG, M. Muon observations. **Space Science Review**, v. 93, p. 207-226, 2000.

DULK, G. A.; MCLEAN, D. Coronal magnetic fields. **Journal of Solar Physics**, 57, p. 279-295, 1978.

DUNGEY, J. W. Interplanetary magnetic field and the auroral zones. **Physical Review Letters**, v. 6, p. 47-48, 1961.

DUPERIER, A. A New Cosmic-Ray Recorder and the Air Absorption and Decay of Particles. **Terrestrial and Magnetic Atmospheric Electricity**, v. 49, 1–7 p., 1944.

DUPERIER, A. The Meson Intensity at the Surface of the Earth and the Temperature at the Production Level, **Proceeding of the Physical Society,** v. 62, p. 684–696, 1949.

ECHER, E.; GONZALEZ, W. D.; ALVEZ, M. V. Minimum variance analysis of interplanetary coronal mass ejections around solar cycle 23 maximun (1998-2002). **Solar Physics,** v. 233, p. 249-263, 2006.

FUSHISHITA, A.; KUWABARA, T.;KATO, C.; YASUE, S.; BIEBER, J. W.; EVENSON, P.; DA SILVA, M. R.; DAL LAGO, A.; SCHUCH, N. J.; TOKUMARU, M.; DULDIG, M.L.; HUMBLE, J.E.; SABBAH, I.; AL JASSAR, H. K.; SHARMA, M.M.; MUNAKATA, K. Precursors of the Forbush Decrease on 2006 December 14 observed with the Global Muon Detector Network (GMDN). **The Astrophysical Journal,** v. 715, p. 1239-1247, 2010.

GARY G. A.; MOORE, R. L. Eruption of a multiple-turn helical magnetic flux tube in a large flare: evidence for external and internal reconnection that fits the breakout model of solar magnetic eruptions. **The Astrophysical Journal**, v. 611, p. 545-556, 2004.

GONZALEZ, W. D.; JOSELYN, J. A.; KAMIDE, Y.; KROEHL, H. W.; ROSTOKER, G.; TSURUTANI, B. T.; VASYLIUNAS, V. M. What is a magnetic storm? **Journal of Geophysical Research**, v.99, n. A4, p. 5771-5792, 1994.

GOSLING, J. T. Coronal mass ejections: the link between solar and geomagnetic activity. **Physics of Fluids**, v. B5, n. 7, p. 2638-2645, 1993.

GOSLING, J. T.; BAME, S. J.; MCCOMAS, D. J.; PHILLIPS, J. L. Coronal mass ejections and large geomagnetic storms, **Geophysical Research Letters**, v. 17, p. 901-904, 1990.

GOSLING, J. T.; HILDNER, E.; MACQUEEN, R. M.; MUNRO, R. H.; POLAND, A. I.; ROSS, C. L. Direct observations of a flare related coronal and solar-wind disturbance. **Solar Physics**, v.40, n.2, p. 439-448, 1975.

GOUSSIES, N.; MEJAIL, M.; JACOBO, J.; STENBORG, G. Detection and tracking of coronal mass ejections based on supervised segmentation and level sets. **Pattern Recognition Letters**, v .31, n. 5, p. 496-501, 2009.

GOUSSIES, N.; STENBORG, G.; VOURLIDAS, A.; HOWARD, R. Tracking of Coronal White-Light Events by Texture. **Solar Physics**, v. 262, n. 2, p. 481-494, 2010.

HARALICK, R.M., SHANMUGAM, K., DINSTEIN, I. Textural features for image classification. **IEEE Transactions on Systems, Man and Cybernetics**, v. SMC3, p. 610-621, 1973.

HARRISON, R. A. Solar coronal mass ejections and flares. **Astronomy and Astrophysics**, v. 162, p. 283-291, 1986.

HAYES, A. P.; VOURLIDAS, A.; HOWARD, R. A. Deriving the electron density of the solar corona from the inversion of total brightness measurements. **The Astrophysical Journal**, v. 548, p. 1081-1086, 2000.

HOWARD, R. A. ET AL. Observations of CME from SOHO/LASCO. In: CROOKER, N.; JOSELYN J. A.; FEYNMAN, J. (eds). **Coronal mass ejections**. Washington, DC: American Geophysical Union, v. 99, p. 17-26, 1997.

HOWARD, R. A.; MICHELS, D. J.; SHEELEY, N. R. JR.; KOOMEN, M. J. The observation of a coronal transient directed at Earth, **Astrophysical Journal**, v. 263, n. 2L, p. 101-104, 1982.

HOWARD, R. A.; SHEELEY, N. R. Jr.; KOOMEN, M. J.; MICHELS, D. J. Coronal mass ejections 1979-1981. **Journal of Geophysical Research**, v. 90, p. 8173-8191, 1985.

ILLING, R. M.; HUNDHAUSEN, A. J. Disruption of a coronal streamer by an eruptive prominence and coronal mass ejection. **Journal of Geophysical Research**, v.91, n. A10, p. 10951-10960, 1986.

JING, J.; YURCHYSHYN, V. B.; YANG, G.; XU Y.; WANG, H. On the relationship between filaments eruptions, flares and coronal mass ejections. **Astrophysical Journal**, v. 614, p. 1054-1062, 2004.

JOHNSON, T. H. Preliminary report on angular distribution measurements of cosmic radiation in equatorial latitudes. **Physical Reviews**, v. 44, p. 856-858, 1933.

KAHLER, S. W. Solar flares and coronal mass ejections, **Annual Review of Astronomy and Astrophysics**, v. 30, p. 113-141, 1992.

KIVELSON, M. G.; E RUSSELL, C. T. **Introduction to Space Physics**. Los Angeles: Cambrige University Press, 1995. 568p.

KOUTCHMY, S.; LAMY, P.L. Properties and Interactions of Interplanetary Dust. **ASSL**, v. 119, IAU Colloq., n. 85, p. 63 p., 1985.

KUWABARA, T.; MUNAKATA, K.; YASUE, S.; KATO, C.; AKAHANE, S.; KOYAMA, M.; BIEBER, J. W.; EVENSON, P.; PYLE, R.; FUJII, Z.; TOKUMARA, M.; KOJIMA, M.; MARUBASH, K.; DULDIG, M. L.; HUMBLE, J. E.; DA SILVA, M. R.; TRIVEDI, N. B.; GONZALEZ, W. D.; SCHUCH, N. J. Geometry of an interplanetary CME on October 29, 2003 deduced from cosmic rays. **Geophysical Research Letters,** v. 100, p. L19803, 2004.

LIEWER, P. C.; DEJONG, E. M.; HALL, J. R.; LORRE, J. J. Automatic CME detection from coronagraph image. **Instrument Engineering (SPIE) Series**, v. CS 5901, p. 13 – 24, 2005.

LIN, Z.; BIEBER, J.; EVENSON, P. Electron trajectories in a model magnetosphere:simulation and observation under active conditions. **Journal of Geophysical Research**, v. 100, p. 23543-23550, 1995.

MCCRACKEIN, K. G., RAO, U. R; SHEA, M. A. The trajectory of cosmic ray in a high simulation of geomagnetic field. v. 77, **Massachusetts Institute of Technology**, Cambridge, 1962.

MUNAKATA, K., BIEBER, J. W.; YASUE S.; KATO, C.; KOYAMA, M.; AKAHANE, S.; FUJIMOTO, K.; FUJII, Z.; HUMBLE, J. E.; DULDIG, M.L. Precursors of geomagnetic storms observed by the muon detector network, **Journal of Geophysical Research**, v. 105, p. 427-457, 2000.

MURSULA, K.; USOSKIN, I, **Heliospheric Physics and Cosmic Rays**, Lecture Notes, University of Oulu, Oulu, 2003.

NAGASHIMA, K.; FUJIMOTO, K.; SAKAKIBARA, S.; MORISHITA, I.; TATSUOKA, R. Local-time Dependent Pre-IMF-shock Decrease and Post-shock Increase of Cosmic Rays, Produced Respectively by their IMF-collimated Outward and Inward Flows Across the Shock Responsible for Forbush Decrease, **Planetary and Space Science**, v. 40, p. 1109-1137, 1992.

OKAZAKI, Y. **Three dimensional anisotropy and density gradient of galactic cosmic rays measured by global muon detector network**. Ph.D. dissertation, Tohoku University, 2008.

OKAZAKI, Y.; FUSHISHITA, A.; NARUMI, T.; KATO, C.; YASUE, S.; KUWABARA, T.; BIEBER, J.; EVENSON, P.; SILVA, M. D.; LAGO, A. D.; SCHUCH, N.; FUJII, Z.; DULDIG, M.; HUMBLE, J.; SABBAH, I.; KOTA, J.; MUNAKATA, K. Drift effects and the cosmic ray density gradient in a solar rotation period: First observation with the global muon detector network (GMDN). **Astrophysical Journal**, v. 681, p. 693-707, 2008.

OLMEDO, O., ZHANG, J., WECHSLER, H., POLAND, A., BORNE, K. Automatic detection and tracking of coronal mass ejections in coronagraph time series. **Solar Physics**, v. 248, p. 485-499, 2008.

PARKER, E. N. **Interplanetary dynamical processes**, Interscience Publishers, New York, NY, 1963.

PARKS, G. K. **Physics of Space Plasmas** – an introduction. Second Edition. Westview Press Inc, 2004. 616 p. ISBN: 0813341302.

PLUNKETT, S. P.; THOMPSON, B. J.; HOWARD, R. A.; MICHELS, D. J.; ST. CYR, O.C.; TAPPIN, S. J.; SCHWENN R.; LAMY P. L. LASCO observations of an earth-directed coronal mass ejection on may 12, 1997. **Geophysical Research Letters**, v. 25, n. 14, p. 2477-2480, 1998.

QU, M., SHIH, F.Y., JING, J.,WANG, H. Automatic detection and classification of coronal mass ejections. **AGU Fall Meeting Abstracts**, SH14A-01, 2005.

ROBBRECHT, E.; BERGHMANS, D. Automated recognition of coronal mass ejections (CMEs) in near-real-time data. **Astronomy & Astrophysics**. v. 425, p. 1097-1106, 2004.

ROBBRECHT, E.; BERGHMANS, D.; VAN DER LINDER, R. A. M. Automated LASCO CME catalog for solar cycle 23: are CMEs scale invariant? **The Astrophysical Journal**, v. 691, p. 1222-1234, 2009.

RUST, D. M.; KUMAR, A. Evidences for helically kinked magnetic flux rope in solar eruptions. **Astrophysical Journal Letters**, v. 464, p. L199, 1996.

SAGISAKA, S. Atmospheric effects on cosmic-ray muon intensities at deep underground dephts, **Il Nuovo Cimento C**, v. 9, n. 4, p. 809-828, 1986.

SAITO, K.; POLAND, A. I.; MUNRO, R. H. A Study of the Background Corona Near Solar Minimum. **Solar Physics**, v. 55, p. 121-124, 1977.

SCHEIN, M.; JESSE, W. P.; WOLLAN, E. O. The nature of the primary cosmic radiation and the origin of the mesotron. **Physical Reviews**, v. 59, p. 615-618, 1941.

SCHWENN, R.; DAL LAGO, A.; HUTTUNEN, E.; GONZALEZ, W. D. The association of coronal mass ejections with their effects near the Earth, **Annales Geophysicae**, v. 23, p. 1033-1059, 2005.

SHEELEY, N. R. ET AL. Continuous tracking of coronal outflows: two kinds of coronal mass ejections. **Journal of Geophysical Research**, v.104, n. A11, p. 24739-24767, 1999.

ST. CYR, O. C.; HOWARD, R. A.; SHEELEY JR., N. R.;, PLUNKETT, S. P.; MICHELS, D. J.; PASWATERS, S. E.; KOOMENS, M. J.; SIMNETT, G. M.; THOMPSON, B. J. ; GURMAN, J. B.; SCHWENNS, R.; WEBB, D. F.; HILDNER, E.; LAMY, P. L. Properties of coronal mass ejections: SOHO LASCO observations from January 1996 to June 1998. **Journal of Geophysical Research**, v. 105, n, A8, p. 18169-18185, 2000.

WADA, M.; MURAKAMI, K. Cosmic rays in the interplanetary space. In: ODA, M.; NISHIMURA, J.; SAKURAI, K. **Cosmic Ray Astrophysics**. TERRAPUB, p. 299-334, 1988.

YASHIN, I.I.; BARBASHINA, N. S.; BOROG, V. V.; CAPDEVIELLE, J. N.; KOKOULIN, R. P; PETRUKHIN, A. A.; SAAVEDRA, O; TIMASHKOV, D. A.; SHUTENKO, V. V. Muon diagnostics of magnetosphere and atmosphere of the Earth. **20th European Cosmic Ray Symposium**, Lisbon, 2006

YASHIRO, S.; GOPALSWAMY, N.; MICHALEK, G.; ST. CYR, O. C.; PLUNKETT, S. P.; RICH, N. B.; HOWARD, R. A. A catalog of white light coronal mass ejections observed by the SOHO spacecraft. **Journal of Geophysical Research.**, v. 109, n. A0, p. 7105, 2004.